2017

Investigation of the precipitation and hardening response of maraging stainless steels 17-4 and 13-8+Mo during multi-pass welding

Robert Joseph Hamlin
Lehigh University

Recommended Citation

Hamlin, Robert Joseph, "Investigation of the precipitation and hardening response of maraging stainless steels 17-4 and 13-8+Mo during multi-pass welding" (2017). *Theses and Dissertations*. 2946.
https://preserve.lehigh.edu/etd/2946

Investigation of precipitation and hardening response of maraging stainless steels 17-4 and 13-8+Mo during multi-pass welding

by

Robert J. Hamlin

Presented to the Graduate and Research Committee
of Lehigh University
in Candidacy for the Degree of
Doctor of Philosophy

in

Materials Science and Engineering

Lehigh University

August 2017

Approved and recommended for acceptance as a dissertation in partial fulfillment of the requirements for the degree of Doctor of Philosophy

Date

Dissertation Director

Accepted Date

Committee Members:

John N. DuPont

Herman F. Nied

Wojciech Z. Misiolek

Masashi Watanabe

Acknowledgements

Thank you to Dr. John DuPont for allowing me to join the Engineering Metallurgy Group so that I could continue my education in Materials Science and Engineering. I am very grateful for the patience, guidance and knowledge he has shared with me while working on this project.

I would like to gratefully acknowledge financial support for this research through American Metal Casting's Casting Solutions for Readiness program that is sponsored by the Defense Supply Center Philadelphia, Philadelphia, PA and the Defense Logistics Agency Research & Development Office, Ft. Belvoir, VA.

Thank you to my Engineering Metallurgy Group members; Andrew Stockdale, Brett Leister, Daniel Bechetti, Jon Galler, Erin Barrick, Rishi Kant, Sean Orzolek, Jonah Duch, and Ally Fraser. You have all taught me so much and I greatly appreciate all the time you have spent helping me improve myself as a researcher and a student. I could not ask for a better group of co-workers.

I would also like to thank everyone in the Lehigh University Materials Science and Engineering department for their generosity and their contributions to this research project. Thank you Sue Stetler, Janie Carlin, Katrina Kraft, Arlan Benscoter, Mike Rex, Bill Mushock, Laura Moyer, and all my fellow graduate students.

Thank you to also to Dr. Robino at Sandia National Lab for his technical discussions and support during the analysis of this work.

Finally, thank you to my mother, father, brothers and girlfriend, Leah Kulp, for the love and support they have given me through all my endeavors.

Table of Contents

List of Tables

List of Figures

Abstract

Martensitic precipitation strengthened stainless steels 17-4 and 13-8+Mo are candidate alloys for high strength military applications. These applications will require joining by fusion welding processes thus, it is necessary to develop an understanding of microstructural and mechanical property changes that occur during welding. Previous investigations on these materials have demonstrated that significant softening occurs in the heat affected zone (HAZ) during welding, due to dissolution of the strengthen precipitates. It was also observed that post weld heat treatments (PWHT's) were required to restore the properties. However, PWHT's are expensive and cannot be applied when welding on a large scale or making a repair in the field. Thus, the purpose of the current work is to gain a fundamental understanding of the precipitation kinetics in these systems so that optimized welding procedures can be developed that do not require a PWHT.

Multi-pass welding provides an opportunity to restore the strengthening precipitates that dissolve during primary weld passes using the heat from secondary weld passes. Thus, a preliminary investigation was performed to determine whether the times and temperatures associated with welding thermal cycles were sufficient to restore the strength in these systems. A Gleeble thermo-mechanical simulator was used to perform multi-pass welding simulations on samples of each material using a 1000 J/mm and 2000 J/mm heat input. Additionally, base metal and weld metal samples were used as starting conditions to evaluate the difference in precipitation response between each. Hardness measurements were used to estimate the extent of precipitate dissolution and growth. Microstructures

were characterized using light optical microscopy (LOM), scanning electron microscopy (SEM), and energy dispersive spectrometry (EDS). It was determined that precipitate dissolution occurred during primary welding thermal cycles and that significant hardening could be achieved using secondary welding thermal cycles for both heat inputs. Additionally, it was observed that the weld metal and base metal had similar precipitation responses. The preliminary multi-pass welding simulations demonstrated that the times and temperatures associated with welding thermal cycles were sufficient to promote precipitation in each system. Furthermore, these findings indicate that controlled weld metal deposition may be a viable method for optimizing welding procedures and eliminating the need for a PWHT.

Next, an in-depth Gleeble study was performed to develop a fundamental understanding of the reactions that occur in 17-4 and 13-8+Mo during exposure to times and temperatures representative of multi-pass welding. Samples of each material were subjected to a series of short isothermal holds at high temperatures and hardness measurements were recorded to investigate the dissolution behavior of each alloy. Additional secondary isothermal experiments were performed on samples that had been subjected to a high temperature primary thermal cycle and hardness measurements were recorded. Matrix microstructures were characterized by LOM and reverted austenite measurements were recorded using X-ray diffraction techniques. The hardness data from the secondary heating tests was used in combination with Avrami kinetics equations to develop a relationship between the hardness and fraction transformed of the strengthening precipitates. It was determined that the

Avrami relationships provide a useful approximation of the precipitation behavior at times and temperatures representative of welding thermal cycles.

Finally, an autogenous gas tungsten arc (GTA) welding study was performed to demonstrate the utility of multi-pass welding for strength restoration in these alloys. Dual-pass welds were made on samples of each material using a range of heat inputs and secondary weld pass overlap percentages. Hardness mapping was then performed to estimate the extent of precipitate growth and dissolution. It was determined that significant softening occurs after primary weld passes and that secondary weld passes, using a high heat input, restored much of the strength. Furthermore, optimal weld overlap percentages were approximated. It was concluded that controlled weld metal deposition can significantly improve the properties of 17-4 and 13-8+Mo and potentially eliminate the need for costly PWHT's.

CHAPTER 1: Introduction

1.1 Industrial Relevance

Martensitic precipitation hardened (PH) stainless steels 17-4 and 13-8+Mo have been used for a number of applications in the aerospace, nuclear and military industries due to their high strength, corrosion resistance and relatively good ductility[1,2]. Recent developments in the heat treating of these materials has significantly improved their strengths making them viable replacements for titanium alloys used in high strength military applications. One such application is the armor plating on the M88 Hercules that is currently made from Ti-6Al-4V, an image of which can be seen in Figure 1[3]. The specific strength and price of each alloy can be seen in Table 1. The improved strength of the PH alloys has increased the specific strength to the point that it is comparable to that of Ti-6Al-4V. 17-4 and 13-8+Mo will provide comparable mechanical properties with a significant decrease in cost and the added benefit of improved weldability[4,5].

1.2 Compositions, Phase Constitution, and Strengthening Mechanisms

Typical compositions of 17-4 and 13-8+Mo can be seen in Table 2. The Cr content in these alloys is important for corrosion resistance, Ni is an austenite stabilizer and helps prevent the retention of excess δ-ferrite during heat treating, and the Cu and Al contents are important for precipitation strengthening in 17-4 and 13-8+Mo, respectively. Upon solidification, these materials form δ-ferrite, initially transform to austenite on cooling and then to martensite with further cooling. The final as-cast microstructure consists of martensite with approximately 10-20% remnant δ-ferrite and less than a few percent retained austenite. Typical heat treatments for these alloys consists of a homogenization step to reverse microsegregation from casting, followed by a solution treatment and quench to produce supersaturated martensite, and a final aging step. The aging step is typically conducted at temperatures between 450ºC and 620ºC for one to five hours to promote the formation of nanometer scale precipitates that greatly strengthen these alloys[6–8,1]. The cast and heat treated microstructures for 17-4 and 13-8+Mo can be seen in Figure 2.

The low carbon content of the martensitic PH stainless steels results in a relatively ductile martensite, low austenite content and minimal carbide formation[9,10]. Thus, the mechanical properties of these alloys are largely derived from the precipitates that form during aging. These precipitates hinder the movement of dislocations during plastic deformation, thereby increasing the strength of the material. 17-4 and 13-8+Mo are strengthened by Cu rich BCC and β-NiAl precipitates, respectively. These particles have the greatest strengthening effect when they are roughly 2-5nm in size and coherent with the matrix thereby forcing dislocation lines to shear through the particles to continue motion[11–13]. If the particles grow too large and become incoherent it is energetically favorable for the dislocation lines to loop around the particles subsequently decreasing the strength of the material[14]. A high-resolution transmission electron microscope (TEM) image of coherent β-NiAl particles embedded in a martensite matrix, taken from works performed by Ping *et al.*, can be seen in Figure 3[12]. The image demonstrates that even with high resolution TEM, these particles are difficult to distinguish from the matrix due to the small size and high coherency. However, because these particles are the major strengthening mechanism in these alloys, measuring mechanical properties can be a useful method for establishing their presence.

Relationships between precipitate morphology and hardness measurements have been established in works performed by Robino *et al.*[15] and Mirzadeh and Najafizadeh[16] using isothermal aging data and Avrami[17–19] analysis. Similar methods will be applied in the current investigation and will be discussed further in Chapter 3.

The applications involving these alloys will require them to be welded. Thus, it was necessary to develop an understanding of the changes in microstructures and mechanical properties that occur in the heat affected zone (HAZ) of these alloys. The temperatures experienced during welding thermal cycles could result in some combination of martensite tempering, austenite and δ-ferrite reversion, precipitate coarsening and dissolution, or secondary carbide formation. Therefore, Gleeble simulated welding study was performed for each alloy to determine the effect of welding thermal cycles on the microstructures and mechanical properties.

1.3 Single Pass Heat Affected Zone Study

A single pass HAZ study was performed using a Gleeble thermomechanical simulator. Fully age hardened samples of each material were subjected to HAZ thermal cycles representative of a gas tungsten arc (GTA) or gas metal arc (GMA) fusion weld. The tensile properties were measured, microstructural characterization was performed by light optical microscopy (LOM) and scanning electron microscopy (SEM), and modeling of the precipitation was performed using MatCalc. The tensile properties of the simulated Gleeble HAZ samples can be seen in Figure 4A[20]. It was observed that the strength decreased significantly through the HAZ for both materials. The trends in mechanical properties could not be explained solely by the LOM and SEM microstructural characterization, thus, modeling was performed using MatCalc to predict the evolution of the strengthening precipitates throughout the HAZ[13,21,22]. The predicted phase fraction of the strengthening precipitates for 17-4 and 13-8+Mo as a function of HAZ region can be seen in Figure 4B[20]. The decrease in phase fraction through the HAZ indicates precipitate dissolution and correlates well with the decrease in strength observed in both alloys. Models were then adjusted to test optimized welding procedures. Models for welding material in the solution treated condition with a post weld age were created and results indicated the phase fraction should be uniform from the base metal through the HAZ for both materials, as shown in Figure 5A[20]. Samples of each material were tested using these conditions and the tensile properties were measured. The tensile properties for the samples that were welded in the solution treated condition and then given a post weld age can be seen in Figure 5B[20]. It was observed that the strength was relatively uniform through all regions of the HAZ for both materials which correlated well with the precipitate evolution predicted using MatCalc. These findings indicate the mechanical properties in these alloys were primarily governed by the dissolution and growth of the strengthening precipitates and that welding thermal cycles are sufficient to result in precipitate dissolution in both materials.

Full-scale welds were made on samples of each material in both conditions and cross-weld tensile samples were extracted. The tensile test results for the welds can be seen in Table 3[20]. The observed trends in mechanical properties matched well with the mechanical properties from the simulated samples. It was found that only 72-76% of the base metal yield strength was retained in the samples welded in the aged condition, whereas over 93% of the base metal yield strength was retained in the samples that were welded in the solution treated condition and then given a post weld age. These findings indicate that relatively uniform mechanical properties can be achieved by welding in the solution treated condition and applying a post weld age. However, post weld heat treatments (PWHT's) are expensive and impractical when welding on a large scale or making a repair in the field. Welding solution treated material will always require a PWHT to strengthen the base metal, therefore is it necessary to investigate alternative methods for welding aged material to potentially eliminate the need for a PWHT. Multi-pass welding provides an opportunity to restore the strength lost during primary thermal cycles using secondary thermal cycles from subsequent weld passes. Studies were performed by Yu *et al.*[23] to investigate the effect of multiple welding thermal cycles on Cu precipitation in a low carbon martensitic steel. It was determined by atom probe tomography and hardness measurements, that the precipitates dissolved during primary high temperature thermal cycles and formed again after secondary thermal cycles representative of multi-pass welding. Therefore, the effect of multi-pass welding on precipitation in 17-4 and 13-8+Mo was studied to determine if the welding thermal cycles could result in re-precipitation.

In the current thesis, Chapter 1 discusses the industrial relevance of alloys 17-4 and 13-8+Mo, describes why optimized procedures are required for welding them and presents the general purpose and approach of the current investigation. Chapter 2 is concerned with establishing a preliminary description of the precipitation behavior based on hardness measurements recorded during multi-pass welding Gleeble simulations. Furthermore, it provides a comparison of the precipitation response in 17-4 and 13-8+Mo as well as the precipitation response of the aged base metal relative to weld metal for each alloy. Chapter 3 builds on the results from Chapter 2 and is focused on characterizing the matrix microstructures (ie: δ-ferrite and martensite contents) by LOM and developing a model for the precipitate evolution during times and temperatures representative of welding thermal cycles using Avrami relationships[17–19]. Chapter 4 describes a dual-pass gas tungsten arc (GTA) welding investigation. This study was performed to determine the influence of secondary weld passes on the hardness of primary weld passes using a range of heat inputs and secondary weld pass overlaps. Finally, a discussion of future work and implications of all these studies is provided in Chapter 5.

CHAPTER 2: Influence of Multi-Pass Weld Thermal Cycles on the Microstructure and Hardness of Maraging Steels 17-4 and 13-8+Mo

Abstract

Martensitic precipitation strengthened stainless steels 17-4 and 13-8+Mo are potential candidates for high strength military applications. These applications will require joining with fusion welding processes, necessitating an investigation into the evolution of the microstructures and mechanical properties during welding. Previous studies on these alloys have demonstrated that softening associated with precipitate coarsening or dissolution occurs in the HAZ during welding and that a post weld heat treatment (PWHT) is required to restore the strength. However, PWHT's are expensive and impractical when welding on a large scale or making a repair in the field, thus, it is necessary to develop optimized welding procedures that do not require PWHT's. Multi-pass welding provides an opportunity to restore the strengthening precipitates that dissolve during primary welding thermal cycles using heat from subsequent weld passes. In the current investigation, a Gleeble thermo-mechanical simulator was used to subject samples of 17-4 and 13-8+Mo to primary and secondary welding thermal cycles representative of a 1000 J/mm and 2000 J/mm heat input multi-pass weld. Age hardened base metal and as-welded weld metal were used as starting conditions to investigate the precipitation response of each condition. Hardness measurements were recorded after each thermal cycle to estimate the extent of precipitate dissolution or growth. It was determined that secondary welding thermal cycles were sufficient to promote hardening in both the base metal and weld metal for each heat input, indicating precipitate growth was occurring. Alloy 17-4 demonstrated a higher precipitation response when compared to 13-8+Mo that was attributed to an increased level

of supersaturation and larger temperature range in which precipitation could occur. It was also observed that the weld metal and base metal possessed similar precipitation responses for each material. Microchemical measurements in the weld metal, thermodynamic modeling and back diffusion calculations demonstrated minimal segregation of the precipitating elements occurs during solidification and that additional back diffusion relieves the composition profiles further. This explains the similarities in precipitation response between the base metal and weld metal. The implications of these findings are that controlled weld metal deposition may be used to eliminate the need for a PWHT.

2.1 Introduction

Martensitic precipitation strengthened stainless steels 17-4 and 13-8+Mo possess a combination of high strength and relatively good ductility, making them ideal for applications in the military, aerospace and nuclear industry[6,24]. These alloys solidify as δ-ferrite and transform to austenite on cooling and martensite upon further cooling. Thus, the microstructure consists of a martensitic matrix with around 10-20% remnant δ-ferrite and less than a few percent retained austenite. The low percentage of retained austenite is due to the low carbon content in these systems (typically < 0.03 wt%), which also results in a relatively ductile martensite and low carbide content. Therefore, changes in the mechanical properties of these alloys are largely controlled by the evolution of fine nanometer scale precipitates that form during heat treatment[1,2]. Alloys 17-4 and 13-8+Mo are strengthened by BCC Cu precipitates and β-NiAl precipitates, respectively. Following casting these alloys are homogenized to reverse microsegregation, solution treated and quenched to produce a supersaturated martensite, and then aged at temperatures between 450°C and

620ºC for times ranging from 1 to 5 hours to promote the formation of the strengthening precipitates[1,2]. During the early stages of aging the precipitates are on the order of 2-3 nm in size and highly coherent with the matrix, resulting in a drastic increase in strength by forcing dislocation lines to shear through the particles. After prolonged aging particle coarsening occurs, resulting in loss of coherency, and causing dislocation lines to loop around the particles concurrently decreasing the strength. If temperature is increased further dissolution can occur, also decreasing the strength[25,26].

Large scale applications involving these materials require joining with welding processes, which has provoked several studies on the effects of the welding thermal cycles on the properties of these alloys. The high temperatures experienced during welding are sufficient to result in microstructural changes such as martensite to austenite transformation, austenite to δ-ferrite transformation and precipitate growth, coarsening and dissolution[7,20,27]. Previous investigations on 17-4 and 13-8+Mo have demonstrated that the temperatures experienced in the heat affected zone (HAZ) of fusion welds result in a significant decrease in strength that has been associated with precipitate dissolution[20]. Furthermore, it was determined that the evolution of the major microstructural features such as martensite and δ-ferrite had minimal effect on the changes in properties and that the changes were the result of precipitate dissolution or growth[20]. Bhaduri *et. al*[28] observed similar softening in the HAZ of 17-4 using hardness measurements and attributed the softening to the dissolution of precipitates, though coarsening was also thought to be occurring as well. However, in both experiments it was observed that optimal properties could be achieved if a post weld heat treatment (PWHT) is applied. However, PWHT's are expensive and cannot be applied when welding on a large scale or making a repair in the field, necessitating development of optimized welding procedures that do not require a PWHT.

Multi-pass welding provides an opportunity to reheat the region that softens during primary weld passes by the heat from secondary weld passes. Studies were performed by Yu *et al.*[23] to investigate the effect of multiple welding thermal cycles on Cu precipitation in a low carbon martensitic steel, BlastAlloy 160. Atom probe tomography and hardness measurements demonstrated that the precipitates dissolved during primary high temperature thermal cycles and formed again after secondary thermal cycles representative of multi-pass welding[23]. If the times and temperatures associated with welding thermal cycles are sufficient to promote reprecipitation in 17-4 and 13-8+Mo, it may be possible to eliminate the need for a PWHT by controlled weld metal deposition. The purpose of the current investigation is to determine the hardening response of these materials after exposure to primary and secondary thermal cycles representative of multi-pass welding. Two heat inputs were investigated as well as both age hardened material and weld metal starting conditions. If sufficient hardening can be achieved using multi-pass welding it may be possible to eliminate the need for a PWHT, decreasing the cost associated with welding these materials.

In the current investigation, peak aged material and weld metal were subjected to primary and secondary welding thermal cycles representative of multi-pass welding using a Gleeble

3500 thermomechanical simulator. Hardness measurements were then used to estimate the extent of precipitate dissolution and growth. The precipitation response of the weld metal was investigated, in addition to the peak aged material, because the as-solidified microstructure differs significantly from the base metal. This difference in microstructure combined with the residual segregation from solidification may influence the precipitation response of the weld metal as compared to the heat treated base metal. Brooks and Garrison[24] determined by transmission electron microscopy (TEM) and mechanical testing that the weld metal of various precipitation strengthened stainless steels, including 13-8+Mo, aged more intensely at lower temperatures when compared to their respective base metals and were more resistant to over aging (coarsening)[24]. It was also observed in works by Bhaduri *et. al*[28] that the hardening response of 17-4 weld metal was either faster or slower than the base metal depending on the base metal starting condition. Thus, it is important to consider the hardening response of the base metal and weld metal during exposure to multiple thermal cycles.

Another consideration when welding precipitation strengthened alloys is the effect of heat input. Higher heat inputs will increase the temperature at greater distances into the base metal, thereby decreasing the thermal gradient and concurrently the cooling rate. Slower cooling rates will allow for more time at temperatures where growth can occur and may therefore provide additional strengthening during secondary thermal cycles. In the same work on 17-4 performed by Bhaduri *et. al*[28] it was observed that the welding heat input had significant effects on both the hardness and tensile properties of weldments. However, it was also observed that a PWHT was still required to optimize properties[28]. Two heat inputs of 1000 and 2000 J/mm were used in the current investigation to simulate a relatively low and high heat input for the gas tungsten arc (GTA) and gas metal arc (GMA) welding process.

2.3 Experimental Procedure

The chemical compositions of 17-4 and 13-8+Mo used during this investigation can be seen in Table 4. Cast 17-4 and 13-8+Mo plates were hot isostatic pressed (HIPed) at 1162ºC and 103 MPa to eliminate porosity and minimize residual segregation from casting, and then air cooled to room temperature. The 17-4 and 13-8+Mo samples were solution treated at 1052ºC and 926ºC, respectively. Following solution treatment, 17-4 samples were air cooled to room temperature and 13-8+Mo samples were argon gas cooled followed by a water quench to 15ºC. Samples were then aged for 1.5 hours at 579ºC and four hours at 593ºC for 17-4 and 13-8+Mo, respectively. Autogenous gas tungsten arc (GTA) welds were made on a half inch thick plate of each material using a current of 200 A, voltage of 10 V, travel speed of 1 mm/s, and 99.98% argon shielding gas.

The aged plates were machined into 70 mm long, 6 mm diameter pins. Additional cross-weld samples of matching dimensions were machined from the GTA weld plates, with the weld metal centered in each pin. A Gleeble 3500 Thermo-mechanical simulator was used to subject samples to various combinations of welding thermal cycles representative of multi-pass welding for a 1000 J/mm and a 2000 J/mm heat input. It should be noted that during Gleeble experimentation, the cooling rates required for the 1000 J/mm thermal cycle could not be fully achieved and therefore the data may not be entirely representative of a 1000 J/mm heat input. However, the heating rates were achievable and the thermal cycles are still representative of a lower heat input than 2000 J/mm. Welding thermal cycles were calculated for four peak temperatures for each alloy using Sandia's SmartWeld program[29,30]. Peak temperatures of 650ºC, 875ºC, 1150ºC and 1300ºC were used for 17-4 and 650ºC, 850ºC, 1150ºC and 1300ºC were used for 13-8+Mo. These four peak temperatures were chosen to represent the four major HAZ regions for each alloy based on recent work performed by Hamlin and DuPont[20]. Thermal cycle combinations were chosen to simulate multi-pass welding, the combinations used in these experiments can be seen in Table 5. The region of a weld that is subjected to a high peak temperature primary thermal cycle may experience two additional thermal cycles during multi-pass welding depending on weld bead placement[31]. Thus, the 1300ºC peak temperature has a tertiary thermal cycle as well. Hardness testing was performed after primary and secondary thermal cycles using a Leco LM 248AT vicker's microhardness indenter with a 500g load and 13 second dwell time.

Select samples of each material were prepared using standard metallographic procedures with a final polishing step of 0.05µm colloidal silica. Samples were then etched using Vilella's reagent. Microstructures were characterized using a Reichert Jung MeF3 light optical microscope (LOM) and a Hitachi 4300 SE/N scanning electron microscope with an X-ray detector for energy dispersive spectrometry (EDS). ThermoCalc thermodynamic modeling software was used to model the extent of segregation that occurs upon solidification and the solubility limits for precipitating elements in 17-4 and 13-8+Mo[32].

2.4 Results and Discussion

Hardening Behavior and Evaluation of Matrix Microstructures

Hardness data for the 17-4 and 13-8+Mo samples that were tested using a 2000 J/mm heat input can be seen in Figure 6. After primary thermal cycles, the hardness decreases from 373 HV in the base metal to as low as 347 HV in the HAZ for 17-4 and from 384 HV in the base metal to as low as 347 HV in the HAZ for 13-8+Mo. Light optical photomicrographs of the base metal and the samples subjected to primary thermal cycles can be seen in Figure 7 and Figure 8 for 17-4 and 13-8+Mo, respectively. As recently discussed in more detail, the microstructures consist of varying amounts of tempered martensite, as-quenched martensite and δ-ferrite[20]. The austenite start and finish temperatures (Ac_1 and Ac_3) were recently measured via dilatometry to be 800ºC and 925ºC for 17-4 and 730ºC and 900ºC for 13-8+Mo[20]. The 650ºC peak temperature thermal cycle does not reach Ac_1 and therefore the microstructure resembles the base metal for both alloys, with the exception of the martensite tempering that occurs. At 850ºC for 13-8+Mo and 875ºC for 17-4, the Ac_1 temperature has been surpassed and partial transformation to austenite occurs on heating, resulting in the formation of as-quenched martensite on cooling. Thus, the microstructures are composed of both as-quenched and tempered martensite. The 1150ºC and 1300ºC peak temperatures are above Ac_3 and result in a near complete as-quenched martensite structure with remnant δ-ferrite. Additionally, the δ-ferrite start temperature was measured in the same study[20] to be 1075ºC and 1175ºC for 17-4 and 13-8+Mo, respectively. This is evident from the microstructures for the 17-4 samples heated to 1150ºC and 1300ºC peak temperatures in which an increase in δ-ferrite is evident along inter-lath locations. The same feature can be seen in the 13-8+Mo microstructure that was heated to 1300ºC.

The variations in the matrix microstructure observed here do not account for the changes observed in hardness. The 1150ºC and 1300ºC peak temperature HAZ regions consist primarily of as-quenched martensite which is expected to be harder than the tempered martensite observed in the base metal and after a 650ºC peak temperature thermal cycle[2,33]. However, the hardness is higher in the tempered martensite regions when compared to the as-quenched martensite regions. Therefore, the variations in hardness are attributed to either coarsening or dissolution of the strengthening precipitates, rather than the changes to the matrix microstructures. Studies performed by Robino *et al.*[7] on the heat treatment of investment cast 13-8+Mo observed, using TEM, that even after prolonged aging of 13-8+Mo the β-NiAl precipitates remained coherent with the matrix, indicating coarsening was not occurring[7]. Other research performed by Ping *et al.*[12] on β-NiAl and Bono *et al.*[34] on Cu precipitation in similar systems found that segregation of elements such as Mo, Ni and Mn to the precipitate/matrix boundary created a diffusion barrier that prevented precipitate coarsening. These findings, coupled with the decrease in hardness observed in the current investigation, suggest that precipitate dissolution is the primary mechanism active in these systems that causes reduced hardness. This is further supported by the hardness increase to near base metal levels or higher after exposure to secondary thermal cycles (Figure 6). Such a large increase in hardness can only be due to precipitate growth. If the particles had coarsened after the primary thermal cycles, then reheating from secondary thermal cycles would only coarsen the particles further and a decrease in hardness would be expected[25,26]. Therefore, it was concluded that the precipitates dissolve during primary thermal cycles and that significant hardening can be achieved using secondary thermal cycles for a 2000 J/mm heat input. It should be noted that no secondary thermal cycles were used for the primary thermal cycle of 650ºC. This thermal cycle represents a subcritical temperature and is unlikely to experience significant reheating due to secondary weld passes[31].

The hardness data for the 17-4 and 13-8+Mo samples that were subjected to thermal cycles representative of 1000 J/mm heat input can be seen in Figure 9. A similar decrease in hardness was observed after primary thermal cycles and a similar rise in hardness after secondary thermal cycles for each alloy. However, it was noted that a smaller increase in hardness was observed for the subcritical secondary thermal cycles when compared to the results for the 2000 J/mm heat input. This trend was attributed to the decreased time at elevated temperature associated with the lower heat input thermal cycles which allow less time for precipitate growth during reheating.

Discussion of Apparent Precipitation Response

For both heat inputs, it was observed that the hardening response was slower in 13-8+Mo when compared to 17-4. These findings indicate 17-4 has a faster precipitation response than 13-8+Mo. Precipitate growth rates are controlled by two major factors, the diffusion rate of the precipitate solute element in the matrix and the supersaturation of these elements, which is the driving force for precipitate growth[35,36]. Activation energies for diffusion of Cu, Al and Ni in Ferrite are 284 kJ/mol, 235 kJ/mol, and 245 kJ/mol, respectively, which would imply that precipitation may occur more rapidly in 13-8+Mo,which relies on the formation of β-NiAl precipitates[37]. However, the driving force for precipitate growth depends on the amount of supersaturation[35,36]. Thus, ThermoCalc was used to calculate the solubility limit of Cu in 17-4 and Al in 13-8+Mo.

Calculated solubility plots of Cu in 17-4 and Al in 13-8+Mo can be seen in Figure 10. Martensite cannot be predicted using equilibrium calculations as it is a metastable phase. Thus, ferrite was modeled instead. The changes in Ferrite stability and solubility are expected to be like those of martensite due the similarity between the two phases[2]. The plots include temperatures up to 750ºC and 800ºC for 13-8+Mo and 17-4, respectively, since ferrite is not stable about these temperatures. The nominal composition of Cu and Al in their respective alloys are labeled on the plots and show that the range of temperatures over which the Cu concentration in 17-4 exceeds the solubility limit is much larger than that of Al in 13-8+Mo. Therefore, even though the diffusion rate of Al in 13-8+Mo is higher than Cu in 17-4, the temperature range for precipitation and extent of supersaturation are significantly smaller in 13-8+Mo. Thus, there is decreased driving force for precipitate growth in 13-8+Mo when compared to 17-4 and a slower hardening response would be expected. Even though the precipitation response is not as significant in 13-8+Mo, both alloys show an increase in hardness which indicates the times and temperatures associated with welding thermal cycles are sufficient to promote hardening in the softened region of the HAZ. This suggests that controlled multi-pass welding procedures may be used to restore the strength lost in the HAZ during primary weld passes and potentially eliminate the need for a PWHT.

Comparison of Base Metal and Weld Metal Hardening Response

The as-solidified weld metal microstructure for 17-4 and 13-8+Mo can be seen in Figure 12. These alloys both solidify as δ-ferrite, transform to austenite on cooling and eventually to martensite on further cooling[1,24,38]. The weld metal exhibits a martensitic structure with a significant presence of δ-ferrite. It should also be noted that some extent of residual segregation is expected from solidification and that the composition should not be completely homogeneous throughout the structure. The 17-4 and 13-8+Mo weld metal samples were also subjected to the welding thermal cycle combinations listed in Table 5 for a 2000 J/mm and 1000 J/mm heat input, respectively. Hardness measurements were recorded before and after primary thermal cycles and the results can be seen in Figure 11. The as-welded material was significantly lower in hardness relative to the age hardened base metal. This is expected because after solidification these alloys cool as austenite, which has a higher solubility limit for the precipitating elements than martensite, meaning there is no supersaturation or driving force for precipitation. The transformation to martensite occurs below 200ºC where diffusion is slow and precipitation is unlikely to occur[1,15]. After primary and secondary thermal cycles the weld metal demonstrated a similar increase in hardness as its respective base metal for each material. The hardness in 17-4 returned to near base metal levels or greater and the hardness in 13-8+Mo approached that of the base metal. The apparent similarity in precipitation response between the base metal and weld metal is surprising, as the base metal has been homogenized and the weld metal should contain residual segregation. The presence of segregation can result in local depletion of solute creating regions of the weld metal that are no longer supersaturated and where precipitation cannot occur.

Light optical photomicrographs of the dendritic structures accompanied by composition plots for 17-4 and 13-8+Mo can be seen in Figure 13 and Figure 14, respectively. In general, the results indicate the Cr and Al concentrations are higher and the Ni and Cu concentrations are lower in ferrite regions when compared to the martensite. These results are expected since Cr and Al are ferrite stabilizers while Ni and Cu are known to stabilize austenite (and the austenite will subsequently transform to martensite on cooling)[2]. It was also evident that the Cu in 17-4 and Al in 13-8+Mo showed minimal variation within the martensitic regions. This is significant because the martensitic regions are where the strengthening precipitates will form. The relatively uniform compositional profile for the major precipitating elements in each system explains why a similar precipitation response is seen in both the weld metal and base metal. These results are in good agreement with the findings of Brooks and Garrison[24] who measured the extent of segregation in the weld metal of three maraging stainless steel including 13-8+Mo. In their work, it was found that the dendrite core and boundary composition of Al only varied by 0.2 wt% after solidification.

The lack of compositional variation in the weld metal martensite indicates that limited segregation occurs between the solid and liquid during solidification, and/or that back diffusion was active and relieved any concentration gradients that may have formed. To assess this in more detail, Scheil non-equilibrium solidification calculations were performed using ThermoCalc to simulate the amount of segregation that would be expected for each alloy. These calculations assume complete diffusion in the liquid, no diffusion in the solid and equilibrium at the solid/liquid interface and, thus, give an estimation of the maximum amount of segregation that could be expected for a given composition. A plot of calculated composition as a function of fraction solid can be seen in Figure 15 and Figure 16 for 17-4 and 13-8+Mo, respectively. These materials have been observed to solidify completely as δ-Ferrite after which the solid state transformation to austenite and martensite occurs[8,24,38]. Thus, the concentration of elements in ferrite upon solidification will be representative of the eventual martensite composition at room temperature. The Al and Cu concentrations were predicted to vary from 0.9 wt% to 0.25 wt% and 1.7 wt% to 5.2 wt%, respectively. The highest value of Cu solubility per Figure 10 is 0.5 wt% Cu which indicates supersaturation is expected over the range of compositions within the dendritic substructure in 17-4. However, the lowest solubility limit in 13-8+Mo is 0.6 wt% Al, which indicates there will be regions within the dendritic substructure that are not supersaturated and where precipitation cannot occur. As mentioned previously, Scheil solidification calculations estimate the maximum amount of segregation that will occur and assumes no back diffusion. Thus, back diffusion calculations were performed to determine whether the segregation profile predicted for 13-8+Mo and 17-4 would be relieved during cooling.

Back diffusion during solidification can be calculated using the following equations developed by Brody and Flemings[39] and Clyne and Kurz[40]

$$C_s^* = kC_0[1 - (1 - 2\alpha' k)f_s]^{\frac{k-1}{1-2\alpha' k}} \quad [1a]$$

$$f_s = \left(\frac{1}{1-2\alpha' k}\right)\left[1 - \left(\frac{T_m - T}{T_m - T_l}\right)^{\frac{1-2\alpha' k}{k-1}}\right] \quad [1b]$$

$$\alpha' = \alpha\left[1 - \exp\left(-\frac{1}{\alpha}\right)\right] - \frac{1}{2}\exp\left(-\frac{1}{2\alpha}\right) \quad [1c]$$

$$\alpha = \frac{D_s t_f}{L^2} \quad [1d]$$

Where C_s^* is the solute concentration at a given fraction solid after back diffusion, k is the partitioning coefficient, C_0 is the nominal solute concentration, f_s is the fraction solid, T_m is the melting point of the pure solvent, T_l is the liquidus temperature of the alloy, D_s is the diffusivity of the solute in body center cubic (BCC) Fe, t_f is the solidification time and L is half the dendrite arm spacing. The partition coefficient is the ratio of the solute concentration in the solid and liquid at a given temperature. An average k was calculated using compositions from the ThermoCalc Scheil simulation as 0.56 for Cu in 17-4 and 1.15 for Al in 13-8+Mo. The solidification time was then calculated using the solidification temperature range from ThermoCalc in combination with SmartWeld[29,30]. SmartWeld was used to predict a fusion zone thermal cycle for each alloy for a 2000 J/mm heat input. The solidification time was then taken from each thermal cycle by looking at the time spent between the solidification start and finish temperatures predicted in ThermoCalc. Times of 0.44 seconds and 0.31 seconds were determined for 17-4 and 13-8+Mo, respectively. Half of the dendrite arm spacing was measured on average to be approximately 9 μm for both alloys. The diffusion rates will vary significantly as temperature changes during solidification, thus, diffusion rates of Cu and Al in BCC Fe were taken from literature for temperatures just below the liquidus and just above the solidus for each alloy[41]. The redistributed solute concentration was calculated for 0 to 1 fraction solid and can be seen in Figure 17 accompanied by the Scheil and equilibrium concentration profiles for each alloy. The calculations demonstrate that significant back diffusion is expected within the solidification temperature range for both 17-4 and 13-8+Mo. The Al concentration is predicted to increase in the interdendritic regions to as high as 0.66 wt% in 13-8+Mo. Furthermore, the Cu concentration was predicted to decrease to as low as 3.1 wt%. The implications of these predictions are that the composition profile of the Al in the weld metal is predicted to be comparable to the base metal which would explain the similarity in apparent precipitation response. Additionally, the decrease in Cu concentration in 17-4 results in a decrease in supersaturation, but as the lowest region is still above the predicted solubility limit, precipitation can still occur.

2.5 Conclusions

Samples of 17-4 and 13-8+Mo were subjected to primary and secondary thermal cycles representative of multi-pass welding. Thermal cycles for a 1000 J/mm and 2000 J/mm heat input were used on aged hardened material as well as weld metal. Hardness testing was performed to estimate the extent of precipitate growth and dissolution. The following conclusions can be drawn from this work.

1. The temperatures experienced during primary welding thermal cycles result in precipitate dissolution and a concurrent decrease in hardness in 17-4 and 13-8+Mo

2. Secondary thermal cycles resulted in an increase in hardness for each alloy indicating reprecipitation was occurring. The longer times associated with the 2000 J/mm heat input resulted in a greater increase in hardness than the lower heat input by allowing more time for precipitation to occur.
3. The hardening response of the weld metal is similar to the base metal for each alloy, which was attributed to minimal segregation and additional backdiffusion of the precipitating elements in each system.
4. Cu precipitation in 17-4 occurs more rapidly than β-NiAl in 13-8+Mo and was attributed to more supersaturation and a wider temperature range over which supersaturation is present and precipitation can occur.

CHAPTER 3: Simulation of the Precipitation Kinetics of Maraging Stainless Steels 17-4 and 13-8+Mo during Multi-pass Welding

Abstract

Maraging stainless steels 17-4 and 13-8+Mo are candidate alloys for high strength military applications. Current welding procedures for these materials require the use of a post weld heat treatment (PWHT). However, these treatments are expensive and cannot be applied in the field. Thus, it is necessary to develop welding procedures that do not require the use of a PWHT. A concurrent investigation has demonstrated that the times and temperatures associated with welding thermal cycles were sufficient to promote precipitation in these systems. The purpose of the current investigation is to develop a more detailed understanding of the precipitation kinetics of these materials during times and temperatures representative of welding thermal cycles. Peak aged samples of each alloy were subjected to a series of short isothermal holds at high temperatures using a Gleeble thermomechanical simulator. Hardness measurements were then recorded to estimate the dissolution behavior of each alloy. Additional secondary heating experiments were then performed and hardness measurements were recorded to estimate the extent of precipitate growth. The hardness data was then used in combination with the Avrami equation and strengthening considerations to develop a relationship between hardness and the fraction transformed of the strengthening precipitates. Light optical microscopy was performed on all samples to determine the evolution of the matrix microstructures, and x-ray diffraction as performed on select samples to detect the presence of reverted austenite. It was observed that the matrix microstructures undergo martensite tempering, δ-ferrite formation, grain growth, and austenite transformation on heating that subsequently forms as-quenched martensite

on cooling. However, the matrix microstructure had minimal effect on the hardness while the strengthening precipitates were the primary factor affecting the hardness. Average apparent activation energies for precipitation and growth were calculated as 175 kJ/mol and 132 kJ/mol for 17-4 and 13-8+Mo, respectively, and were in good agreement with values from literature. However, comparison of the measured and calculated hardness values with these activation energies showed appreciable scatter. Thus, data optimization was performed after which is was determined that activation energies of 29 kJ/mol and 71 kJ/mol for 17-4 and 13-8+Mo, respectively, were required to best fit the data. These activation energies were significantly lower than previously reported values for these alloys and were attributed, at least in part, to the starting condition of the material. Simple diffusion calculations indicate the primary thermal cycles in the current investigation result in significantly less solute homogenization as compared to solution treated material in previous investigations. The decreased homogenization may lead to increased local supersaturation, thereby lowering the activation energy. It was concluded that the Avrami relationships provide a reasonable approximation of the precipitation and hardening behavior in 17-4 and 13-8+Mo during times and temperatures representative of welding thermal cycles.

3.1 Introduction

Maraging stainless steels 17-4 and 13-8+Mo are candidate alloys for high strength military applications[24,28]. The low carbon content in these alloys results in a relatively ductile martensite, low retained austenite content, and minimal secondary carbide formation. Thus, their high strength is largely derived from the growth of fine nanometer scale precipitates that form during heat treatment. The applications involving these materials will require welding, necessitating an investigation of the microstructural and mechanical property changes that occur during welding processes. Previous studies on 17-4 and 13-8+Mo have demonstrated significant softening occurs in the heat affected zone (HAZ) during welding, due to the dissolution of the strengthening precipitates, and that a post weld heat treatment (PWHT) was required to restore the properties[6,20]. However, PWHT's are expensive and impractical when welding on a large scale or making a repair in the field. Thus, improved welding procedures for these alloys are required. Multi-pass welding provides an opportunity to reform the strengthening precipitates that dissolve during primary welding thermal cycles using secondary thermal cycles from subsequent weld passes. A concurrent study on 17-4 and 13-8+Mo has demonstrated that the times and temperatures associated with secondary welding thermal cycles are sufficient to restore the hardness lost during primary thermal cycles, indicating precipitate growth is occurring. In the current investigation, an estimate of the precipitate kinetics during primary and secondary thermal cycles was developed using isothermal aging data and Avrami kinetics equations.

Evaluation of precipitation hardening can be performed using the impinged volume Avrami equation[15,17–19,42]

$$x = 1 - exp(-kt)^n \qquad [1]$$

For which x is the fraction transformed, t is time and k and n are constants. The impinged volume equation is used to represent the interference of growing particles due to removal of solute from the matrix by neighboring particles. Thus, it is useful for estimating growth in precipitation strengthened systems such as maraging stainless steels[15,43]. Robino *et al.*[15] developed a relationship between hardness and fraction transformed which was used in combination with impinged volume equation to evaluate the precipitation kinetics during various aging treatments of 13-8+Mo.

$$\frac{H_t^{1.5}-H_0^{1.5}}{H_F^{1.5}-H_0^{1.5}} \propto x = 1 - exp(-kt)^n \qquad [2]$$

H_t being the hardness after some time at a given temperature, H_0 being the solution treated hardness and H_F being the peak aged hardness. Similarly, this relationship was applied to 17-4 in works performed by Mirzadeh and Najafizadeh[16]. In both studies, it was determined that the Avrami equations were useful for estimating the hardening behavior of these materials and give insight to the precipitation kinetics. However, it was noted that, strictly speaking, there are limitations of this method for these alloys since other transformations are occurring simultaneously, including austenite reversion, martensite recovery and formation of other phases after long term aging that can affect the hardness. Thus, in the current study, light optical microscopy (LOM) was performed to evaluate the changes in major matrix microstructure, i.e. changes to the martensite and ferrite morphologies. Additionally, reverted austenite typically forms in low quantities and is typically not detectable using LOM and will therefore be investigated using x-ray diffraction (XRD).

The primary purpose of this investigation is to gain a fundamental understanding of the precipitation kinetics that occur in these systems during times and temperatures representative of primary and secondary welding thermal cycles. The results of this study can form the basis for optimizing thermal cycles in multi-pass welds to restore the strength of 17-4 and 13-8+Mo without the need for a PWHT.

3.2 Experimental Procedure

The chemical compositions of 17-4 and 13-8+Mo used in this study can be seen in Table 6. 17-4 rods were cold drawn to an 8 mm diameter, solution treated for one hour and twenty minutes at 1038ºC, water quenched, and then aged at 482ºC for one hour. 13-8+Mo rods were hot rolled to an 8 mm diameter with a cold finish, solution treated for one hour at 927ºC, water quenched, and aged at 510ºC for four hours. Rods were then sectioned into 70 mm lengths for use in Gleeble simulations.

Preliminary experiments were performed to determine the temperature range and time dependency for precipitate dissolution. A Gleeble thermo-mechanical simulator was used to heat age hardened samples of 17-4 and 13-8+Mo at 1000ºC/s to peak temperatures of 600ºC to 1300ºC in 100ºC increments. An additional peak temperature of 500ºC was used for 13-8+Mo samples. At each peak temperature samples were held for either 0, 5, or 10 seconds and then rapidly cooled. A quartz rod piezometric dilatometer was also used to detect the presence of the austenite and martensite transformations on heating and cooling for each alloy. Hardness measurements were then recorded using a Leco LM 248AT vicker's microhardness indenter with a 500g load and 13 second dwell time for each sample. The hardness measurements were used to indicate the extent of dissolution in each sample. Following these experiments an average dissolution peak temperature of 1100ºC with no hold was chosen as the primary heat treatment for use in secondary heating experiments.

Samples that were heated at 1000ºC/s to 1100ºC and rapidly cooled were then reheated at 1000ºC/s to peak temperatures of 400ºC, 500ºC, 550ºC, 600ºC, and 650ºC with an additional 700ºC peak temperature being used specifically for 17-4. The purpose of these secondary heating experiments was to determine the hardening response of each alloy at times and temperatures representative of secondary welding thermal cycles. The 17-4 samples were held at each temperature for either 0, 5, or 60 seconds and then rapidly cooled. The 13-8+Mo samples showed a slower precipitation response and therefore were held for either 0, 5, 60, or 120 seconds. Additional secondary heating experiments were performed using primary peak temperatures of 900ºC and 1200ºC and a secondary peak temperature of 550ºC for 0, 5, 60, and 120 second holds for each alloy. Hardness measurements were then recorded on each sample to estimate the extent of precipitate growth.

Each sample was prepared using standard metallographic procedures with a final polish step of 0.05 μm colloidal silica. Samples were then etched using Vilella’s reagent and imaged using a Reichert Jung MeF3 light optical microscope. Select samples were also prepared for semi-quantitative X-ray diffraction (XRD) using a Panalytical Empyrean X-ray diffractometer.

3.3 Results and Discussion

Precipitate Dissolution Experiments and Evolution of Matrix Microstructure

The mechanical properties in these alloys are known to be controlled primarily by the evolution of the strengthening precipitates, which are too small to observe by light optical and scanning electron microscopy[7,20,27]. Changes to the matrix microstructures also occur at elevated temperatures such as martensite tempering, austenite formation, grain growth and δ-ferrite formation. Although these microstructural changes do not affect the mechanical properties as much as precipitation, they can affect the precipitate evolution. Thus, LOM was performed on all samples during this investigation to understand the evolution of the matrix microstructures and aid in the interpretation of the precipitate kinetics.

Light optical photomicrographs of 17-4 samples heated at 1000ºC/s to temperatures between 600ºC and 1300ºC with no hold time can be seen in Figure 18. The peak aged starting material (base metal) consisted of tempered martensite and small amounts of δ-ferrite in the form of stringers. The matrix microstructures remained relatively unchanged on heating until the 800ºC and 900ºC peak temperatures, at which point austenite formation began on heating and transformed to as-quenched martensite on cooling. This was demonstrated by the microstructures in Figure 18, in which a combination of as-quenched martensite and tempered martensite was observed. Furthermore, the austenite transformation temperatures, Ac_1 and Ac_3, were measured as 790ºC and 930ºC, respectively, using dilatometry at a heating rate of 1000ºC/s. Thus, at peak temperatures of 1000ºC and higher, complete austenite transformation occurs on heating resulting in a complete as-quenched martensite microstructure on cooling. Finally, at 1300ºC the onset of δ-Ferrite formation was observed. It was also noted that as temperature increased above Ac_3 there was an increase in the prior austenite grain size demonstrating that austenite grain growth increased with peak temperature, as would be expected[2]. Photomicrographs of samples exposed to each peak temperature for a five and ten second hold can be seen in Figure 19 and Figure 20, respectively. It was observed that as hold time increased at 800ºC and 900ºC the austenite transformation progresses, giving rise to increased amounts of as-quenched martensite. It was also noted that the Ac_1 and Ac_3 temperatures for a 1ºC/s heating rate were 700ºC and 880ºC, respectively, therefore, it is likely complete austenite transformation occurred in the 900ºC hold samples. As time increased at 1000ºC, 1100ºC, and 1200ºC a significant increase in prior austenite grain size occurred with respect to the no hold samples. Finally, longer hold times at 1300ºC gave rise to an increase in δ-Ferrite content.

Photomicrographs of 13-8+Mo samples that were heated at 1000ºC/s to temperatures between 500ºC and 1300ºC with no hold time, a five second hold and a ten second hold can be seen in Figure 21 through Figure 23. The microstructural trends were very similar to those observed in 17-4. However, the Ac_1 and Ac_3 temperatures were measured to be 773ºC and 926ºC, respectively, for a 1000ºC/s heating rate and 600ºC and 850ºC, respectively, for a 1ºC/s heating rate. Therefore, austenite transformation began in the samples that were held at 700ºC for five and ten seconds and was complete in the samples heated to 900ºC. Furthermore, no δ-ferrite was observed in the any of the samples until the five second hold at 1300ºC. Thus, the observed changes to the matrix microstructures on heating of these alloys included: austenite transformation (and transformation to martensite on cooling), grain growth and δ-ferrite transformation. These findings are consistent with the microstructural observations made during previous simulated HAZ experiments performed on cast 17-4 and 13-8+Mo[20].

Hardness measurements were recorded on each sample and the results can be seen in Figure 24 for both alloys. A rapid drop in hardness was observed when heating above 600ºC in 17-4 and 500ºC in 13-8+Mo. Above 700ºC for 17-4 and 600ºC for 13-8+Mo the softening was relatively independent of time. The observed hardness trends could not be explained by the changes in matrix microstructure, such as the relative phase fraction of as-quenched martensite, tempered martensite and δ-ferrite shown in Figure 18 through Figure 23. For example, a relatively uniform hardness was measured in the samples that were heated to temperatures ranging from 800ºC to 1300ºC in 17-4 and 700ºC to 1300ºC in 13-8+Mo even though very significant microstructural changes occur within these ranges. This demonstrates that the change in hardness must be the result of changes to the precipitate morphology rather than the matrix microstructures. These results are consistent with other studies conducted on these alloys[20,28]. Softening in maraging systems is typically associated with precipitate coarsening or dissolution[25,26]. The precipitates in maraging steels provide the largest strength increase when they are on the order of 2-3 nm in size and coherent with the matrix so that dislocation lines must shear through the particles during deformation. At prolonged aging or high temperature exposure the particles coarsen, lose coherency with the matrix, and dislocation lines must then loop around the particles rather than shear. This change in dislocation-particle interaction is marked by a decrease in strength which progresses as coarsening continues[11,25,26]. TEM investigations performed by Robino *et al.*[7] on 13-8+Mo have demonstrated that even after prolonged aging of 13-8+Mo the β-NiAl precipitates remain coherent with the matrix, indicating that dislocation cutting is still active and coarsening has not occurred. Furthermore, studies performed by Ping *et al.*[12] on β-NiAl and Bono *et al.*[34] on Cu precipitation in similar systems found that segregation of elements such as Mo, Ni and Mn to the precipitate/matrix boundary created diffusion barriers that inhibited precipitate coarsening. Thus, the decrease in hardness observed in Figure 24 was attributed primarily to precipitate dissolution. However, it is recognized that some coarsening may be occurring and either TEM or atom probe tomography (APT) would be necessary to confirm this. The preliminary heating experiments indicate the temperature ranges for dissolution in 17-4 and 13-8+Mo were ~700ºC to 1300ºC and ~600ºC to 1300ºC, respectively. An 1100ºC peak temperature with no hold time was chosen as a primary thermal cycle for secondary heating experiments. This temperature was chosen as it is near the middle of the complete dissolution region and results in a uniform as-quenched martensite structure, while not having undergone excessive grain growth.

Precipitate Growth Experiments

Samples were heated to 1100ºC at 1000ºC/s, rapidly cooled and then subjected to temperatures ranging from 400ºC to 700ºC for various times. The hardness results from these secondary heating experiments for both materials can be seen in Figure 25. The hardness increased in the 17-4 samples heated above 400ºC and reached near base metal levels in samples that were heated between 550ºC and 650ºC. In the 13-8+Mo samples a slower precipitation response was observed and significant hardening was not achieved until 60 and 120 second hold times. It was also noted that the maximum achieved hardness was approximately 50 HV below the peak aged hardness. Furthermore, the temperature range over which hardening occurred in the 13-8+Mo samples was only between 500ºC and 600ºC. Light optical photomicrographs of select reheated 17-4 and 13-8+Mo samples can be seen in Figure 26 and Figure 27, respectively. No significant change in matrix microstructures was observed during the secondary heating tests, other than martensite tempering, as the peak temperatures were below Ac_1 for each alloy at the given heating rate. However, it was noted that some as-quenched martensite did form in the 13-8+Mo sample that was held at 650ºC for 120 seconds, which can be seen in Figure 27. As mentioned previously, the measured Ac_1 temperature for 13-8+Mo using dilatometry and a heating rate of 1ºC/s was 600ºC, indicating austenite transformation can occur at 650ºC if given sufficient time. Thus, the matrix microstructures demonstrated little to no change during the secondary heating experiments, but showed a significant increase in hardness. These results further demonstrate that precipitation is the major factor affecting the hardness in these systems and that dissolution was the primary cause for the hardness drop after primary thermal cycles. If the initial drop in hardness was primarily the result of precipitate coarsening, then upon reheating particles would continue to coarsen and the hardness would not increase.

Additional secondary heating experiments were performed using primary thermal cycle peak temperatures of 900ºC and 1200ºC and a secondary peak temperature of 550ºC. The purpose of these tests was to determine whether the primary peak temperature will have significant effects on the precipitation response in these systems. After primary treatment, the 900ºC samples will have a structure that consists of both tempered and as-quenched martensite. The 1100ºC and 1200ºC samples will consist of as-quenched martensite, with the 1200ºC sample having a significantly larger prior austenite grain size. The hardness results for samples subjected to each of the primary peak temperatures followed by a 550ºC secondary peak temperature can be seen in Figure 28. In general, the results demonstrate there is a similar precipitation response regardless of starting condition, though a slightly higher initial hardening response was generally observed in the 900ºC samples. Each of the primary thermal cycles dissolves the precipitates as indicated by the decrease in hardness seen in Figure 24. However, they may not result in the same extent of solute homogenization away from the precipitate region once dissolution occurs. If the lower temperature primary thermal cycle does not homogenize the solute as much as the 1100ºC and 1200ºC peak temperature thermal cycles, then formation of the precipitates may occur more rapidly upon reheating. The effect of primary thermal cycle peak temperature on precipitation response is discussed in more detail below.

The results from the precipitate growth experiments demonstrate that the temperature ranges for secondary hardening in 17-4 and 13-8+Mo are 500ºC to 700ºC and 500ºC to 600ºC, respectively (for the temperatures investigated here). This data was then used in combination with Avrami analysis to develop a relationship between the observed changes in hardness and the precipitate kinetics within these temperature ranges.

Avrami Analysis

Similar to the approach used for these alloys in previous work, the hardness data in Figure 28 was used in combination with Eq. [2] to create plots of ln $(\ln((H_F^{1.5} - H_0^{1.5})/(H_F^{1.5} - H_0^{1.5})))$ vs ln t, which can be seen in Figure 29 for each alloy[15,16]. The peak aged hardness of 446 HV for 17-4 and 499 HV for 13-8+Mo were used as H_F and the hardness after the primary thermal cycles was used as H_0. These values were 349 HV for 17-4 and 356 HV for 13-8+Mo. Due to the rapidity of the hardening in these systems, sufficient data could only be obtained at 500ºC and 550ºC for 17-4 and 500ºC, 550ºC and 600ºC for 13-8+Mo. The slope of each line in Figure 29 represents the time exponent (n) from Eq. [1]. The average time exponents for 17-4 and 13-8+Mo were 0.37 and 0.34, respectively. These values are slightly lower than the value of 0.47 obtained by Mirzadeh and Najafizadeh[16] in 17-4 and 0.49 by Robino *et al.*[15] in 13-8+Mo, using data obtained during conventional aging heat treatments that consist of times from 1 to 4 hours at temperatures from 510ºC to 621ºC. However, they are still within the range of 0.2 – 0.5 which have been reported using similar methods in a number of other maraging systems[44,45].

In addition to the growth constants, the apparent activation energy for precipitation in these systems can be calculated using the Arrhenius rate equation[15,46]:

$$k = \frac{1}{t} = k_0 \exp\left(-\frac{Q}{RT}\right) \qquad [3]$$

Where 1/t is the rate at a given fraction transformed, k_0 is a constant, Q is the apparent activation energy, R is the ideal gas constant and T is the absolute temperature[15,46]. A plot of 1/t as a function of 1/T was created at 0.25, 0.5 and 0.75 fraction transformed for 17-4 and 13-8+Mo. Due to the high rate of transformation in 17-4, limited data was available for the lower fraction transformed values. The apparent activation energy plots for both materials can be seen in Figure 30. The slope of the lines in each plot represent Q/R, which can be used to calculate the activation energy ranges of 95 kJ/mol to 255 kJ/mol for 17-4 and 113 kJ/mol to 152 kJ/mol for 13-8+Mo. The activation energy increases with increasing fraction transformed. These findings are consistent with results for maraging systems obtained in other studies[45,47,48]. Floreen and Decker[47] calculated ranges of 105 kJ/mol to 210 kJ/mol while Squires and Wilson[45] found ranges of 128 kJ/mol to 197 kJ/mol. Derivation of Eq. [2] assumes site saturation for precipitation, thus, a constant activation energy is expected. Therefore, it is likely competing reactions that affect the hardening are occurring simultaneously and contributing to the changes in the apparent activation energy[15].

In addition to the variation in activation energies reported within specific studies on maraging systems, a wide range of values has been reported in literature for 17-4 and 13-8+Mo using various measuring techniques, as can be seen in Table 7. Limited data was available for 13-8+Mo, however, the activation energies in 17-4 range from 112-262 kJ/mol. The range in observed activation energies could be the result of competing solid state reactions such as austenite formation and martensite recovery, or due to the differences in measuring techniques. For instance, austenite formation results in softening, thermal contraction, and an increase in resistivity relative to the martensitic matrix[15,16,46,49]. Thus, austenite formation will influence the hardness, dilatometry and resistivity measurements, which were used to calculate the apparent activation energies listed in Table

7. As the relative effect of austenite formation and martensite recovery on each measuring technique is not identical, this may explain the differences in reported values.

The activation energies reported in literature as well as the current investigation are relatively low compared to the activation energies for diffusion of Cu, Ni, and Al in Ferrite. These findings have been interpreted in other maraging systems to indicate precipitate nucleation at dislocations and enhanced precipitate growth due to rapid dislocation pipe diffusion. This assumption is considered reasonable because of the highly dislocated martensitic matrix in these systems[15,16,44–46]. Average activation energies of 175 kJ/mol and 132 kJ/mol for 17-4 and 13-8+Mo, respectively, were used in combination with average n values for the initial calculations of fraction transformed.

To apply Eq. [1] over the range of temperatures that demonstrated precipitate growth, it was first necessary to calculate a k at each of the target temperatures. To do this, Eq. [3] was employed using k_0 values that were measured from the intercepts of the apparent activation energy plots in Figure 30. Average k_0 values of $3.33e^{14}$ 1/s and $3.67e^{6}$ 1/s were determined for 17-4 and 13-8+Mo, respectively. The average k_0 values and activation energies were used in combination with Eq. [3] to calculate k at each temperature. The calculated k was then input to Eq. [1] to determine the fraction transformed for each time and temperature. This method was applied to each of the time and temperature combinations in Figure 28, after which hardness values were back calculated using Eq. [2]. A plot of measured hardness values vs calculated hardness values can be seen in Figure 31.

Appreciable scatter was observed in the plots, indicating the relationships for each alloy do not provide a highly accurate description of the experimental data. As discussed previously, calculation of the activation energy and n values may be suspect due to competing transformations that affect the apparent rate of precipitation. Therefore, the activation energy and n values used for this initial calculation may not be completely accurate. Thus, to develop a relationship that more accurately describes data in the current investigation, data optimization was performed by allowing the activation energy and n values to vary using an iterative approach.

The sum of residuals was calculated between the measured and calculated hardness values. The Q, n and k_0 values were then simultaneously and iteratively varied. What-If analysis was performed on the sum of the residuals after each iteration to minimize the value, thus, providing the best fit. A comparison of the measured and calculated hardness using the optimized Q, n and k_0 values can be seen in Figure 32. The best fit was achieved with n values of 0.31 for 17-4, 0.28 for 13-8+Mo, and significantly lower activation energies and k_0 values for both alloys. The activation energies determined were 71 kJ/mol and 29 kJ/mol for 17-4 and 13-8+Mo, respectively. The n values were within the range reported for precipitation in maraging systems. However, the activation energies were significantly lower and raise the question of whether these results are purely a mathematical best fit or if they are representative of the precipitate kinetics in these systems[15,16,46,49,50]. Previous experiments that have reported values of activation energies were performed on solution treated material at heat treatment temperatures and using significantly longer hold times.

The difference in starting material condition, as well as testing conditions may explain the discrepancy in calculated activation energies and is discussed in more detail below.

Effect of Material Start Condition on Analysis

The primary thermal cycles used in the current investigation result in precipitate dissolution as indicated by the significant decrease in hardness. However, significantly less time is available for diffusion when compared to the typical solution treatment times. The solution treatment times and temperatures used in the current investigation were 80 minutes at 1038ºC for 17-4 and 60 minutes at 927ºC for 13-8+Mo. A simple estimation of the diffusion distance of Cu and Ni during the primary thermal cycles and solution treatments was performed using the following diffusion relationship[51]:

$$x = \sqrt{Dt} \qquad [4]$$

Where x, D and t are the diffusion distance, diffusion rate, and time, respectively. The diffusion rate of Cu and Ni in FCC Fe were calculated using diffusion data taken from literature at temperatures at temperatures of 900ºC, 1100ºC and 1200ºC[41]. Ni was used to represent β-NiAl precipitation as data for Al in FCC Fe could not be found. Plots showing the calculated diffusion distance can be seen in Figure 33 for the primary thermal cycle peak temperatures. The predicted diffusion distances for times ranging from 1 to 5 seconds at 900ºC were between 3 nm and 7 nm for both Cu and Ni. However, the calculated distances at 1100ºC and 1200ºC ranges from 21 nm to 72 nm and 47 nm to 178 nm, respectively. Thus, the calculated diffusion distances are an order of magnitude less at 900ºC when compared to 1100ºC and 1200ºC. These findings indicate that the initial increased hardening response demonstrated by the samples subjected to a 900ºC primary thermal cycle peak temperature, shown in Figure 24, may be the result of the slower diffusion rates and less homogenization of the solute.

The calculated diffusion distance of Cu in Fe after the 17-4 solution treatment was 1.2 μm and the calculated distance of Ni in Fe was 225 nm after the 13-8+Mo solution treatment. Thus, the precipitating elements in these systems may diffuse two or three orders of magnitude further during solution treatment as compared to the rapid primary thermal cycles used in the current investigation. TEM and APT investigations on these alloys have demonstrated the precipitates are approximately 2-5 nm in size with interparticle spacing on the order of tens of nanometers [7,11–13,27]. These distances are comparable to the calculated diffusion lengths for the primary thermal cycles used in this investigation and orders of magnitude smaller than the distance calculated for the solution treatments. Thus, after the primary thermal cycles less solute homogenization is expected, which may result in localized enrichment of the precipitating elements, thereby, increasing the local supersaturation. As supersaturation is the driving force for precipitation this may explain why the optimized activation energy in this study is lower than previously reported values[35,36].

Effect of Competing Reactions on Analysis

In addition to the difference in starting condition, several studies have shown that austenite reversion occurs during aging heat treatments that can cause error in activation energy measurements[7,13,15,27,52,53]. Previous investigations have demonstrated that austenite formation in both 17-4 and 13-8+Mo is related to the diffusion of Cu or Ni to lath and prior austenite grain boundaries. These elements are both austenite stabilizers and decrease the austenite transformation temperature, thus allowing austenite to form at lower temperatures and subsequently suppressing the martensite transformation to below room temperature[7,13,27,52]. Austenite formation results in a decrease in strength and would thus lower the apparent fraction transformed that is estimated by hardness measurements. As shown in Figure 30, a decrease in the fraction transformed results in a decrease in the apparent activation energy. This suggests that austenite reversion in these systems would lower the apparent activation energy. To investigate the presence of reverted austenite, semi-quantitative XRD was performed on select samples of each material from the secondary heating experiments.

Austenite measurements for select 17-4 and 13-8+Mo samples can be seen in Table 8. No austenite was observed in the peak aged 13-8+Mo and 17-4 sample or the 17-4 sample subjected to a primary 1100ºC peak temperature with no hold time. However, 3% austenite was observed in the 13-8+Mo sample after a primary 1100ºC peak temperature with no hold time. Additionally, 3% and 4% austenite was detected in the 13-8+Mo samples subjected to a secondary peak temperature of 650ºC for 60 seconds and 120 seconds, respectively. Therefore, a small amount of austenite formed during the primary thermal cycle and little to no additional austenite was detected after secondary heat treatment. These results suggest that austenite formation does not occur during the secondary heat treatments used in the current investigation for 13-8+Mo. For the 17-4 samples, up to 5%

austenite formed during secondary thermal cycles. However, the sample heated to 650ºC with no hold and the sample heated to 650ºC that was held for 60 seconds, demonstrated approximately the same amount of reverted austenite. The hardness in these two samples was 420 HV for no hold and 361 HV for the 60 second hold. These results suggest the austenite formation was not directly responsible for the decrease in hardness observed in these samples. The low reverted austenite content observed in this investigation can be understood by looking at reported activation energies for austenite reversion in maraging systems, which have been measured around 250 kJ/mol[13,53,54]. In general, this value is higher than the values for precipitation reported in literature in most maraging systems. The higher activation energies indicate austenite transformation takes place at a slower rate compared to precipitation. Thus, the heating rates and hold times used in the current study may be sufficient for precipitate growth, but limit the amount of time available for austenite transformation to occur. The lack of austenite formation observed during secondary thermal cycles in 13-8+Mo and the fact that it appears to have minimal effect on the hardness in 17-4, indicate it was not the primary reason for the low apparent activation energy required for the optimized fit in this investigation though it may have contributed.

Recovery of the martensitic matrix can also cause error in the activation energy measurements. In studies performed by Hochanadel *et al.*[7] a significant reduction in dislocation density occurred after aging heat treatments in 13-8+Mo. In their study, aging temperatures of 510ºC, 538ºC, 566ºC, 593ºC, 621ºC and 760ºC were used with aging times ranging from 1 to 4 hours. However, an observable decrease in dislocation density did not occur until one or more hours at temperatures greater than 566ºC. This suggests the times and temperatures used in the current study may not have resulted in significant reduction to the dislocation density. Additionally, in studies performed by Miner *et al*.[55] and Speich *et al*.[56] it has been concluded that precipitation processes can halt dislocation glide and limit martensite recovery when they occur on dislocations. As the precipitates in 17-4 and 13-8+Mo systems form rapidly and are believed to form on dislocations it is possible the recovery process is inhibited by precipitation. Therefore, the effect of recovery is thought to be minimal in the current investigation.

It was determined in this investigation that the Avrami relationships provide a practical estimation of the precipitation and hardening behavior in both 17-4 and 13-8+Mo during times and temperatures representative of secondary welding thermal cycles. Activation energies and time constants comparable to those observed in the literature were obtained. However, the activation energies after optimization were significantly lower than values reported in previous studies on maraging systems. The low values may just be the result of a mathematical best fit. However, analysis of the testing conditions and competing transformations during this investigation suggest the lower values may have fundamental significance. Austenite formation and martensite recovery may have contributed to the lower activation energies. However, minimal reverted austenite was detected via XRD and significant martensite recovery is unlikely, based on testing conditions and precipitate locations. Thus, the low activation energies were attributed, at least in part, to the calculated diffusion distances of the precipitating solute. The calculations suggest rapid high temperature thermal cycles are sufficient to dissolve the strengthening precipitates, but do not homogenize the solute as much as solution heat treatments. Therefore, there is an increase in local supersaturation and the activation energy required for precipitation upon reheating is lowered.

3.4 Conclusions

Samples of 17-4 and 13-8+Mo were subjected to a series of short isothermal holds at various temperatures representative of welding thermal cycles, hardness measurements were recorded and the matrix microstructures were characterized using LOM and XRD. The hardness data was then used in combination with Avrami equations to develop a relationship between the hardening behavior and precipitation kinetics. The following conclusions can be drawn from this work.

1. During exposure to temperatures representative of welding thermal cycles in 17-4 and 13-8+Mo it was found that matrix microstructures undergo the following changes: martensite tempering, δ-ferrite formation, grain growth and austenite transformation on heating that subsequently forms as-quenched martensite on cooling
2. Precipitate dissolution was the primary softening mechanism in these alloys, during high temperature exposure, and occurs relatively independent of time at temperatures above 700ºC for 17-4 and 600ºC for 13-8+Mo.
3. Precipitate growth was observed at temperatures between 500 and 700ºC for 17-4 and 500 and 600ºC for 13-8+Mo.
4. Average n values were calculated as 0.34 for 13-8+Mo and 0.37 for 17-4. It was also determined that the average activation energies were 175 kJ/mol and 132 kJ/mol for 17-4 and 13-8+Mo, respectively

5. Data optimization yielded lower n values of 0.31 for 17-4 and 0.28 for 13-8+Mo and very low activation energies of 29 kJ/mol and 71 kJ/mol for 17-4 and 13-8+Mo, respectively
6. The low activation energies were attributed, at least in part, to the decreased time available for homogenization of the solute during the primary thermal cycles in these experiments, relative to typical solution heat treatments. It was also noted that austenite reversion and martensite recovery may have contributed.
7. Avrami relationships provide a practical representation of the precipitation and hardening response during exposure to times and temperatures representative of welding thermal cycles in these materials.

CHAPTER 4: Controlled Weld Metal Deposition for Strength Restoration of Maraging Steels 17-4 and 13-8+Mo

Abstract

Martensitic precipitation strengthened stainless steels 17-4 and 13-8+Mo are candidate alloys for use as armor plating in military combat vehicles and will require joining using fusion welding processes. It has been observed in previous works that welding of these materials results in a softened region in the heat affected zone (HAZ), due to the dissolution of strengthening precipitates. Thus, current optimized welding procedures for these alloys require the use of post weld heat treatments (PWHT's), which are expensive and impractical when welding on a large scale or making a repair in the field. Therefore, it is necessary to develop welding procedures for these materials that do not require the use of a PWHT. A concurrent study has demonstrated that the times and temperatures associated with secondary welding thermal cycles, representative of multi-pass welding, are sufficient to promote precipitation and restore the hardness that is lost due to primary weld passes. Thus, in the current investigation dual pass autogenous gas tungsten arc (GTA) welds were fabricated on samples of each material using 1000 J/mm, 2000 J/mm and 3000 J/mm heat inputs and various secondary weld pass overlaps. Hardness mapping was performed across the fusion zone (FZ), HAZ and base metal of each weld pair to estimate the extent of precipitate growth and dissolution. The purpose of the current investigation was to demonstrate the utility of multi-pass welding for strength restoration in these systems. It was found that secondary weld passes using a 2000 J/mm and 3000 J/mm heat input were sufficient to increase the hardness in the softened primary weld passes to near base metal levels in 17-4. Additionally, secondary weld passes with a 3000 J/mm heat restored 50%

of the hardness lost during primary weld passes in 13-8+Mo. It was also determined that secondary weld overlap percentages of 60-70% for 17-4 and greater than 75% for 13-8+Mo were required to minimize the softened region from primary weld passes. The implications of these findings are that controlled weld metal deposition could be used to significantly improve the properties of multi-pass welds on these alloys and may eliminate the need for a PWHT.

4.*1 Introduction*

Martensitic precipitation strengthened stainless steels 17-4 and 13-8+Mo are candidate alloys for use as armor plating in military combat vehicles due to their high strength, moderate ductility and relatively low cost[1,2]. These applications will require joining using fusion welding processes, which has spurred several investigations into the microstructure and mechanical property changes that occur during welding of these alloys. The matrix microstructure of these materials consists of a martensitic matrix with anywhere from 10-20% remnant δ-ferrite. They also have a low carbon content resulting in minimal austenite and carbide formation, thus, the mechanical properties are largely controlled by the formation of fine nanometer scale precipitates that form during aging heat treatment. 17-4 and 13-8+Mo are strengthened by BCC Cu rich precipitates and β-NiAl precipitates, respectively[1,2]. Previous studies concerned with the welding of these alloys have demonstrated that significant softening occurs in the heat affected zone (HAZ) during welding due to the dissolution of these strengthening precipitates, and that the use of a post weld heat treatment (PWHT) was required to restore the properties[1,20,28]. However, PWHT's are expensive and cannot be applied when welding on a large scale or making a repair in the field, thus necessitating an investigation into optimized welding procedures that do not require a PWHT. Multi-pass welding provides an opportunity to restore the strengthening precipitates that dissolve during primary weld passes using the heat from secondary weld passes[23].

A concurrent study performed on 17-4 and 13-8+Mo has demonstrated that the times and temperatures associated with secondary welding thermal cycles were sufficient to increase the hardness in the softened HAZ and weld metal of these materials, indicating precipitation was occurring. Additional isothermal Gleeble simulations were performed on samples of each material to estimate the precipitate kinetics at times and temperatures representative of welding thermal cycles. It was determined that precipitate dissolution occurs rapidly at temperatures above 700ºC in 17-4 and above 600ºC in 13-8+Mo. It was also observed that significant hardening could be achieved using relatively short hold times between 500ºC and 700ºC for 17-4 and 500ºC and 600ºC for 13-8+Mo. During welding, the amount of base plate that will be exposed to each of these temperature ranges will depend on the welding heat input. Heat input is an important welding parameter given by:

$$\frac{Q_{nominal}}{V} = \frac{EI}{V} \qquad [1]$$

Where Q is the power, E is the voltage, I is the current and V the heat source travel speed. A constant voltage and travel speed were used in the current investigation and current was varied to change the heat input. Higher heat inputs will increase the temperature at greater distances into the weld plate, thereby increasing the size of both the fusion zone (FZ) and HAZ. Additionally, by increasing the temperature further into the base plate the higher heat inputs result in a decrease in the thermal gradient and subsequently decrease the cooling rate. Therefore, with a higher heat input, it is expected that more time will be available at elevated temperature where precipitation can occur[31,33].

In the current investigation, dual pass welds were made using gas tungsten arc (GTA) welding on samples of each material with a range of heat inputs and weld overlaps. Hardness mapping was then performed to estimate the extent of precipitation that could be achieved using secondary weld passes. These results were then compared to the results from the simulated Gleeble studies to estimate the precipitate kinetics. The purpose of this work is to determine the utility of multi-pass welding as a means for restoring the strength in 17-4 and 13-8+Mo weldments and potentially eliminate the need for a PWHT.

4.2 Experimental Procedure

The chemical compositions of 17-4 and 13-8+Mo used in the current investigation can be seen in Table 9. 17-4 bar was hot rolled to a one inch thickness, straightened and pickled. It was then solution treated for six hours at 1038ºC, water quenched, and aged at 482ºC for one hour followed by an air cool. 13-8+Mo bar was rolled to a one inch thickness diameter with a hot finish, solution treated for one and a half hours at 927ºC, fan cooled, and then aged at 510ºC for four hours followed by an air cool. The one inch bar of each material was sectioned into three inch by three inch square sections for use in welding experiments.

Preliminary modeling was performed using Sandia's SmartWeld program[29,30]. Weld isotherms were calculated for a 1000 J/mm, 2000 J/mm and 3000 J/mm heat input for 17-4 and 13-8+Mo. It should be noted that 13-8+Mo was not available in the SmartWeld database, thus, 15-5PH was used for simulations to represent 13-8+Mo as it matched closest in composition and thermal conductivity for the materials available.

Dual pass autogenous GTA welds were made on sections of 17-4 using a 1 mm/s travel speed, voltage of 10V, and three currents of 100A, 200A, and 300A to represent heat inputs of 1000 J/mm, 2000 J/mm, and 3000 J/mm, respectively. Welds were fabricated using three secondary weld pass target overlaps of 25%, 50% and 75% for each heat input. Additionally, welds pairs for each overlap percentage were fabricated using a 3000 J/mm heat input on plates of 13-8+Mo. ImageJ image analysis software was then used to measure the actual percentage of overlap for each weld.

Welds were cross-sectioned and hardness mapping was performed using a Leco LM 248AT vicker's microhardness indenter with a 100g load and 13 second dwell time. Select samples were prepared using standard metallographic procedures with a final polish step of 0.05 μm colloidal silica. Samples were then etched using Vilella's reagent and imaged using a Reichert Jung MeF3 light optical microscope (LOM).

4.3 Results and Discussion

Weld Isotherm Simulations

Sandia's SmartWeld program is based on the Rosenthal heat flow equations and can be used to model temperature profiles as a function of distance from the heat source for various welding conditions[29,30,57]. The temperature ranges over which precipitate growth and dissolution occur in 17-4 and 13-8+Mo can be used in combination with Smartweld isotherms to estimate the approximate size of these regions, in terms of distance. Simulated weld isotherms for a 1000 J/mm, 2000 J/mm, and 3000 J/mm heat input for 17-4 and 13-8+Mo can be seen in Figure 34 and Figure 35, respectively. The figures demonstrate that as heat input is increased, the size of both the fusion zone (FZ) and heat affected zone (HAZ) increases. As mentioned previously, significant precipitate dissolution occurs at temperatures above 700ºC for 17-4 and above 600ºC for 13-8+Mo. While growth of precipitates was observed at temperature ranges of 500ºC to 700ºC for 17-4 and 500ºC to 600ºC for 13-8+Mo. Looking at these temperature ranges for the 17-4 isotherms it was observed that the dissolution region and growth region are similar in size for any given heat input. For example, the distance between the fusion line and 700ºC for the 3000 J/mm heat input was approximately 2.5 mm while the distance between 700ºC and 500ºC was approximately 2 mm. Therefore, if the growth region can be directly overlapped on top of the dissolution region during welding, much of the softened region could be eliminated. Looking at the isotherms for 13-8+Mo it was observed that the dissolution region was on the order of 4 mm while the growth region was approximately 1.5 mm indicating less of the weld will be composed of regions where precipitate growth can occur. These results were then used in combination with hardness data measured across dual-pass GTA welds to relate the temperature profiles to relative amounts of precipitate dissolution and growth.

Evaluation of Hardening Response

Hardness maps measured across dual pass 17-4 GTA welds at three overlap percentages for a 1000 J/mm heat input can be seen in Figure 36. It was observed that no hardening occurred due to secondary weld passes and that the FZ and softened region of the HAZ possessed a relatively uniform hardness of 350 HV. In the FZ the weld metal solidifies as δ-ferrite and then transforms to austenite on cooling and eventually martensite once cooled below ~150ºC. Austenite has a higher solubility for Cu than martensite, thus, there is no supersaturation on cooling and no driving force for precipitation until cooled below 150ºC, at which point there is minimal thermal energy available for precipitation to occur[1,24]. Therefore, the FZ hardness of 350 HV should be representative of precipitate free material. A hardness of 350 HV was also observed in the HAZ of both the primary and secondary passes.

The hardness maps for each overlap percentages of dual pass 17-4 welds fabricated with a 2000 J/mm and 3000 J/mm heat input can be seen in Figure 37 and Figure 38, respectively. It was observed that significant hardening was achieved in both the FZ and HAZ of the primary passes after exposure to heat from the secondary weld passes. These observations indicate the time at elevated temperatures associated with higher heat inputs is sufficient to promote precipitation in this system. The observed similarity in hardening response in the FZ and base metal was surprising. The FZ should contain segregation that can lead to local depletion of Cu in the weld metal resulting in regions of the material where supersaturation does not exist and precipitation cannot occur[33]. However, the similarity in precipitation response between base metal and weld metal in these alloys was investigated in a concurrent paper. The similarity was attributed to minimal segregation in the FZ and additional backdiffusion which resulted in a relatively homogeneous distribution of Cu in the weld metal. A band of increased hardness on the order of 3 mm was observed in each of the welds except for the 78% overlap with a 2000 J/mm heat input. This exception was attributed to the secondary pass overlapping too far into the base metal and thus providing additional softening to the primary weld pass. In the remainder of the samples, a hardness increase from 350 HV to as high as 475 HV was observed in both the weld metal and base metal after secondary passes. It was also observed that and overlap percentage around 60-70% could eliminate most of the softened region from the primary weld pass.

Hardness maps measured across 13-8+Mo dual-pass welds for a 3000 J/mm heat input can be seen in Figure 40. A band of increased hardness, as in 17-4, can be seen in the primary pass after exposure to the heat from the secondary pass. The hardness ranges of the softened region, secondary hardness band and base metal were approximately 350-400 HV, 450-500 HV and 500-550 HV, respectively. These findings are consistent with the findings from the simulated multi-pass welding study performed on these alloys which demonstrated that only a maximum of 50% of the hardness that was lost during primary thermal cycles could be restored using secondary thermal cycles. Additionally, the apparent width of the growth regions and dissolution regions were 2-3 mm, and 5-6 mm, respectively. The lower percentage of secondary hardening and the decreased size of the growth region relative to the dissolution region, indicate that strength restoration using multi-pass welding will be more difficult in comparison to 17-4. Additionally, it was determined that an overlap greater than 75% would be required to eliminate the softened region from the primary weld pass. However, it should be noted that controlled weld metal deposition can still significantly improve the strength in this system and should be considered if welding in the aged condition.

Correlation between Simulated Isotherms and Experimental Results

The 2000 J/mm heat input maps demonstrate that the width of the growth and dissolution region for each weld was approximately 3 mm and 3.5mm, respectively. While for the 3000 J/mm samples the dissolution and growth regions were approximately 4 mm and 4.5 mm, respectively. The predicted isotherm widths per SmartWeld were significantly smaller than the apparent widths seen in the hardness maps. This discrepancy could be the result of differences in the predicted weld pool shape as compared to the actual weld pool. SmartWeld models the FZ and isotherms as semi-circular while the shape of the weld pool demonstrated by the 17-4 welds was more oblong, as can be seen in the light optical image in Figure 39. The oblong nature of the weld pool may be the result of surface tension or arc shear stresses that act on the liquid during welding and push the weld metal outward, thus, creating a wider weld pool[33]. SmartWeld calculations do not account for fluid flow in the weld pool which may explain the differences between predicted and measured isotherm sizes. However, even though the exact size of the isotherms cannot be predicted, the ratio between growth and dissolution region are similar. The ratio of the growth region size to the dissolution region size in the 2000 J/mm and 3000 J/mm heat inputs were 0.85 and 0.89, respectively, while the ratios from the predicted isotherms were approximately 0.76. Making this comparison for the 13-8+Mo weld it was observed that the measured and calculated ratios were 0.41 and 0.33, respectively. The difference between the measured and calculated ratios was approximately 12-20% for each material. Thus, even though the isotherm widths were not accurately modeled using SmartWeld, the relative size and location of the regions for a given heat input may be estimated. Therefore, SmartWeld could still be employed as a useful predictive tool for weld bead overlap.

The dual-pass welding results demonstrate that secondary weld passes may be used to restore much of the strength that is lost in the FZ and HAZ during primary weld passes. This information may be used to plan weld bead placement during multi-pass welding to minimize the amount of softened material in the FZ and HAZ. It should be noted that complete elimination of the softened regions during welding is unlikely, however, controlled weld metal deposition may be able to significantly improve the properties in applications when PWHT's cannot be applied. This work is a first step towards development of multi-pass welding procedures.

4.4 Conclusions

Dual-pass GTA welds were fabricated on maraging stainless steel 17-4 using a 1000 J/mm, 2000 J/mm and 3000 J/mm heat input with various overlap percentages. Additionally, dual-pass welds were made on maraging stainless steel 13-8+Mo using a 3000 J/mm heat input.

Hardness mapping was then performed on all samples to estimate the extent of precipitate growth and dissolution. The following conclusions can be drawn from this work.

1. Secondary welding thermal cycles for a 1000 J/mm heat input do not increase the temperature for long enough times to allow for precipitation in 17-4
2. Increased hardness to near base metal levels can be achieved using secondary welding thermal cycles for a 2000 J/mm and 3000 J/mm heat input for 17-4
3. Secondary weld thermal cycles for a 3000 J/mm heat input increase the hardness in the softened primary regions, though not to the same extent as in 17-4
4. SmartWeld does not accurately predict the isotherms distances for the welding conditions used in this investigation but, can predict the isotherm size ratios within 12-20%
5. Controlled weld metal deposition may significantly improve the properties of both 17-4 and 13-8+Mo weldments and should be considered in further detail

CHAPTER 5: Future Work and Implications

5.1 Future Work

The purpose of this investigation was to optimize welding procedures for maraging stainless steels 17-4 and 13-8+Mo. Current welding procedures for these materials require the use of a post weld heat treatment (PWHT), which is impractical for the applications in which these alloys will be used. Thus, controlled weld metal deposition through multi-pass welding was investigated to eliminate the need for a PWHT. Multi-pass welding provides an opportunity to regrow precipitates that dissolve during primary weld passes using the heat from secondary weld passes. Preliminary multi-pass welding Gleeble simulations indicated that the times and temperatures associated with secondary welding thermal cycles were sufficient to promote precipitation. Thus, an in-depth Gleeble study was performed to determine the extent of precipitate growth and dissolution that would be expected at various temperatures representative of welding thermal cycles. The data from these experiments was used in combination with Avrami kinetics equations to develop a relationship for calculating the amount of precipitate growth that can occur during welding thermal cycles in each system. Additionally, dual-pass autogenous GTA welds were fabricated on samples of each material and hardness mapping was performed to relate the simulated results to actual welding processes. This work is a first step towards developing welding procedures that do not require the use of a PWHT for these systems. During this investigation, it has become evident that additional experiments could be performed to improve upon the work presented in this study

A simple calculation of the diffusion distance for the precipitating solutes in each alloy was performed during this work. These calculations provided an order of magnitude estimate based on the diffusion rates of the solute in pure Fe. The purpose of these calculations was to compare the amount of solute homogenization that would occur during primary thermal cycles, representative of welding, to the homogenization that would occur during a solution heat treatment. Thermodynamic and kinetics software packages Thermocalc and Dictra could be employed in the future to better estimate the solute homogenization rates at the various temperatures investigated in this study. Additionally, the isothermal Gleeble experiments performed in these works could be used on solution treated material to aid in interpreting the effect of solute homogenization on the precipitation response.

It was concluded that the Avrami kinetics equations provide a reasonable approximation of the precipitation and hardening response in the growth region of a welding thermal cycle. Furthermore, complete dissolution occurs at temperatures over 800ºC and 700ºC for 17-4 and 13-8+Mo, respectively. Thus, much of the hardening and softening that occurs during welding thermal cycles can be modeled using the results from this study. However, more information is needed to predict the behavior in the partially softened region. At temperatures between 650ºC and 800ºC in 17-4 and 600ºC and 700ºC in 13-8+Mo, partial softening was observed. This softening could be the result of precipitate coarsening, precipitate dissolution, martensite recovery, austenite reversion or a combination of these factors[7,13,27,46,58]. Advanced characterization of the samples that have been subjected to temperatures within these ranges would be required to determine which of these factors are responsible for the observed softening in each system. Techniques such as atom probe tomography (APT) and transmission electron microscopy (TEM) could be employed to investigate the significance of austenite formation and changes to the dislocation density. Furthermore, if precipitate coarsening is occurring and the particles have increased in size and lost coherency with the matrix they may be observable using TEM.

Finally, controlled weld metal deposition can be performed using the optimal heat inputs and weld bead overlaps determined in this work. Filler metal was not used in the current investigation thus, future work should include pad welding experiments using different filler metal overlap and heat inputs. Hardness mapping could then be performed to estimate the extent of precipitate growth and dissolution. Furthermore, other software packages such as Sysweld could be investigated and compared to the hardness mapping results and predicted SmartWeld isotherms from this study.

5.2 Implications

The testing conditions used in the current investigation were chosen to represent welding processes. It was observed that the precipitation response in these alloys is dependent on the testing conditions and the starting condition of the material. Thus, comparing the results obtained here with previous works can aid in developing a better understanding how precipitation occurs in these alloys and maraging systems in general.

Furthermore, the results obtained in this work are the first step towards the development of a controlled weld metal deposition model for these materials. The benefit of developing a model for controlled weld metal deposition is the possibility of eliminating the need for costly PWHT's. It should also be noted that even if the base metal strength cannot be fully retained throughout the heat affected zone (HAZ) and (FZ), this model would still provide a method for maximizing the strength with respect to welds that are made without consideration for precipitation and bead placement. Successful development of this model will have significant implications for additive manufacturing (AM) of these materials. AM and multi-pass welding both result in the formation of a FZ and HAZ, though on different scales. The high energy density associated with the AM processes results in a smaller FZ and HAZ than fusion welding processes, but the temperatures associated with each will be the same[33]. Therefore, with some refinement the model could be applied to AM processing as well.

Tables

Table 1: Properties of Ti-6Al-4V and PH alloys. All Values taken from CES EduPak 2016[4].

Material	13-8+Mo	17-4	Ti-6Al-4V
Yield Strength (MPa)	1090	1085	855
Density (kg/m^3)	7695	7805	4428
Specific Strength (N*m/kg)	0.14	0.14	0.19
Price (USD/lb)	3.24-3.5	2.85-2.96	9.21-10.2

Table 2: Typical cast composition of 17-4 and 13-8+Mo. All values are in weight percent.

	Fe	Cr	Ni	C	Mn	Cu	Mo	Al	Si	P	S	Nb
17-4	Bal.	16.24	3.96	0.03	0.49	3.00	0.11	0.00	0.75	0.02	0.01	0.20
13-8+Mo	Bal.	12.70	7.87	0.03	0.16	0.05	2.23	1.14	0.21	0.01	0.01	0.00

Table 3: Cross-weld tensile test results for 17-4 and 13-8+Mo GMA welds, welded in both conditions[20].

Sample	Yield Strength (MPa)	Tensile Strength (MPa)	% of Base Metal Yield Strength Retained
17-4 Base Metal	1076	1141	N/A
17-4 S-A-W	770	841	72%
17-4 S-W-A	1004	1098	94%
13-8+Mo Base Metal	1092	1181	N/A
13-8+Mo S-A-W	828	1002	76%
13-8+Mo S-W-A	1016	1165	93%

Table 4: Chemical composition of PH 17-4 and PH 13-8+Mo used in the Gleeble simulated multi-pass welding study. All values in weight percent.

	Fe	Cr	Ni	C	Mn	Cu	Mo	Al	Si	P	S	Nb
17-4	Bal.	16.08	4.09	0.03	0.41	3.02	0.21	0.00	0.83	0.03	0.01	0.20
13-8+Mo	Bal.	12.71	7.90	0.06	0.19	0.13	2.27	0.77	0.22	0.01	0.31	0.00

Table 5: Weld thermal cycle peak temperature combinations used in this study.

Material	Primary Thermal Cycle Peak Temperature (ºC)	Secondary Thermal Cycle Peak Temperature (ºC)	Tertiary Thermal Cycle Peak Temperature (ºC)
17-4	650	X	X
17-4	875	650	X
17-4	1150	650	X
17-4	1150	875	X
17-4	1300	1150	650
17-4	1300	1150	875
13-8+Mo	650	X	X
13-8+Mo	875	650	X
13-8+Mo	1150	650	X
13-8+Mo	1150	850	X
13-8+Mo	1300	1150	650
13-8+Mo	1300	1150	850

Table 6: Chemical composition of PH 17-4 and PH 13-8+Mo used in the precipitate kinetics study. All values in weight percent.

	Fe	Cr	Ni	C	Mn	Cu	Mo	Al	Si	P	S	Nb	Ta	N
17-4	Bal.	15.11	4.16	0.03	0.81	3.61	0.07	0.00	0.38	0.022	0.022	0.24	0.02	0.036
13-8+Mo	Bal.	12.58	8.19	0.04	0.04	0.00	2.12	1.04	0.08	0.005	0.001	0	0	0.002

Table 7: Calculated apparent activation energies taken from literature on 17-4 and 13-8+Mo.

Alloy	Q (kJ/mol)	Measuring Method	Conditions	Authors
13-8+Mo	139	Hardness and Avrami	Solution Treated Material and Aging Heat Treatments	Robino et al.[15]
17-4	262	Hardness and Avrami	Solution Treated Material and Aging Heat Treatments	Mirzadeh and Najafizadeh[16]
17-4	190-215	Dilatometry	Solution Treated Material and Aging Heat Treatments	Rivolta and Gerosa[49]
17-4	112	Resistivity Analysis	Solution Treated Material and Aging Heat Treatments	Viswanathan *et al.*[46]

Table 8: Semi-Quantitative XRD results for select samples of 17-4 and 13-8+Mo used in secondary heating experiments.

Sample	**% FCC**
Peak Aged 17-4 BM	0%
Peak Aged 17-4 BM + 1100ºC Peak Temp	0%
Peak Aged 17-4 BM + 1100ºC Peak Temp with no hold + 650ºC Peak Temp with no hold	4%
Peak Aged 17-4 BM + 1100ºC Peak Temp with no hold + 650ºC Peak Temp for 60 Seconds	5%
Peak Aged 17-4 BM + 1100ºC Peak Temp with no hold + 700ºC Peak Temp for 5 Seconds	4%
Peak Aged 13-8+Mo BM	0%
Peak Aged 13-8+Mo BM + 1100ºC Peak Temp	3%
Peak Aged 13-8+Mo BM + 1100ºC Peak Temp with no hold + 650ºC Peak Temp for 60 Seconds	3%
Peak Aged 13-8+Mo BM + 1100ºC Peak Temp with no hold + 650ºC Peak Temp for 120 Seconds	4%

Table 9: Chemical composition of PH 17-4 and PH 13-8+Mo used in the dual pass GTAW study. All values in weight.

	Fe	Cr	Ni	C	Mn	Cu	Mo	Al	Si	P	S	Nb	N
17-4	Bal.	15.25	4.44	0.027	0.65	3.11	0.14	0.00	0.4	0.02	0.003	0.24	0.018
13-8+Mo	Bal.	12.66	8.19	0.04	0.04	0	2.31	1.04	0.06	0.004	0.002	0	0.003

Figures

Figure 1: M88 military combat vehicle currently plated with Ti-6Al-4V.

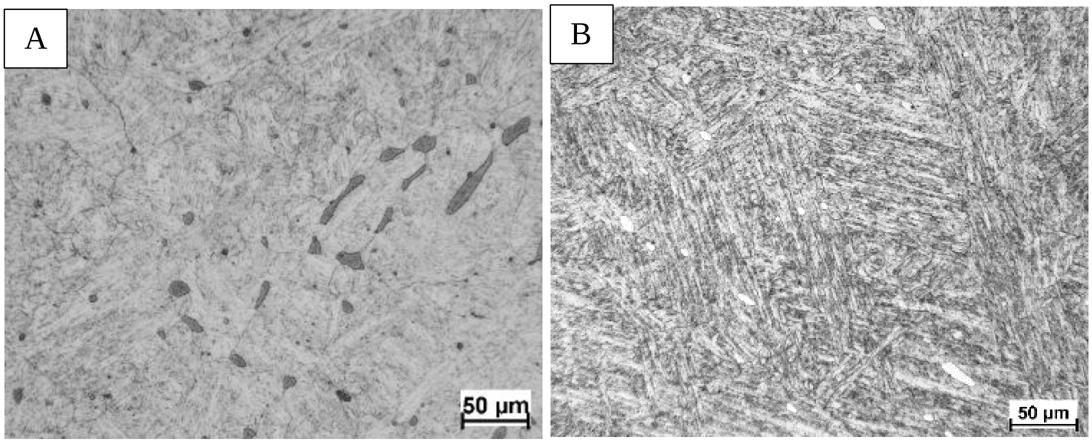

Figure 2: LOM image of the cast and heat treated microstructure of (A) 17-4 and (B) 13-8+Mo.

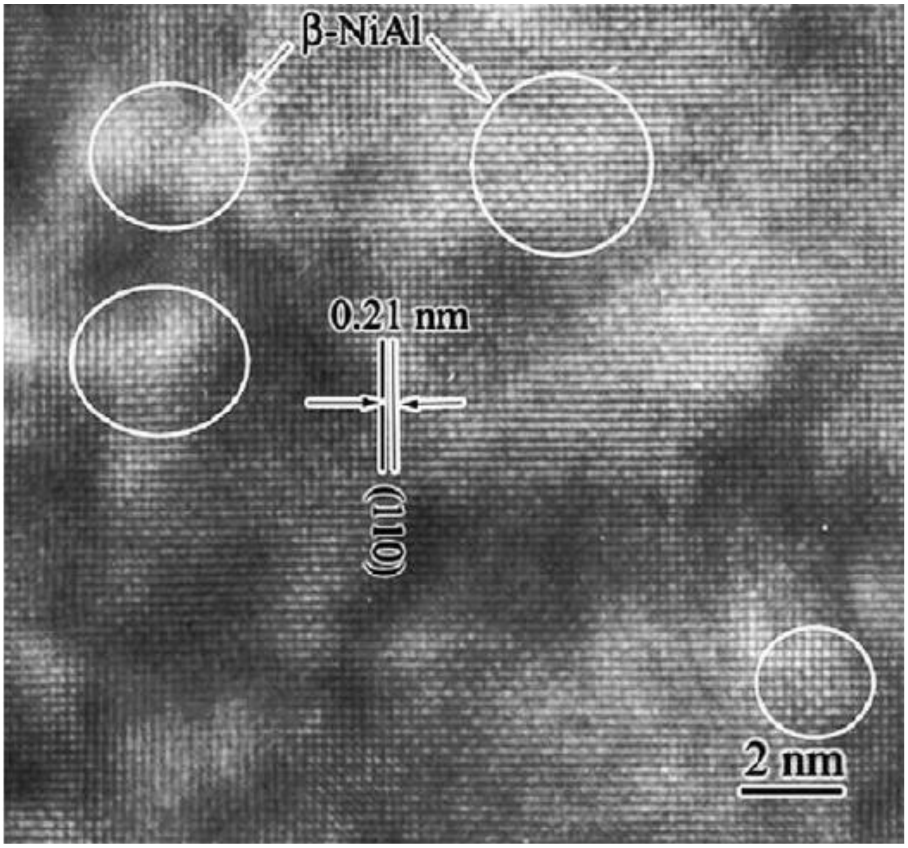

Figure 3: High resolution TEM image of coherent β-NiAl precipitates in a martensite matrix[12].

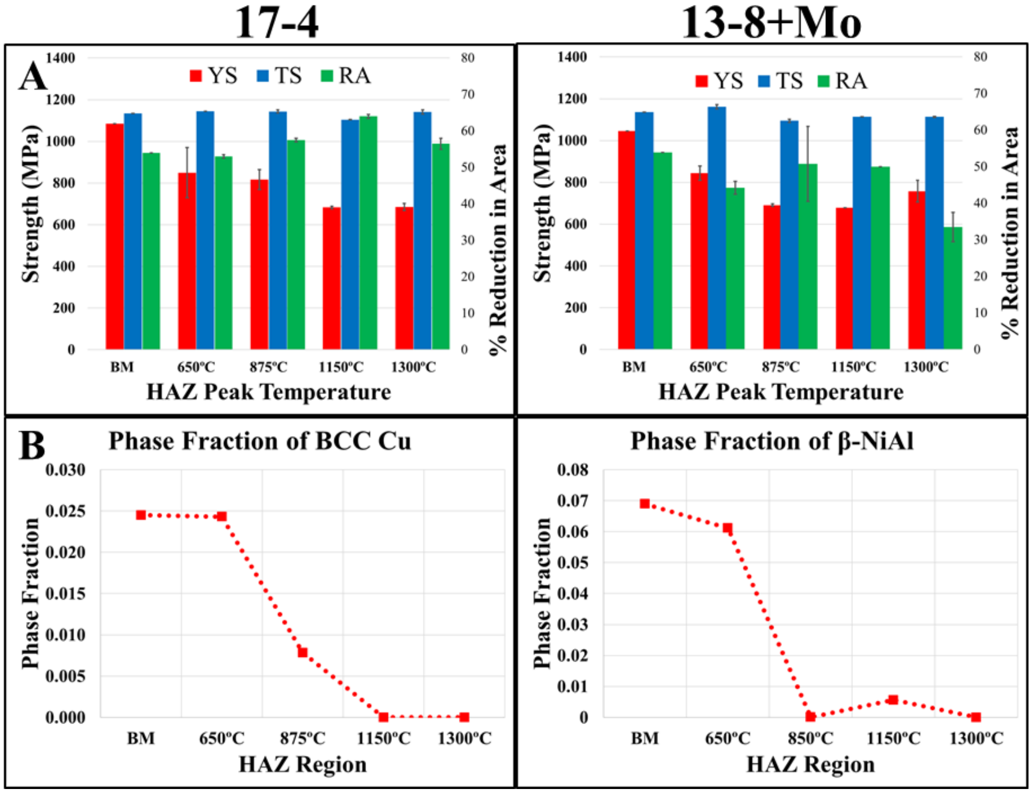

Figure 4: (A) Tensile results for Gleeble HAZ samples welded in the aged condition (B) MatCalc predicted phase fraction of strengthening precipitates[20].

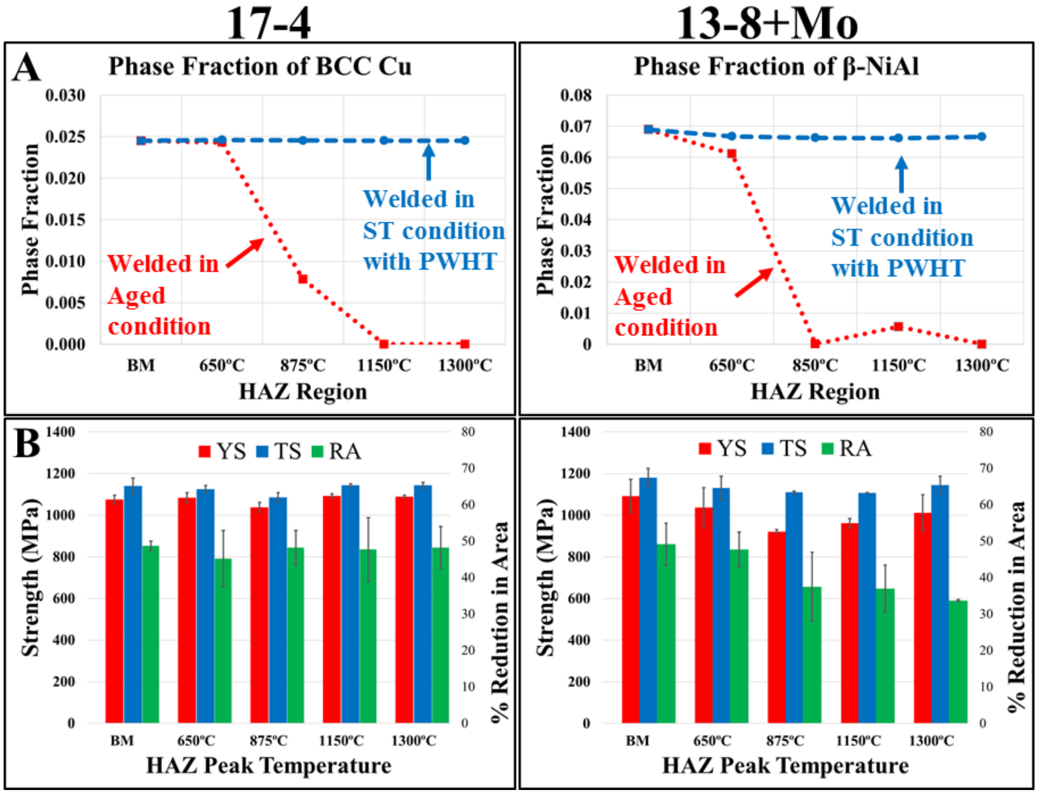

Figure 5: (A) MatCalc predicted phase fraction of strengthening precipitates (B) Tensile results for Gleeble HAZ samples with optimized welding procedures[20].

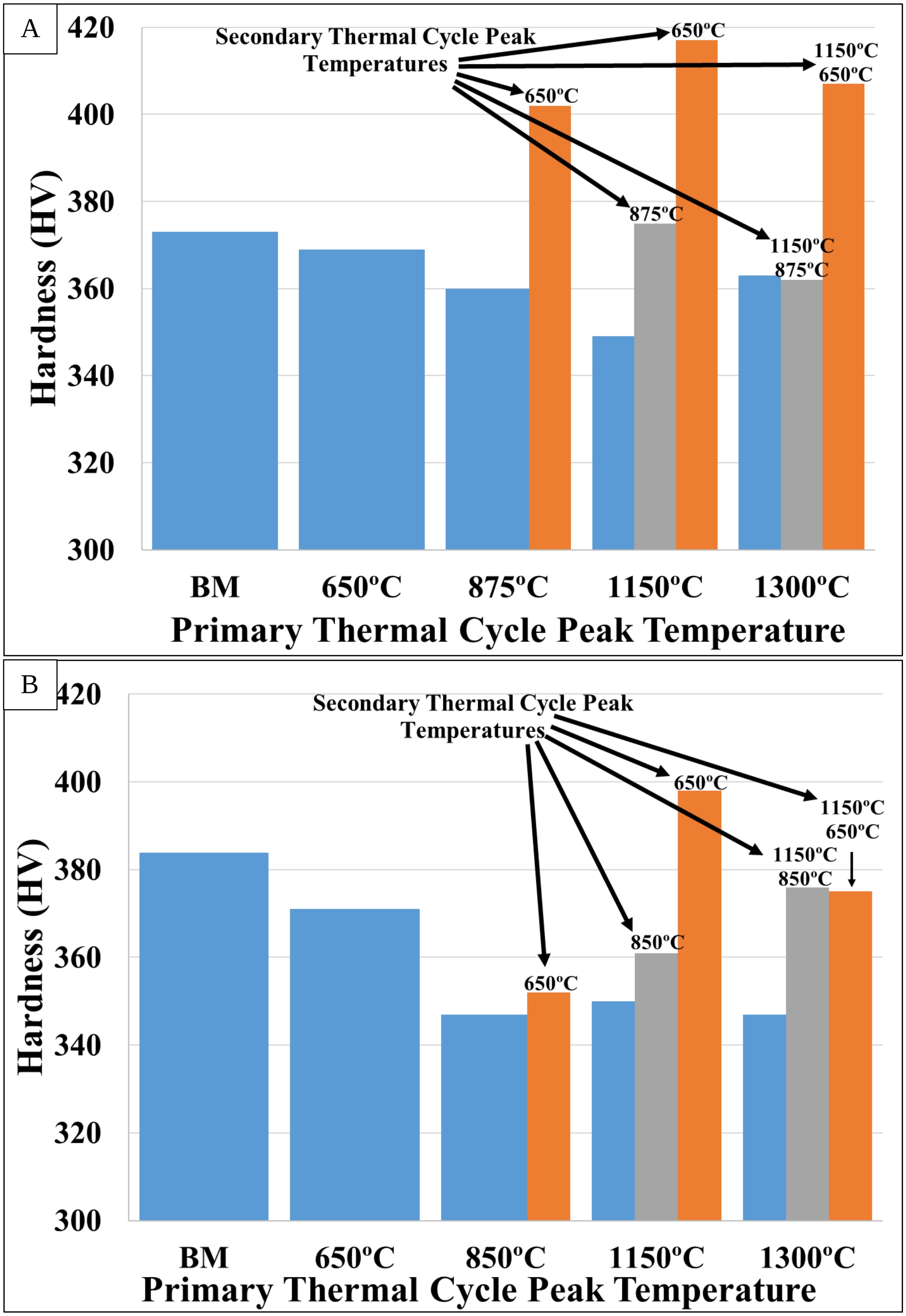

Figure 6: Hardness data for 2000 J/mm heat input Gleeble multi-pass welding simulations blue bars indicate primary welding thermal cycles, orange and gray correlate to secondary welding thermal cycles. (A) 17-4 (B) 13-8+Mo.

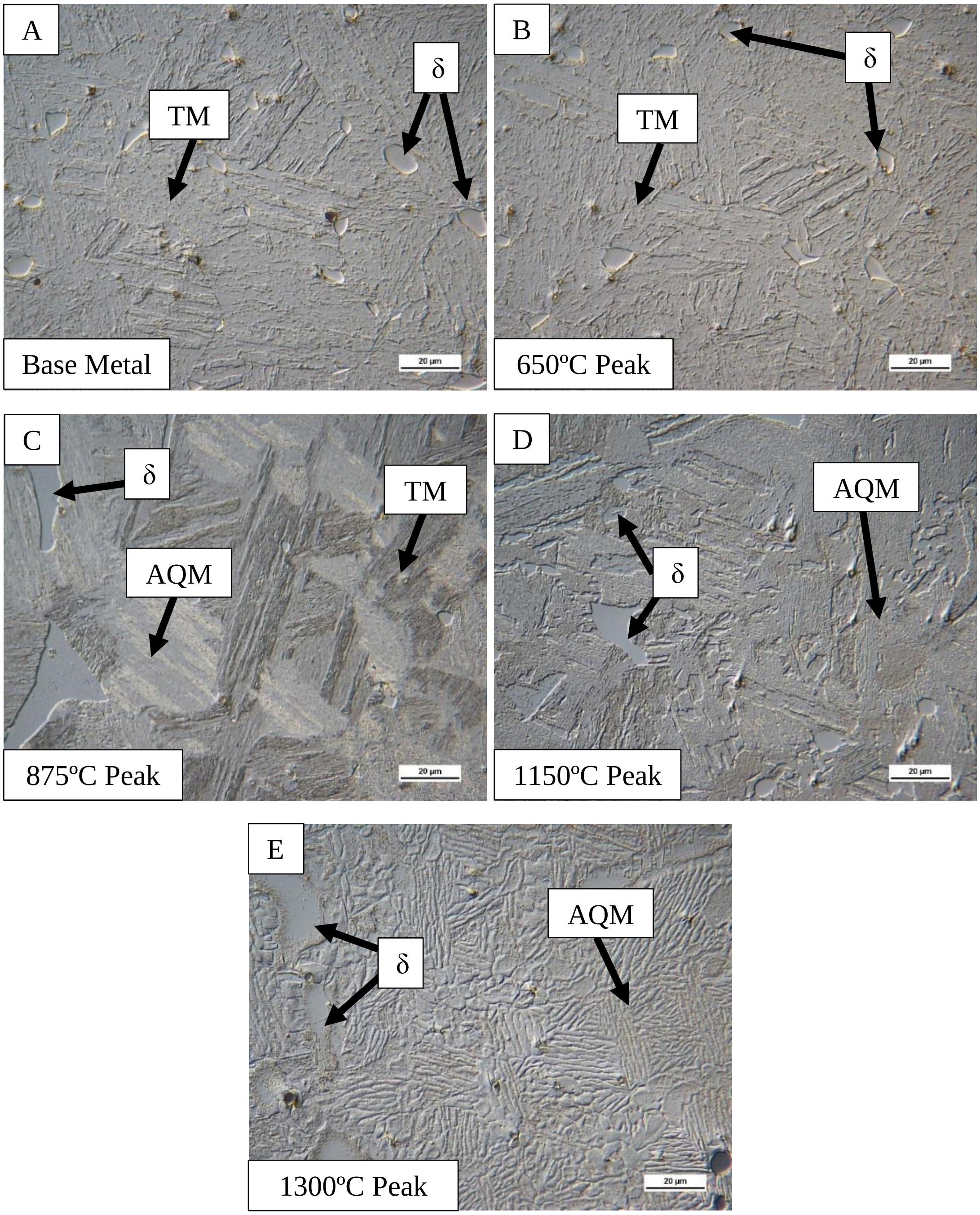

Figure 7: Light optical photomicrographs of 17-4 (A) base metal and after a (B) 650ºC, (C) 875ºC, (D) 1150ºC and (E) 1300ºC thermal cycle. TM=Tempered Martensite, δ = Delta Ferrite, AQM = As-Quenched Martensite.

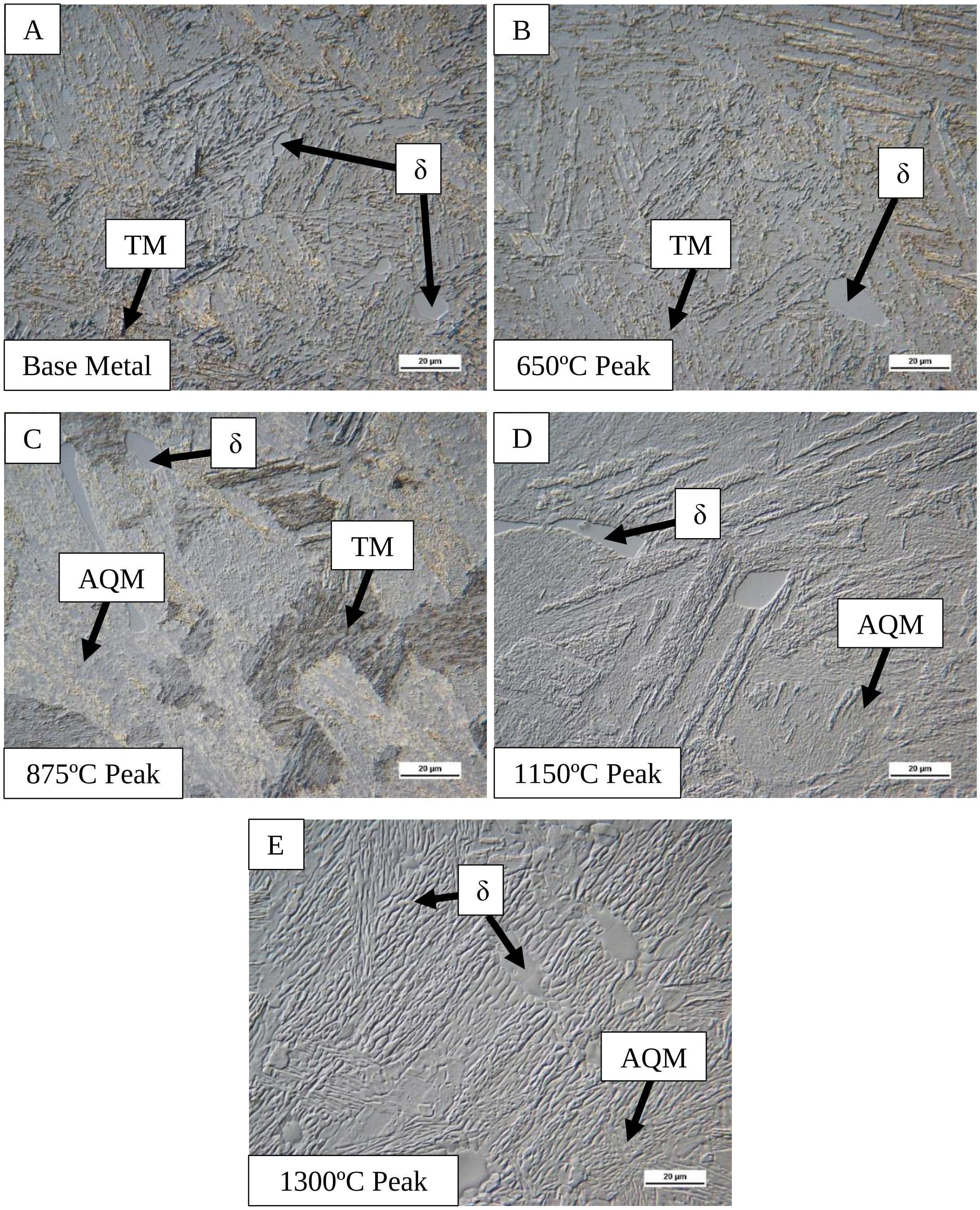

Figure 8: Light optical photomicrographs of 13-8+Mo (A) base metal and after a (B) 650ºC, (C) 850ºC, (D) 1150ºC and (E) 1300ºC thermal cycle TM=Tempered Martensite, δ = Delta Ferrite, AQM = As-Quenched Martensite.

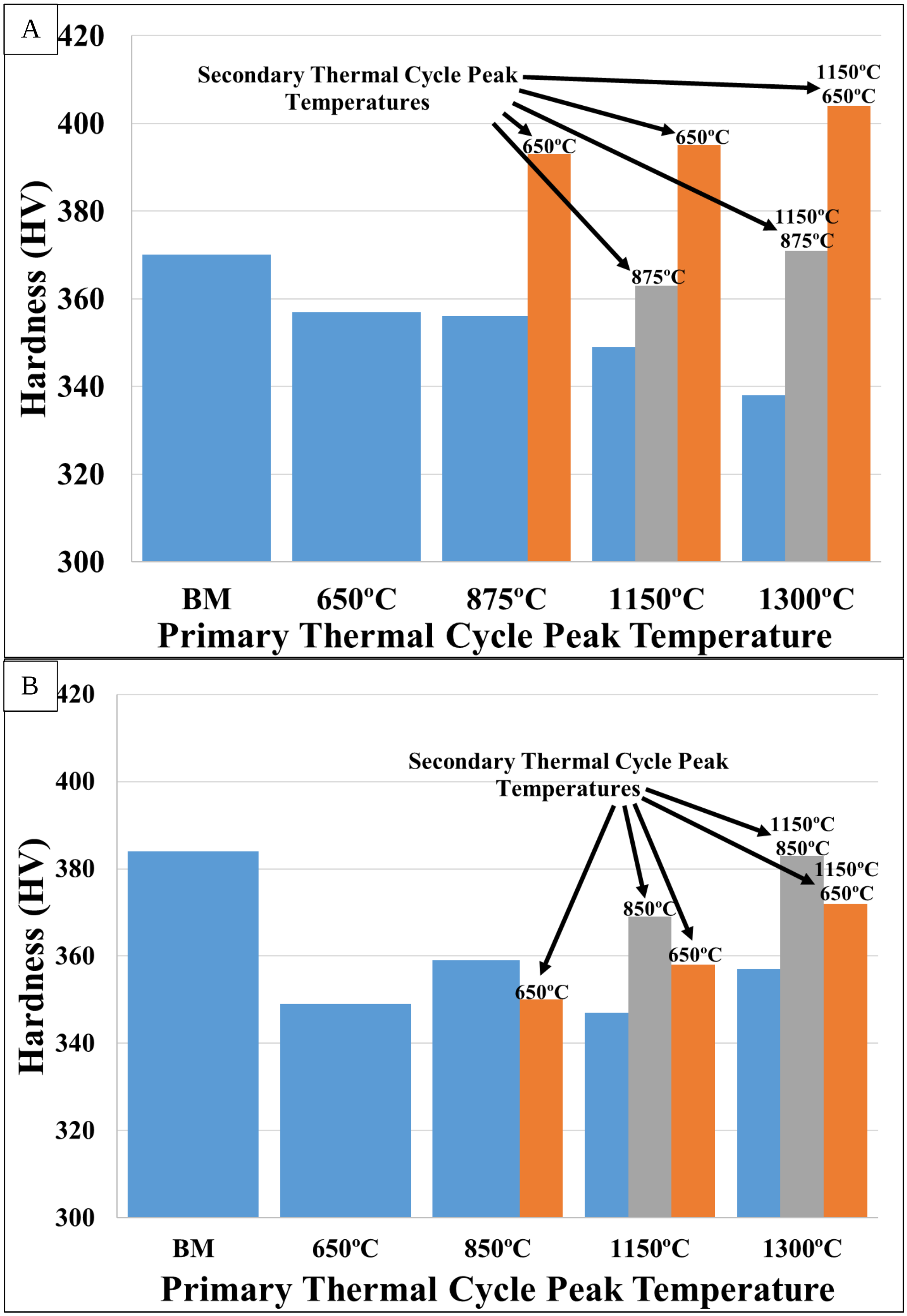

Figure 9: Hardness data for 1000 J/mm heat input Gleeble multi-pass welding simulations blue bars indicate primary welding thermal cycles, orange and gray correlate to secondary welding thermal cycles. (A) 17-4 (B) 13-8+Mo.

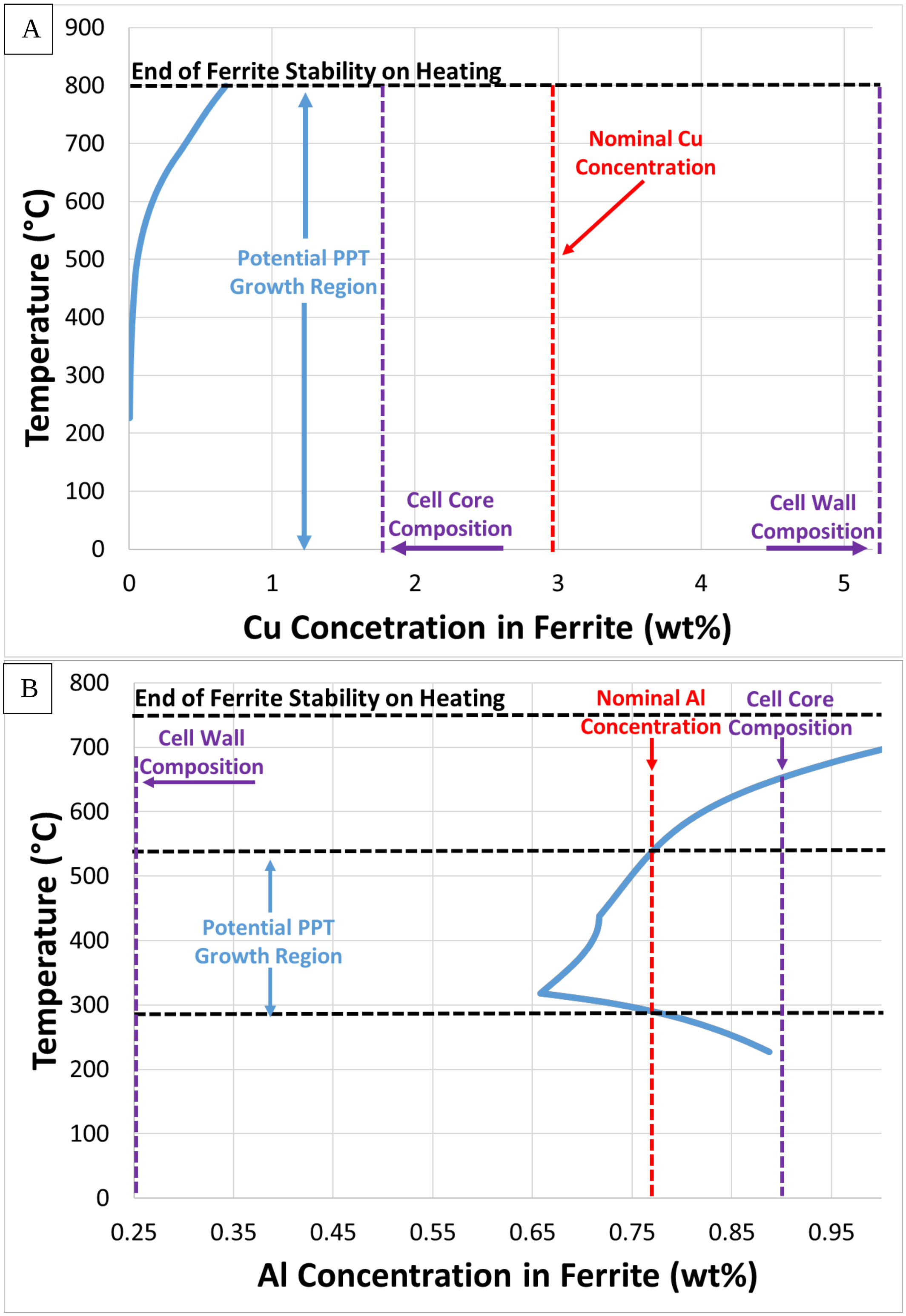

Figure 10: ThermoCalc equilibrium diagrams showing calculated solubility for (A) Cu in 17-4 and (B) Al in 13-8+Mo.

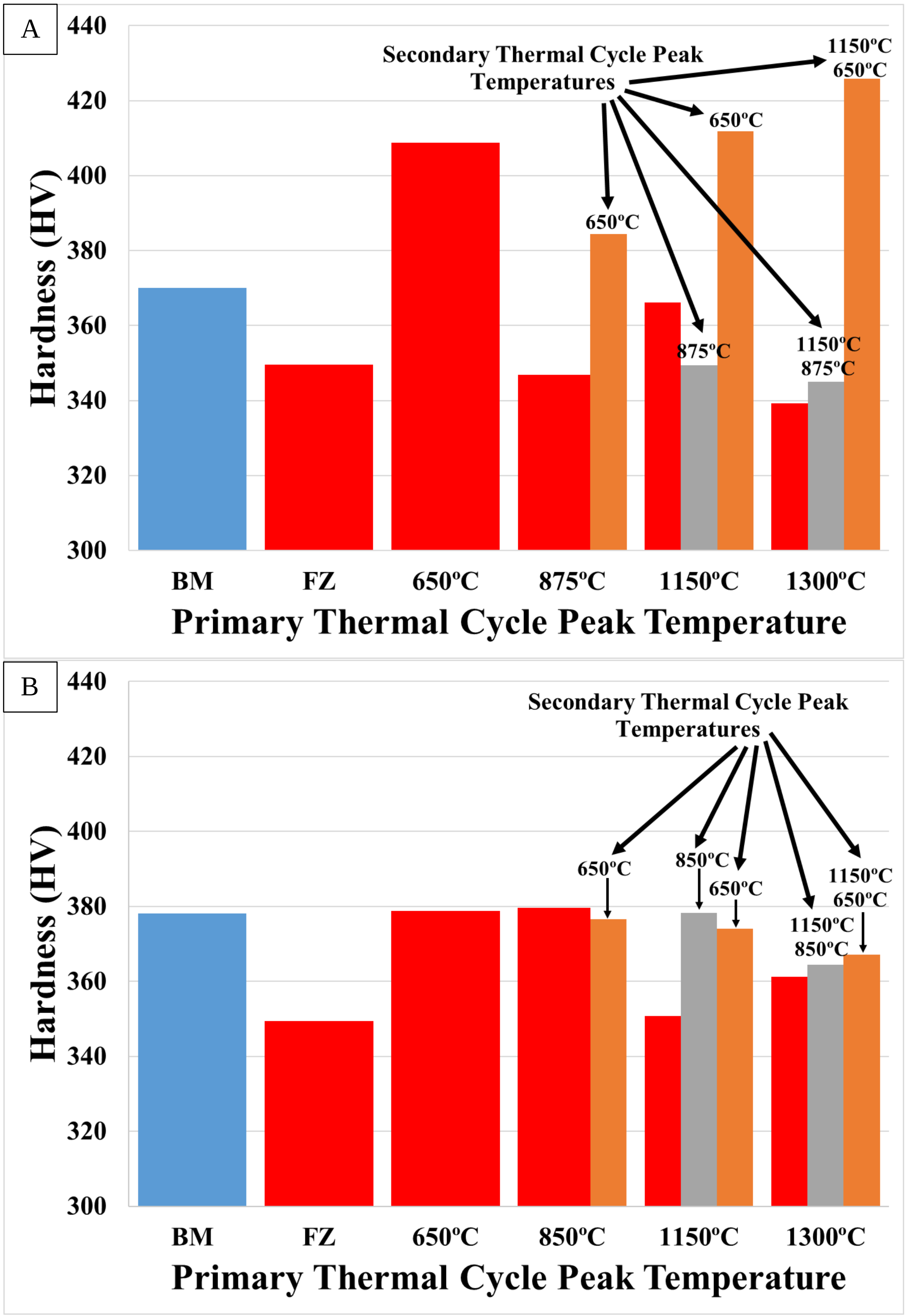

Figure 11: Hardness data for Gleeble multi-pass welding simulations. Red bars represent the as-welded fusion zone and fusion zone after primary welding thermal cycles. Orange and gray correlate to secondary welding thermal cycles. Blue is the age hardened base metal. (A) 17-4 (B) 13-8+Mo.

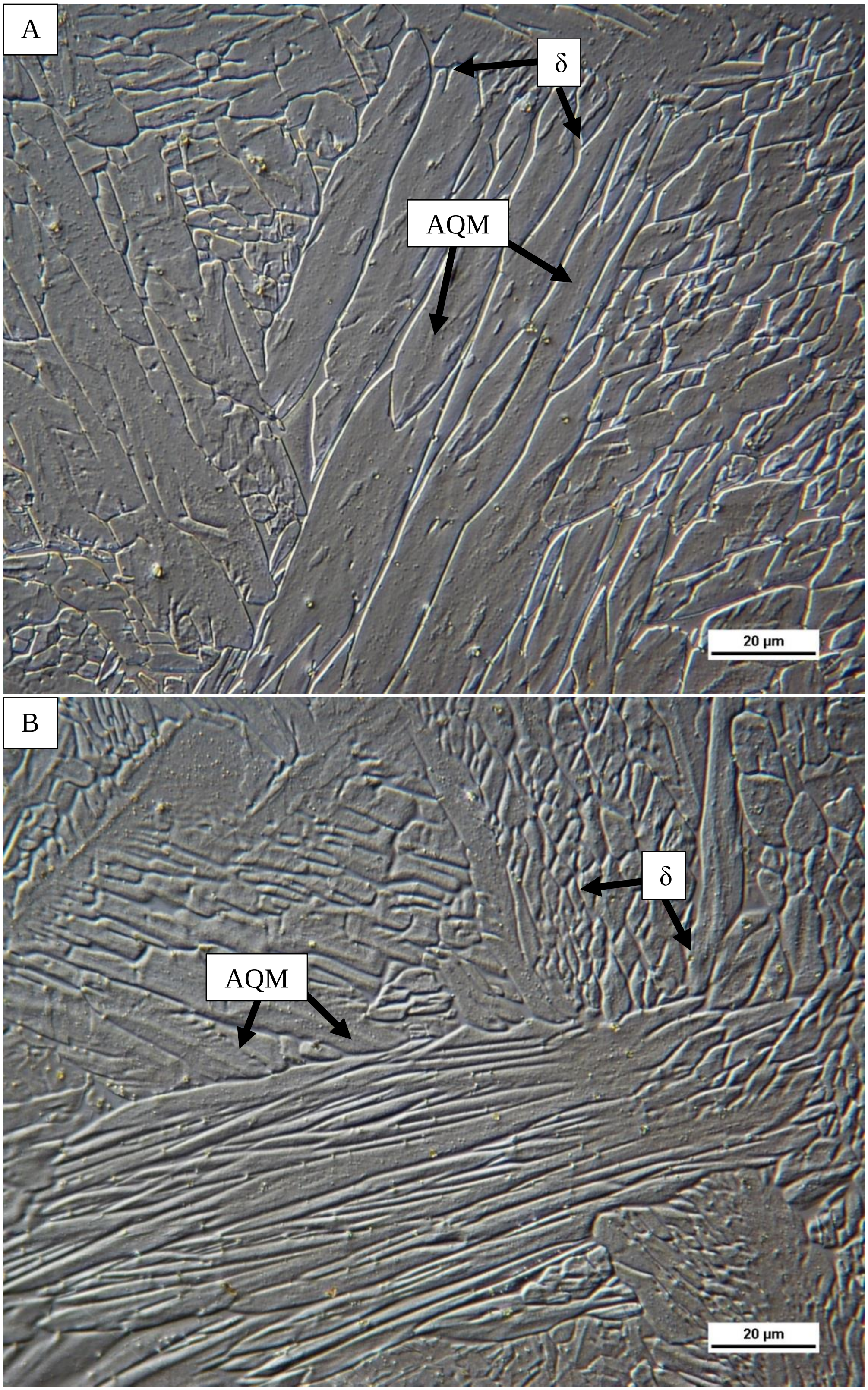

Figure 12: Weld metal microstructure of (A) 17-4 and (B) 13-8+Mo prior to Gleeble simulation AQM = As-Quenched Martensite, δ = δ-Ferrite.

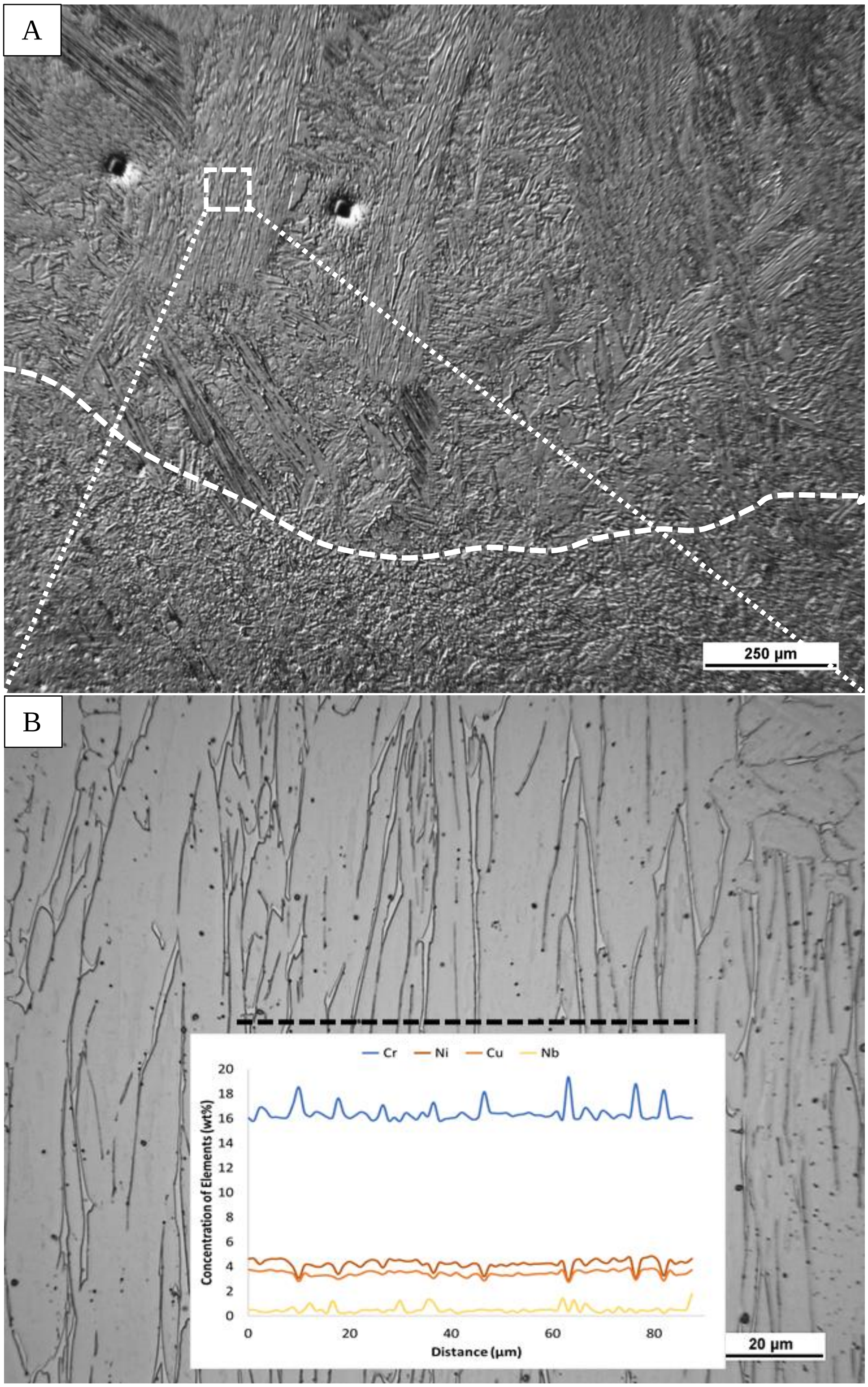

Figure 13: (A) Light optical micrograph of 17-4 weld metal showing the location of an EDS line scan. (B) High magnification image and plot of composition as a function of distance along the line in the micrograph measured using EDS.

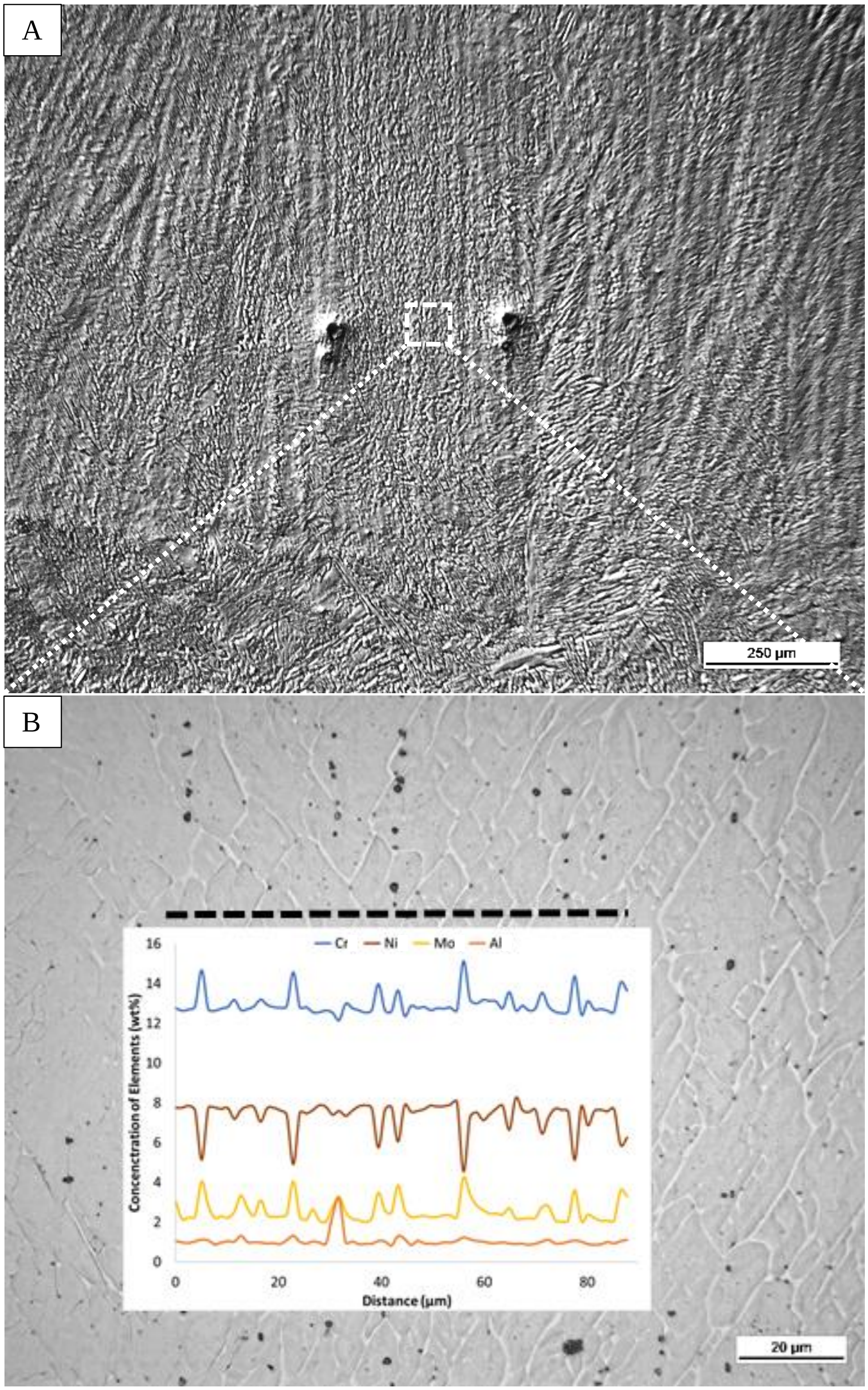

Figure 14: (A) Light optical photomicrographs of 13-8+Mo weld metal showing the location of an EDS line scan (B) High magnification image and plot of composition as a function of distance along the line in the micrograph measured using EDS.

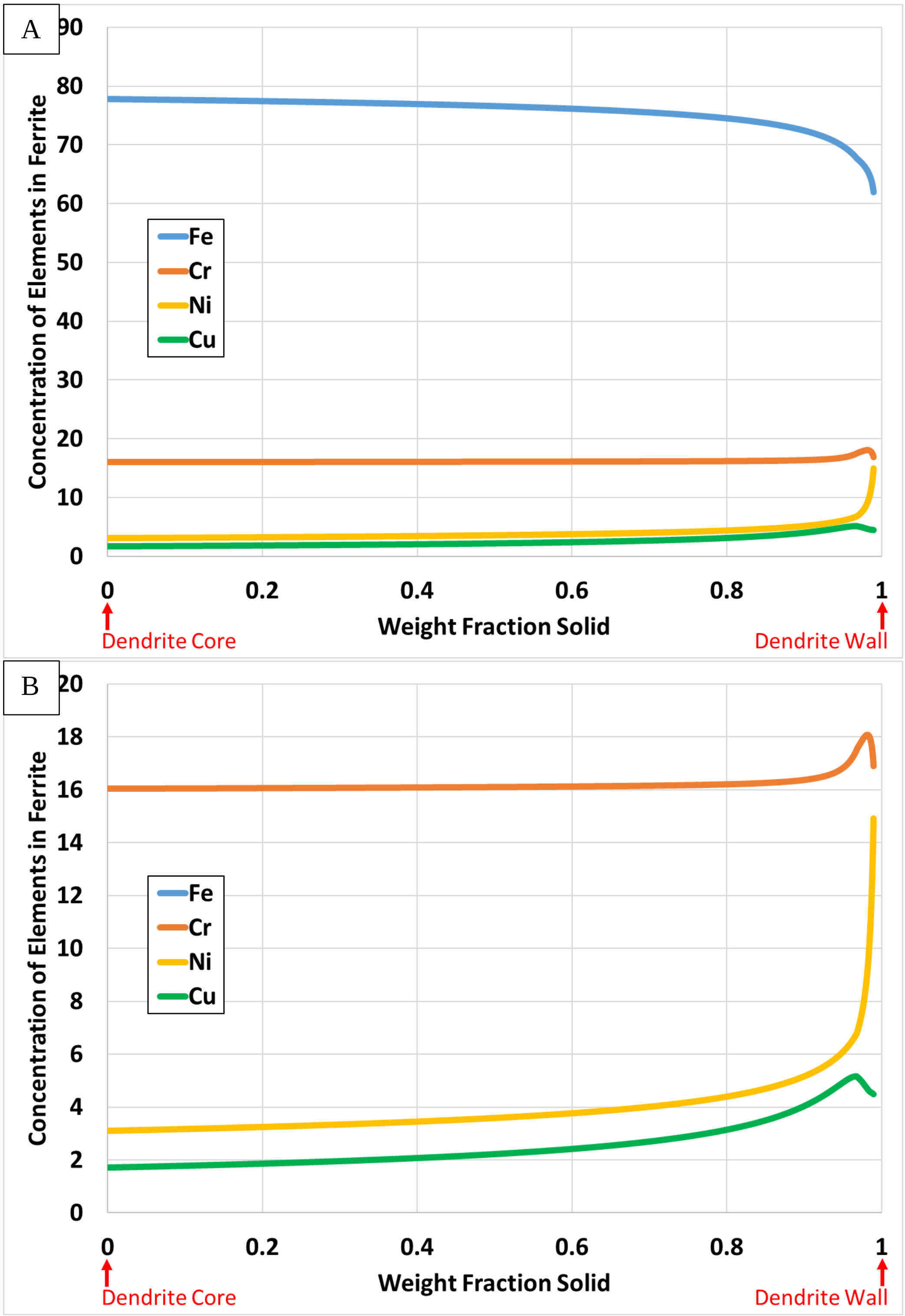

Figure 15: ThermoCalc solidification simulation for 17-4 demonstrating composition as a function of fraction solid in Ferrite for (A) All elements and (B) Minor elements.

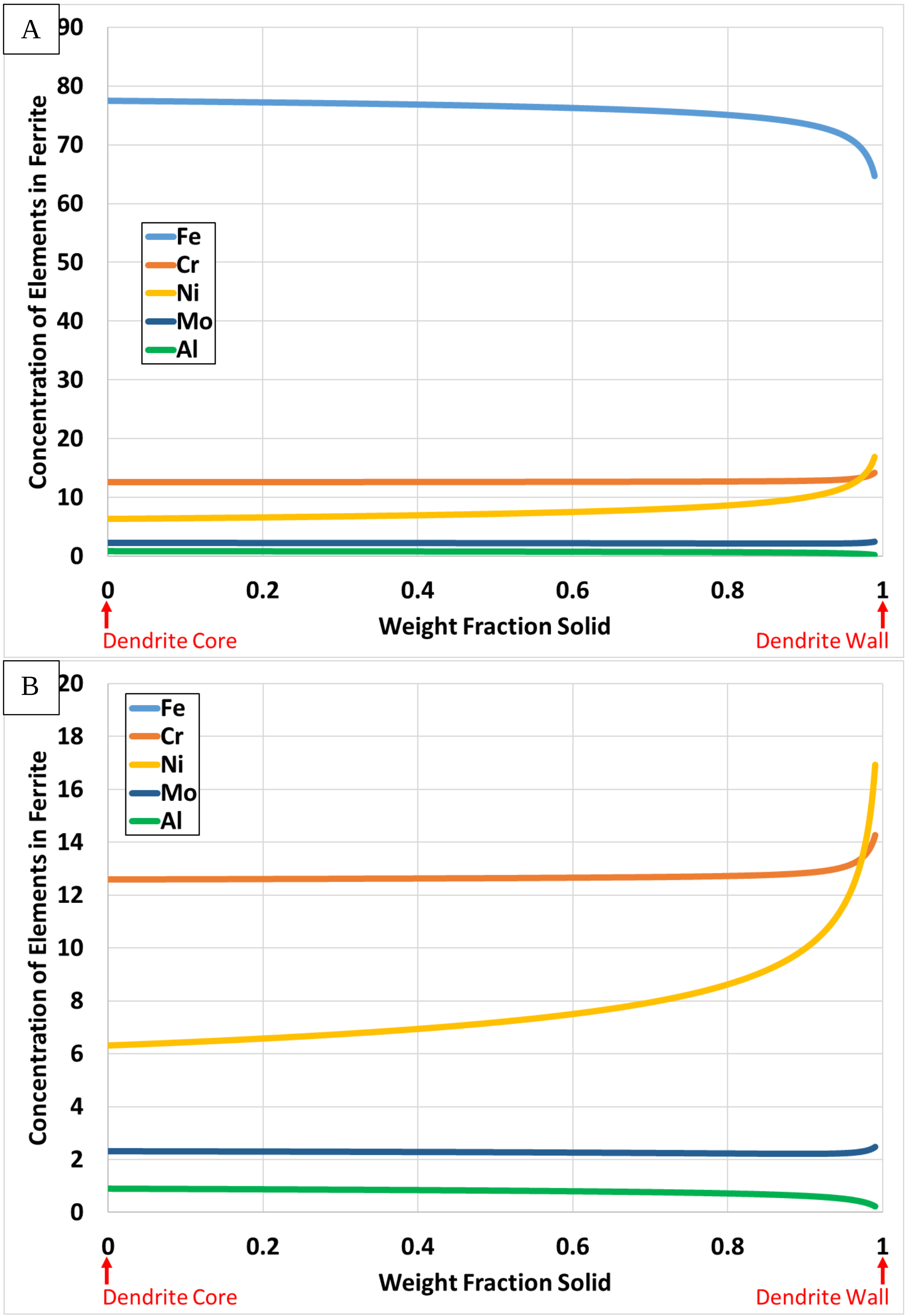

Figure 16: ThermoCalc solidification simulation for 13-8+Mo demonstrating composition as a function of fraction solid in Ferrite for (A) All elements and (B) Minor elements.

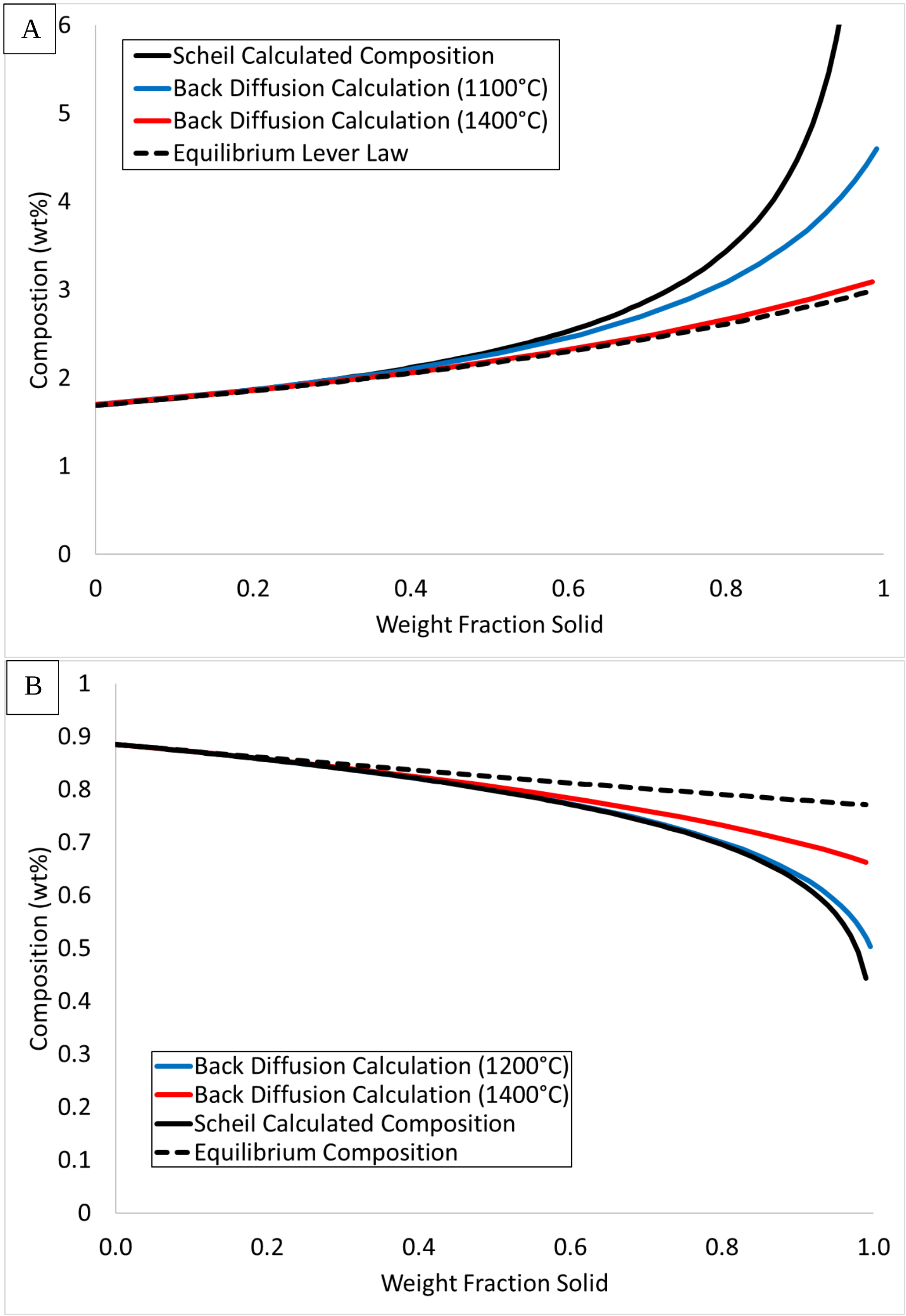

Figure 17: Estimated back diffusion per Eq. [1a] for (A) Cu in 17-4 and (B) Al in 13-8+Mo.

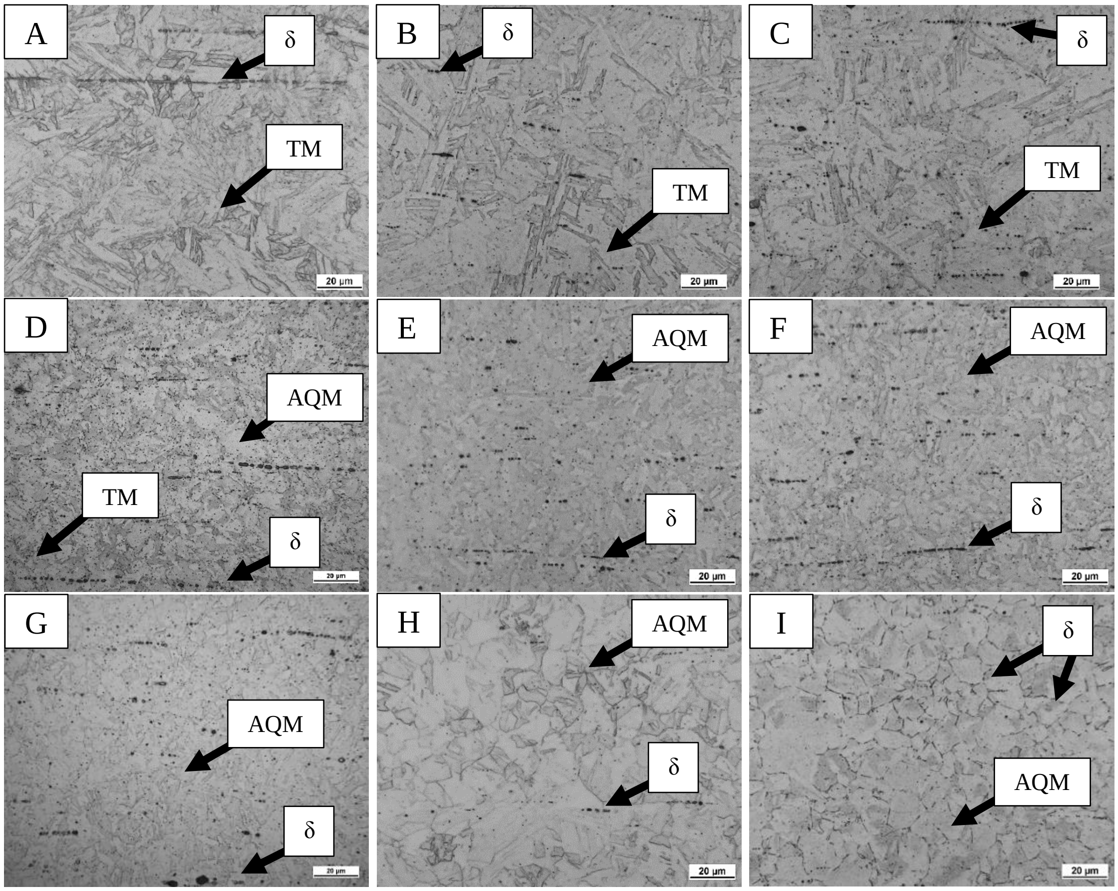

Figure 18: Light optical photomicrographs of 17-4 dissolution Gleeble samples heated to various temperatures with no hold time. (A) Base Metal (B) 600ºC (C) 700ºC (D) 800ºC (E) 900ºC (F) 1000ºC (G) 1100ºC (H) 1200ºC (I) 1300ºC. TM=Tempered Martensite, δ = Delta Ferrite, AQM = As-Quenched Martensite.

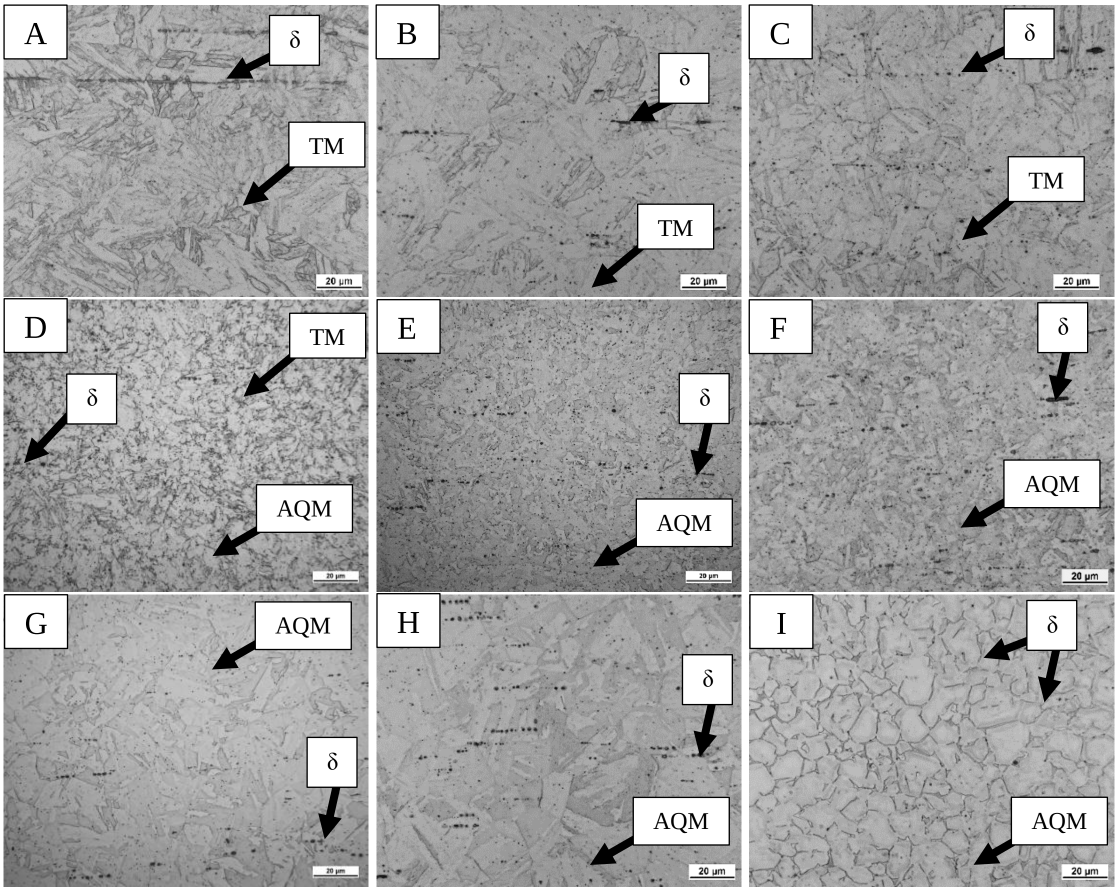

Figure 19: Light optical photomicrographs of 17-4 dissolution Gleeble samples heated to various temperatures with 5 second hold time. (A) Base Metal (B) 600ºC (C) 700ºC (D) 800ºC (E) 900ºC (F) 1000ºC (G) 1100ºC (H) 1200ºC (I) 1300ºC TM=Tempered Martensite, δ = Delta Ferrite, AQM = As-Quenched Martensite.

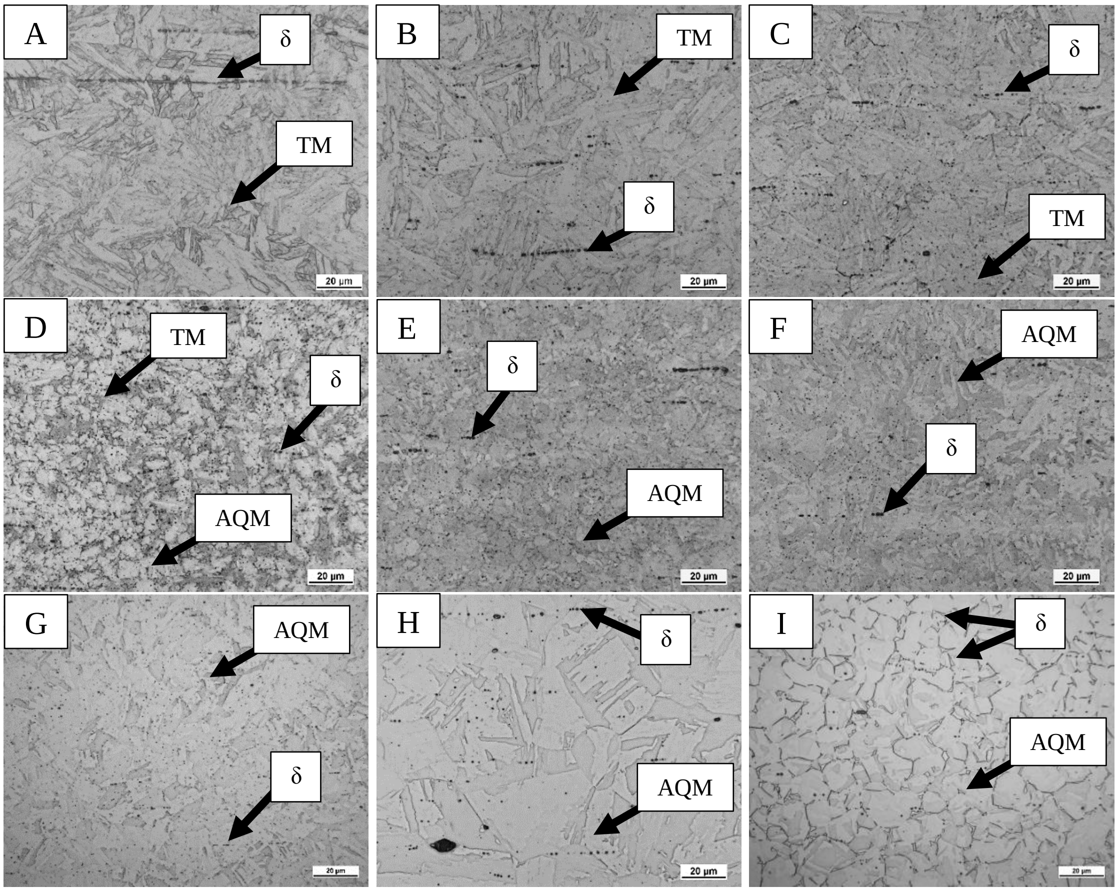

Figure 20: Light optical photomicrographs of 17-4 dissolution Gleeble samples heated to various temperatures with 10 second hold time. (A) Base Metal (B) 600ºC (C) 700ºC (D) 800ºC (E) 900ºC (F) 1000ºC (G) 1100ºC (H) 1200ºC (I) 1300ºC. TM=Tempered Martensite, δ = Delta Ferrite, AQM = As-Quenched Martensite.

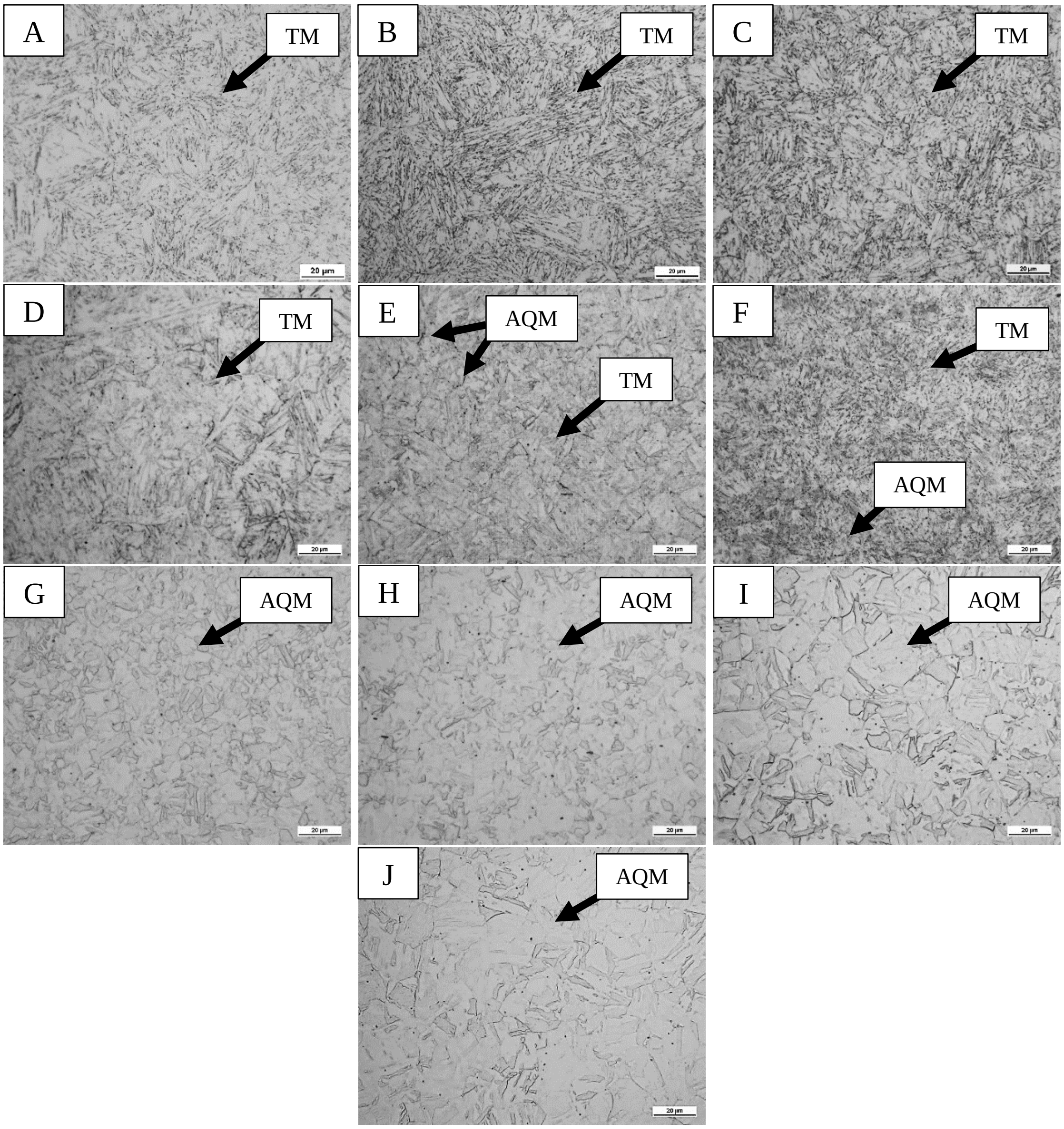

Figure 21: Light optical photomicrographs of 13-8+Mo dissolution Gleeble samples heated to various temperatures with no hold. (A) Base Metal (B) 500ºC (C) 600ºC (D) 700ºC (E) 800ºC (F) 900ºC (G) 1000ºC (H) 1100ºC (I) 1200ºC (J) 1300ºC. TM=Tempered Martensite, AQM = As-Quenched Martensite.

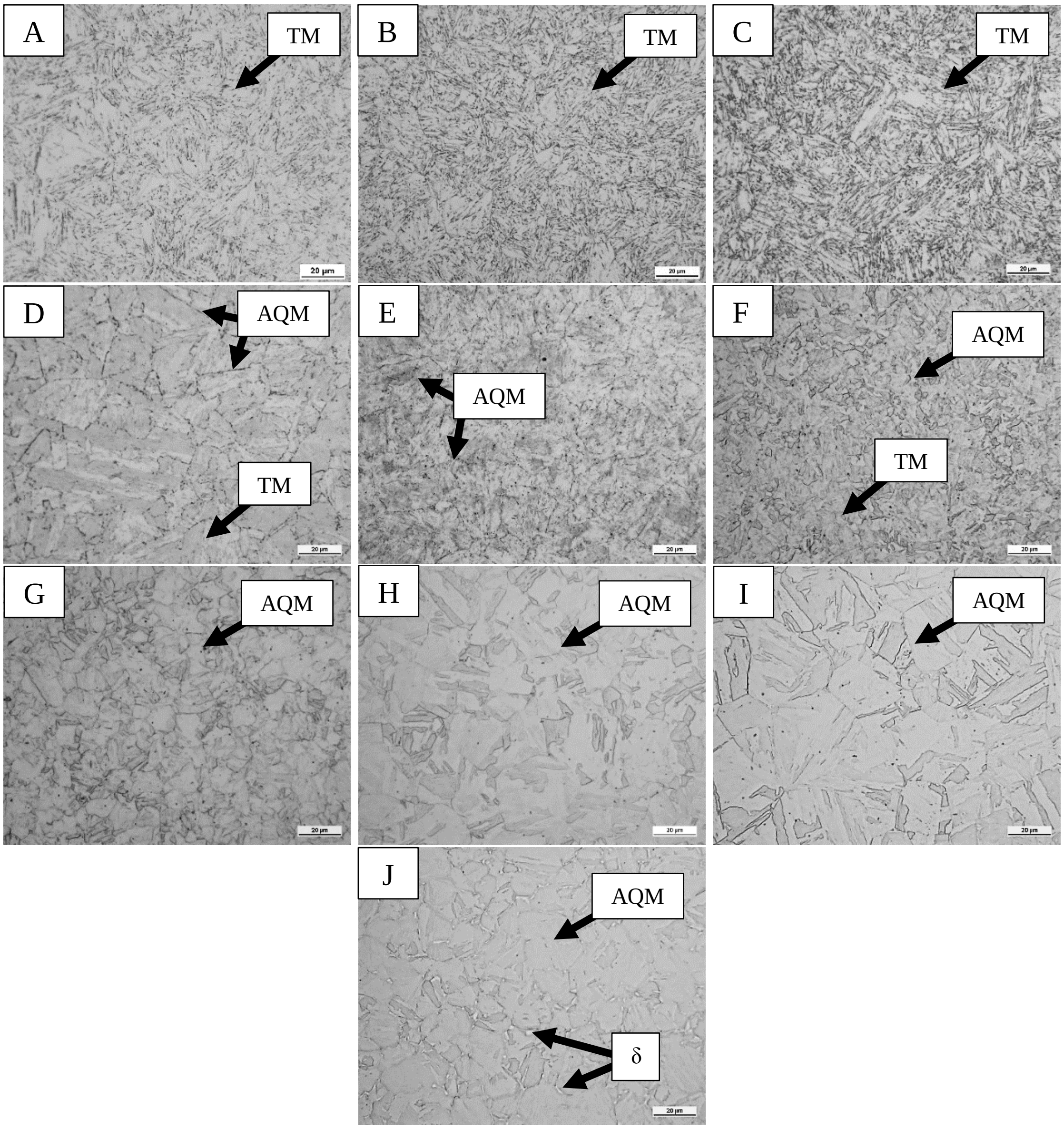

Figure 22: Light optical photomicrographs of 13-8+Mo dissolution Gleeble samples heated to various temperatures with 5 second hold time. (A) Base Metal (B) 500ºC (C) 600ºC (D) 700ºC (E) 800ºC (F) 900ºC (G) 1000ºC (H) 1100ºC (I) 1200ºC (J) 1300ºC. TM=Tempered Martensite, δ = Delta Ferrite, AQM = As-Quenched Martensite.

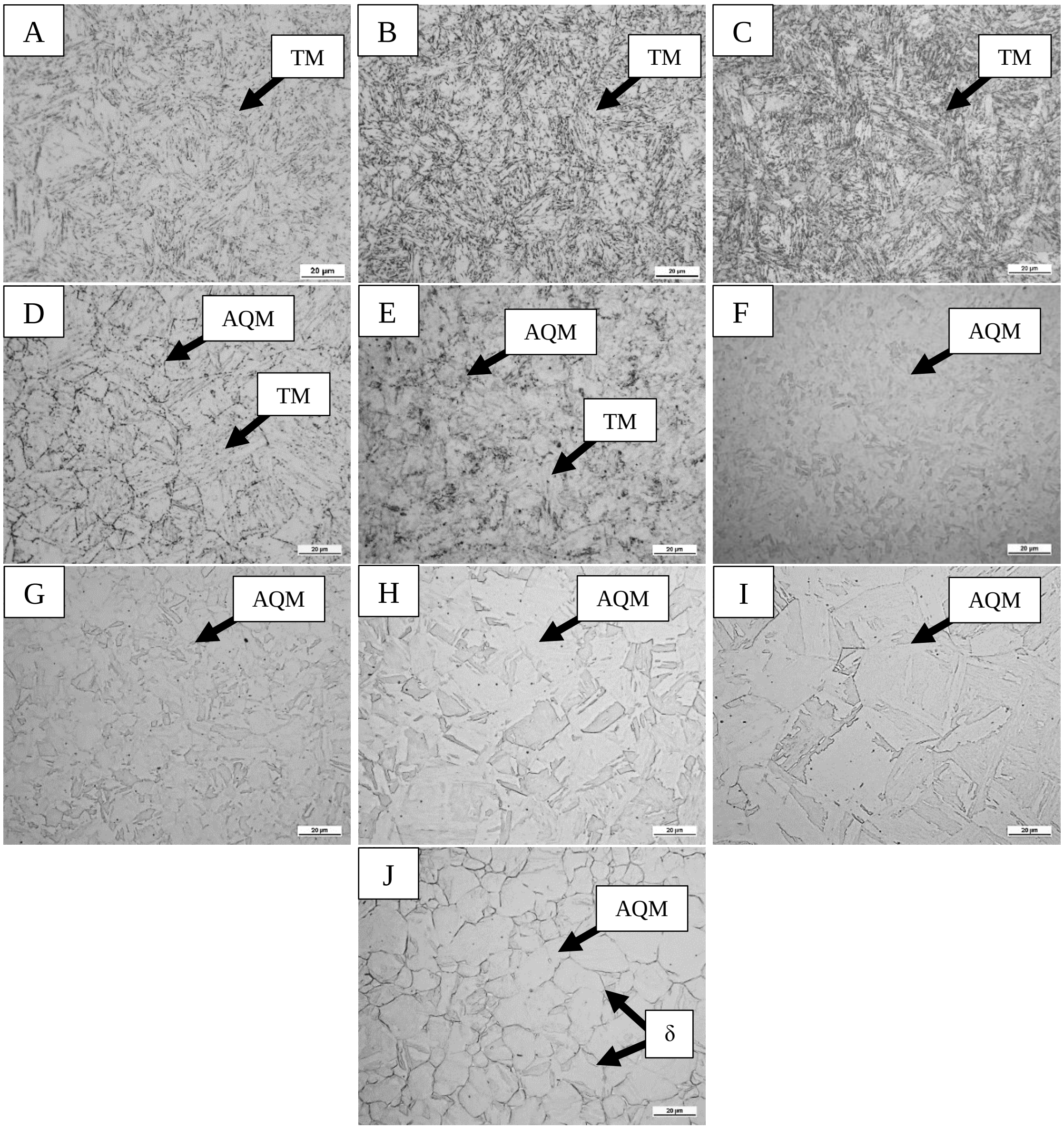

Figure 23: Light optical photomicrographs of 13-8+Mo dissolution Gleeble samples heated to various temperatures with 10 second hold time. (A) Base Metal (B) 500ºC (C) 600ºC (D) 700ºC (E) 800ºC (F) 900ºC (G) 1000ºC (H) 1100ºC (I) 1200ºC (J) 1300ºC. TM=Tempered Martensite, δ = Delta Ferrite, AQM = As-Quenched Martensite.

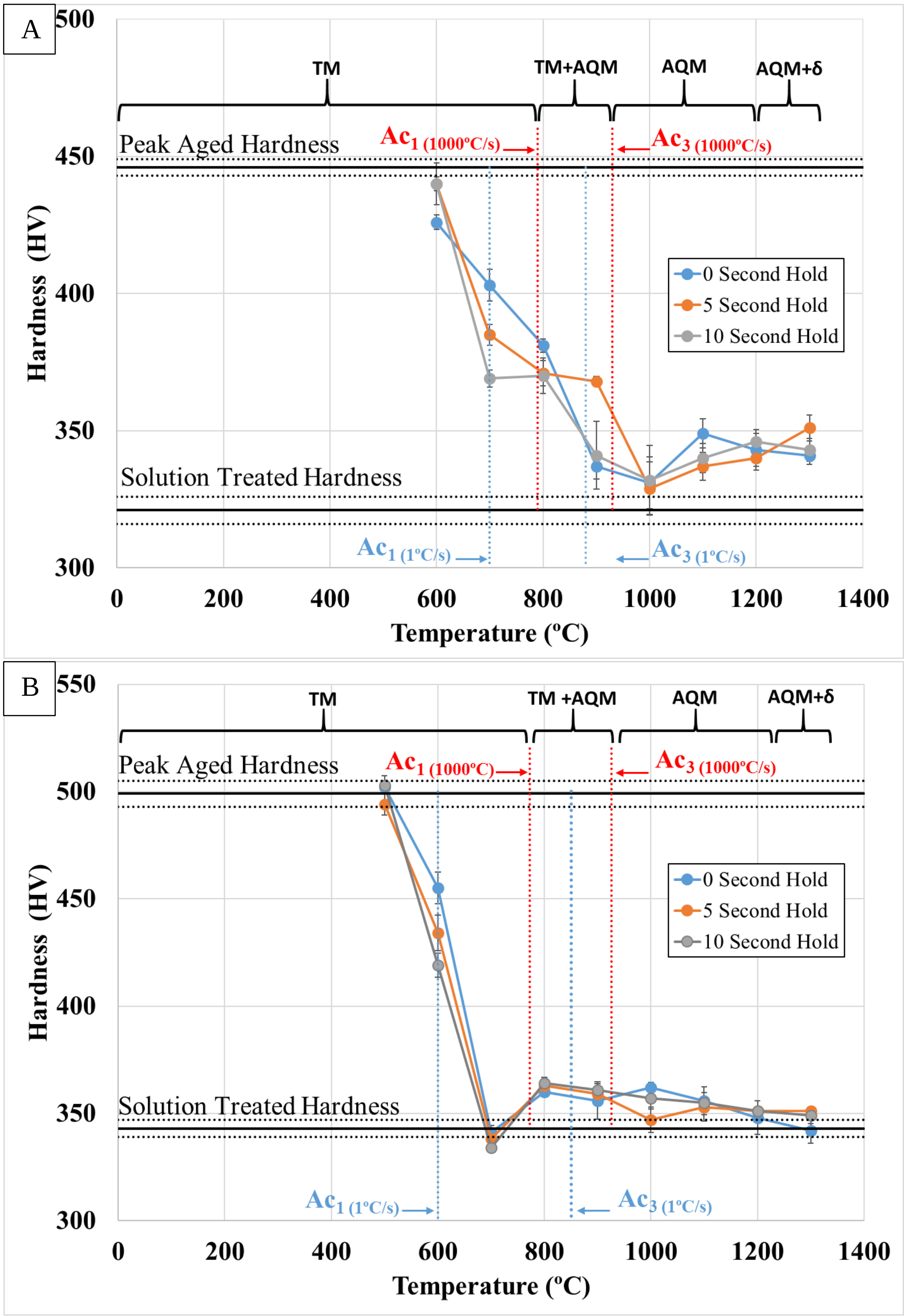

Figure 24: Plot of hardness as a function of peak temperature for 0, 5, and 10, seconds for (A) 17-4 and (B) 13-8+Mo.

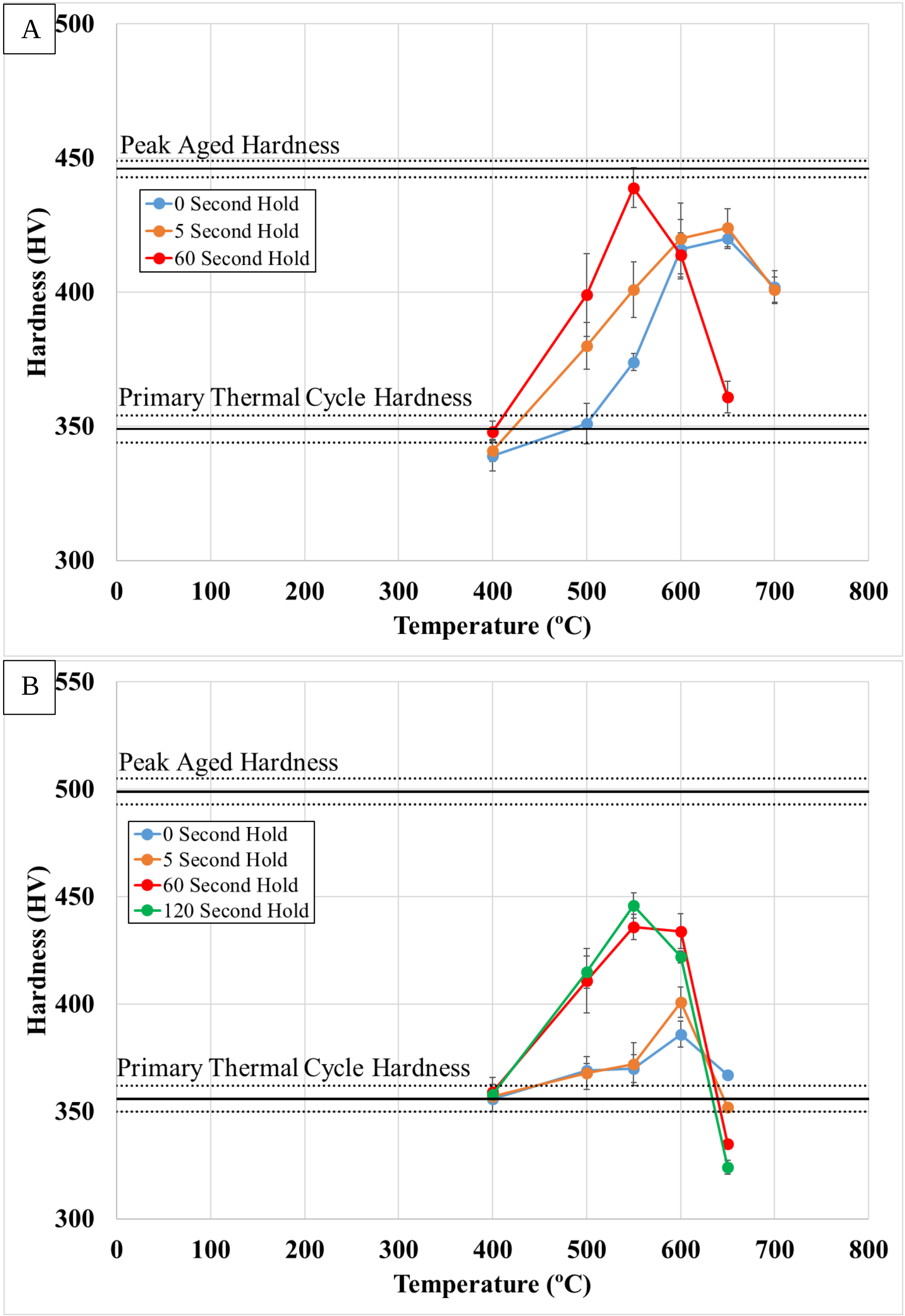

Figure 25: Plot of hardness as a function of peak temperature for (A) 17-4 with a 0, 5, and 60 second hold and (B) 13-8+Mo with a 0, 5, 60, and 120 second hold.

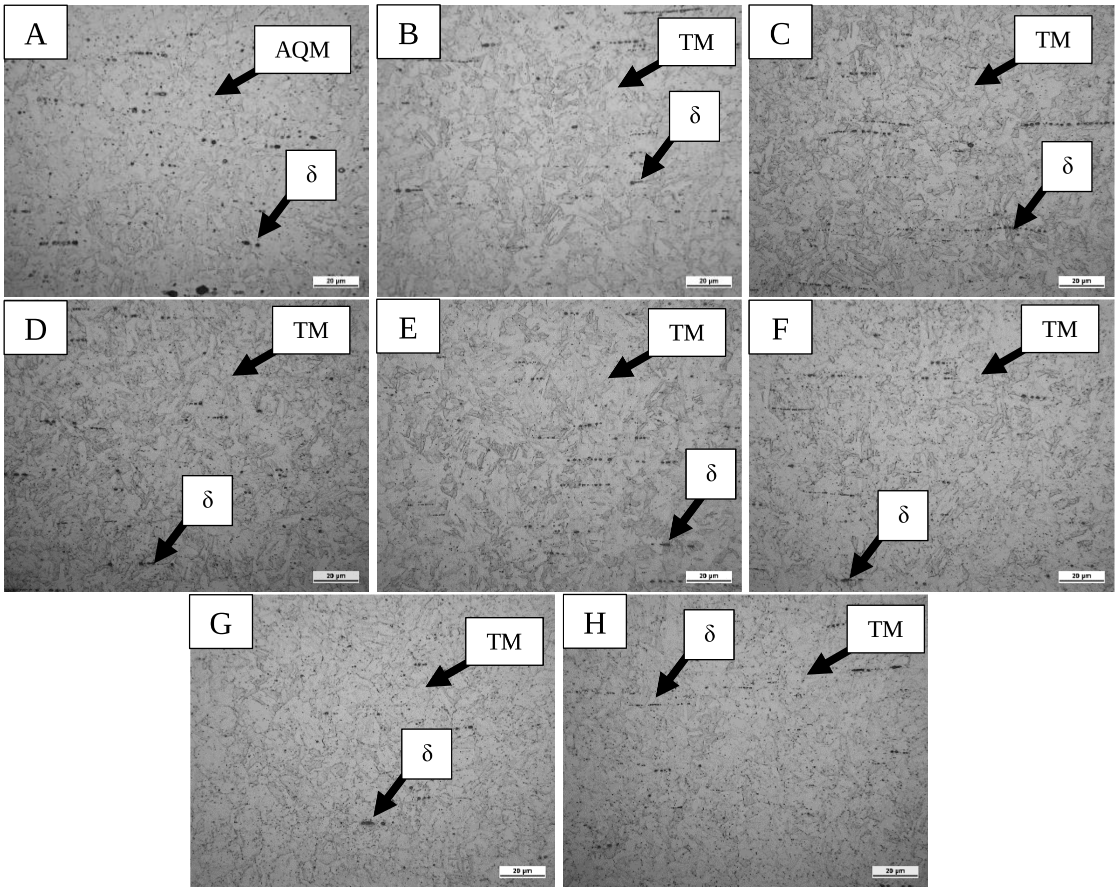

Figure 26: Light optical photomicrographs of 17-4 Gleeble samples subjected to a primary peak temperature of 1100ºC and then heated to various temperatures with 0 second hold time. (A) 1100ºC primary (B) 400ºC (C) 500ºC (D) 550ºC (E) 600ºC (F) 650ºC and (G) 700ºC (H) 700ºC with a 5 second hold. TM=Tempered Martensite, δ = Delta Ferrite, AQM = As-Quenched Martensite.

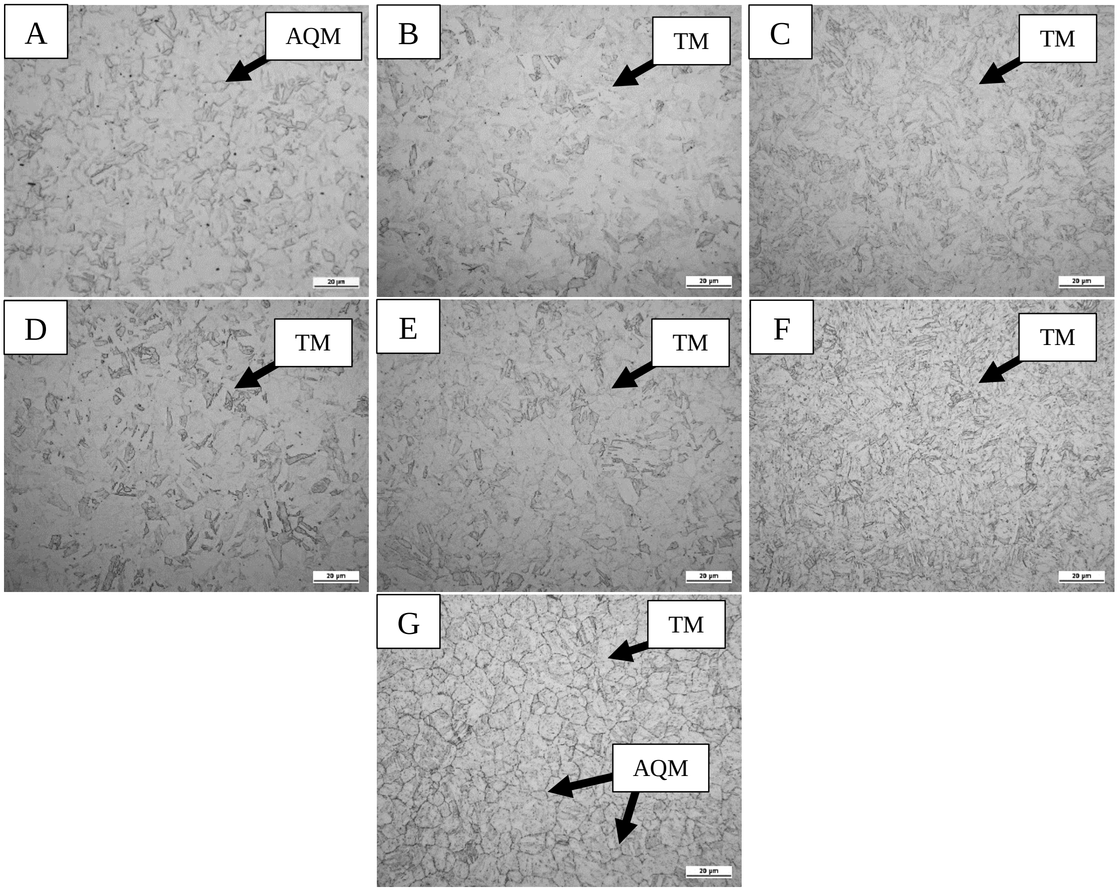

Figure 27: Light optical photomicrographs of 13-8+Mo Gleeble samples subjected to a primary peak temperature of 1100ºC and then heated to various temperatures with 0 second hold time. (A) 1100ºC Primary (B) 400ºC (C) 500ºC (D) 550ºC (E) 600ºC (F) 650ºC (F) 650ºC with a 120 second hold TM=Tempered Martensite, AQM = As-Quenched Martensite.

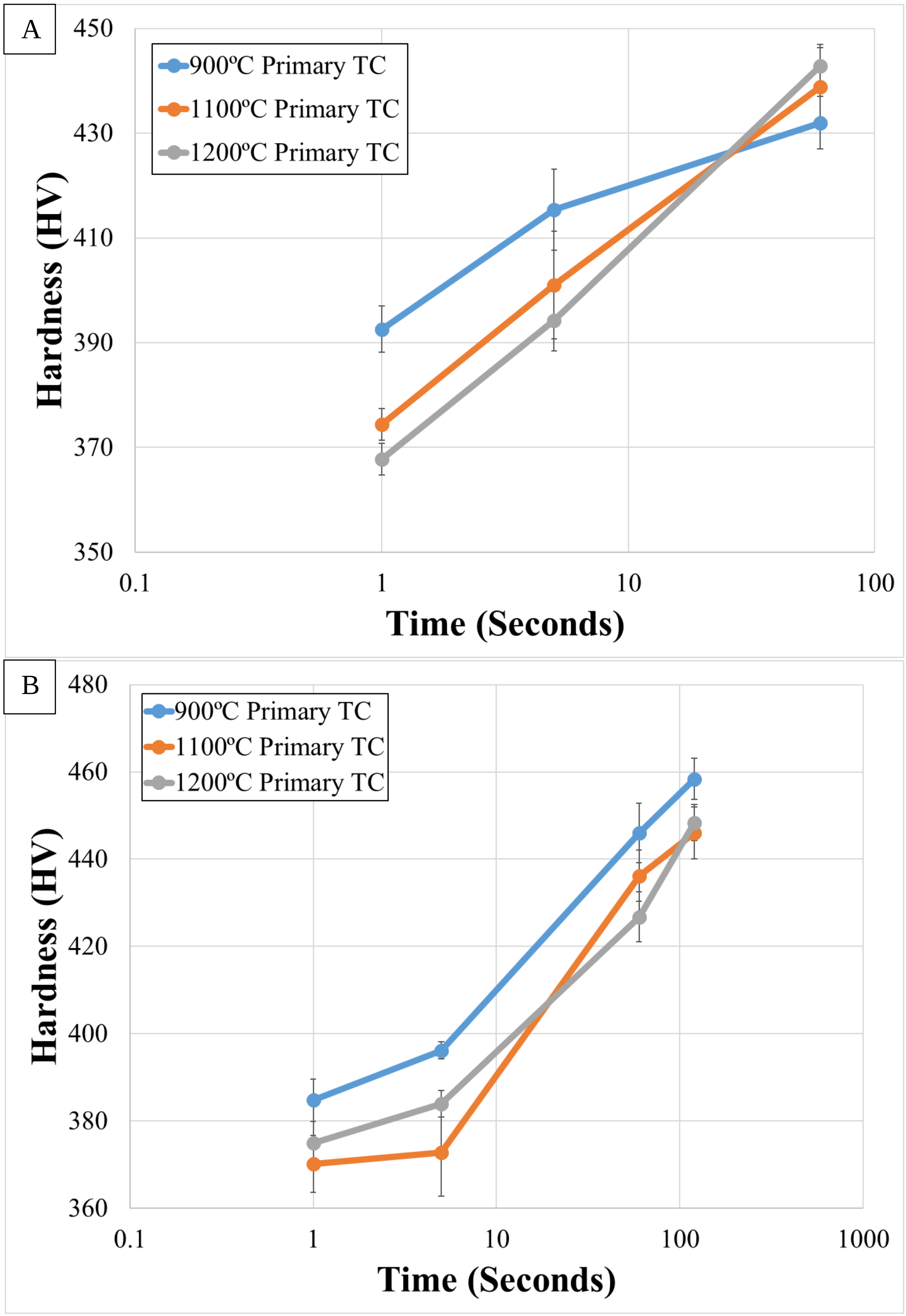

Figure 28: Secondary heating experiments performed with a primary peak temperature treatment of 900ºC, 1100ºC and 1200ºC with no hold and secondary heat treatments at 550ºC for 17-4 and 13-8+Mo for (A) 17-4 and (B) 13-8+Mo.

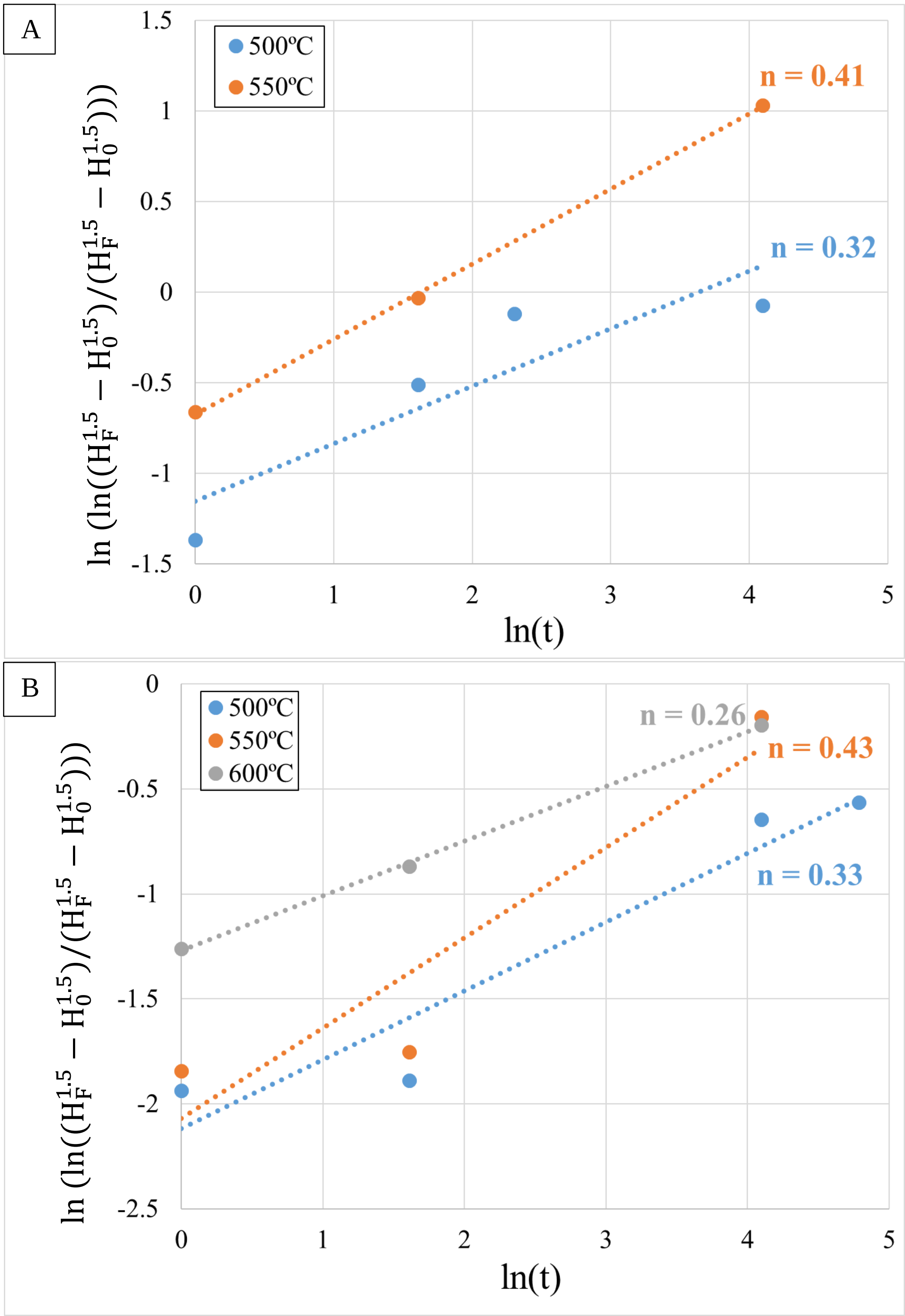

Figure 29: Plot of $\ln(\ln((H_F^{1.5} - H_0^{1.5})/(H_F^{1.5} - H_0^{1.5})))$ vs ln (t) for (A) 17-4 and (B) 13-8+Mo.

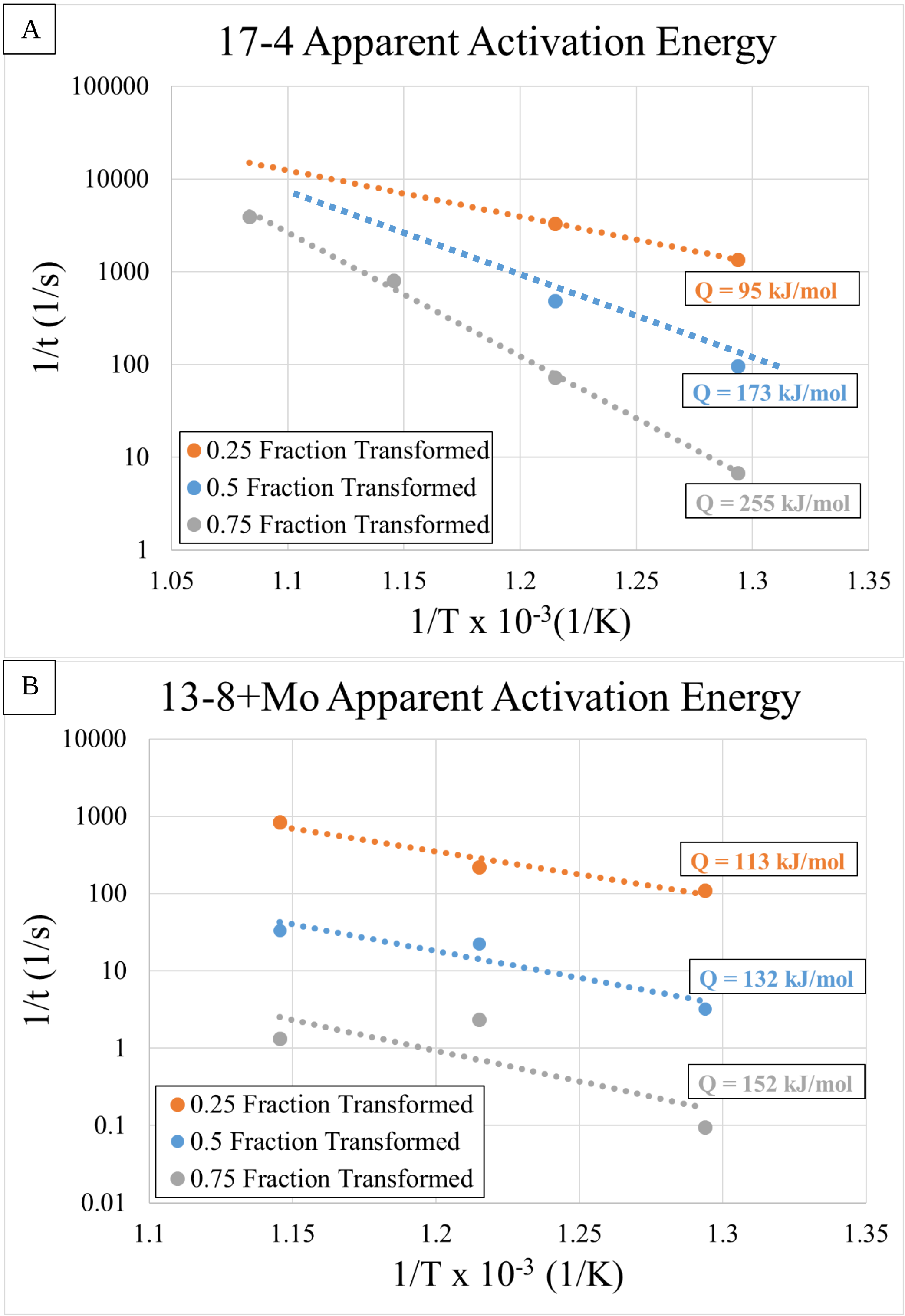

Figure 30: Plot of apparent activation energy for (A) 17-4 and (B) 13-8+Mo.

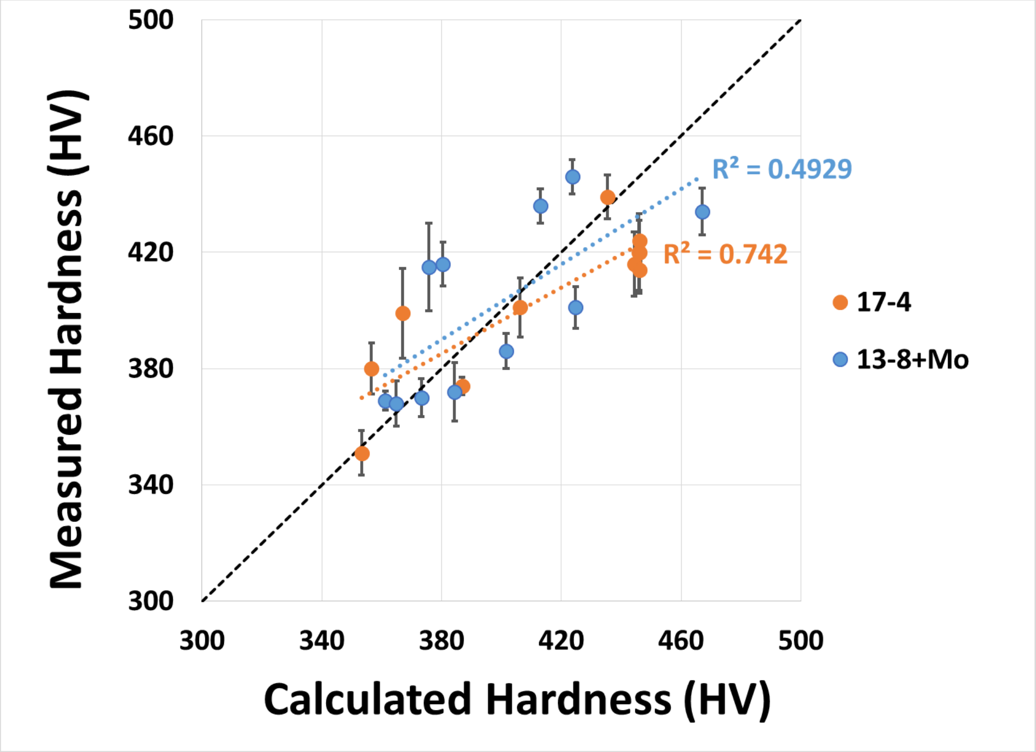

Figure 31: Plot of measured vs calculated hardness for 17-4 and 13-8+Mo.

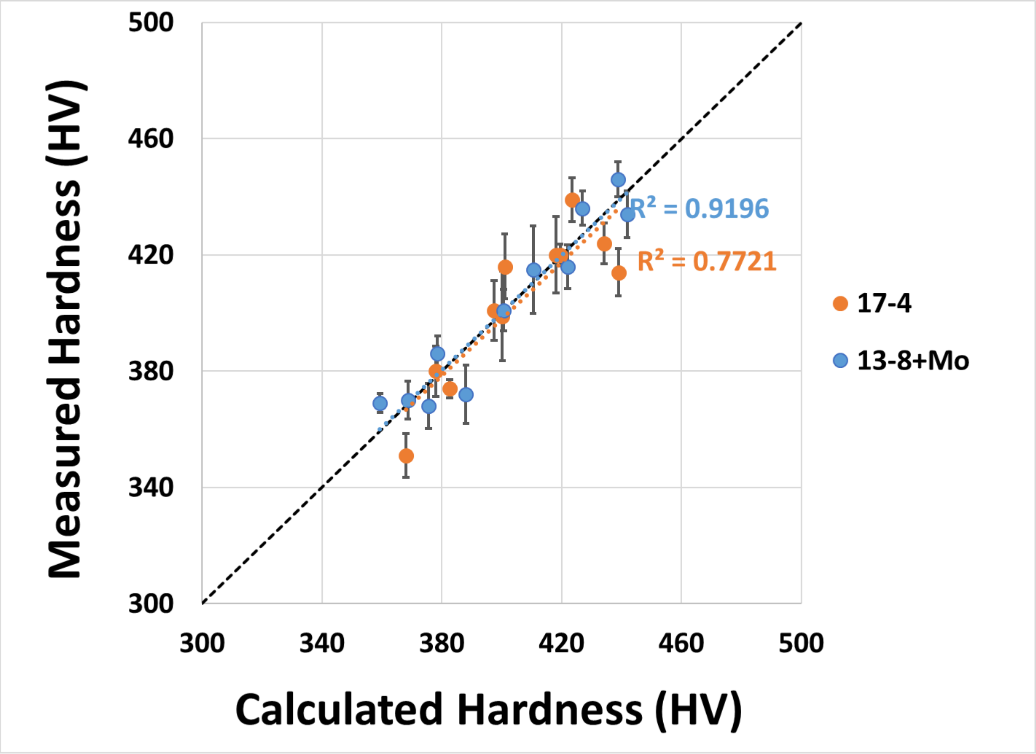

Figure 32: Plot of measured vs calculated hardness for 17-4 and 13-8+Mo using data optimization to achieve best fit.

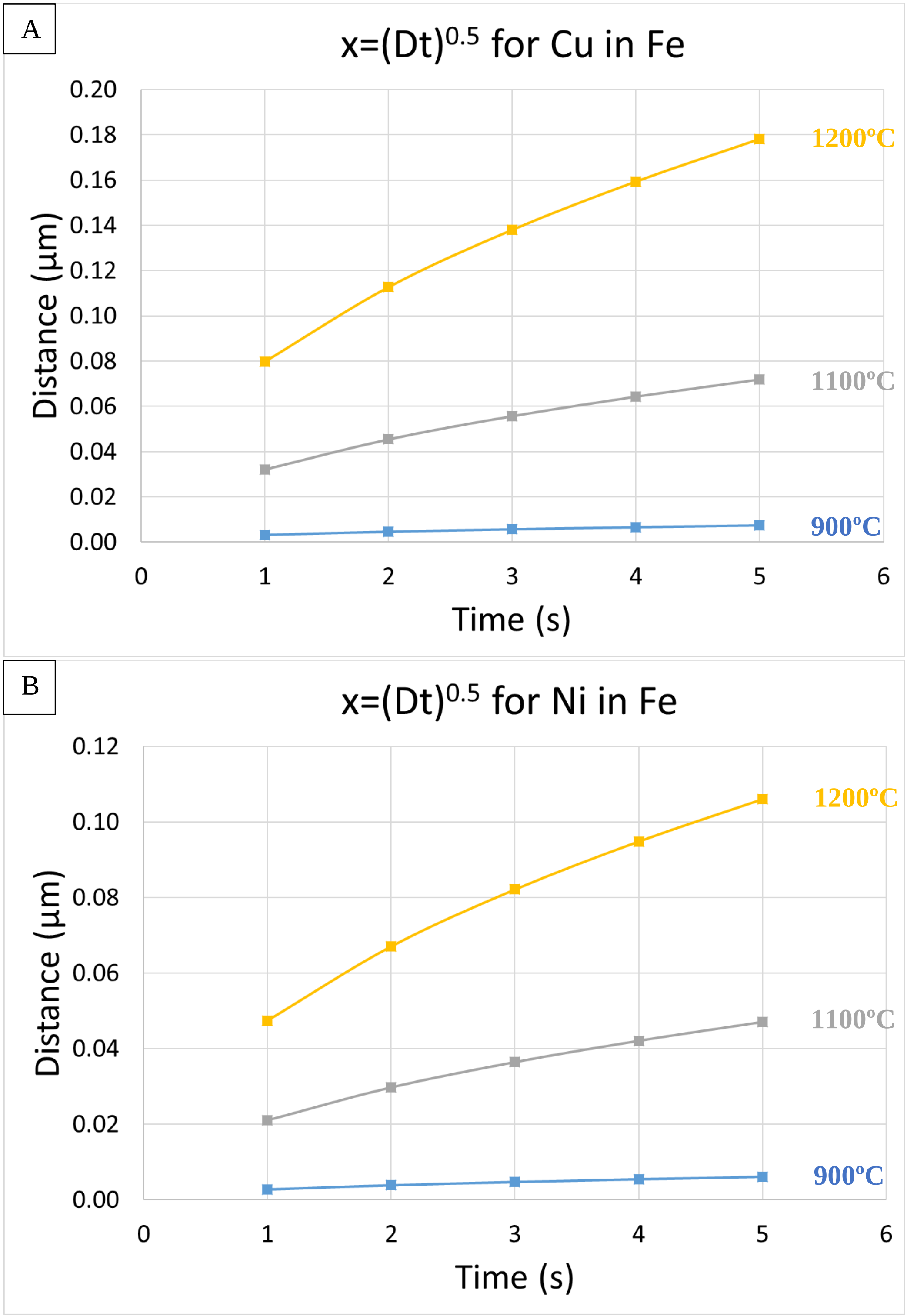

Figure 33: Calculated diffusion distances for (A) Cu in Fe and (B) Ni in Fe.

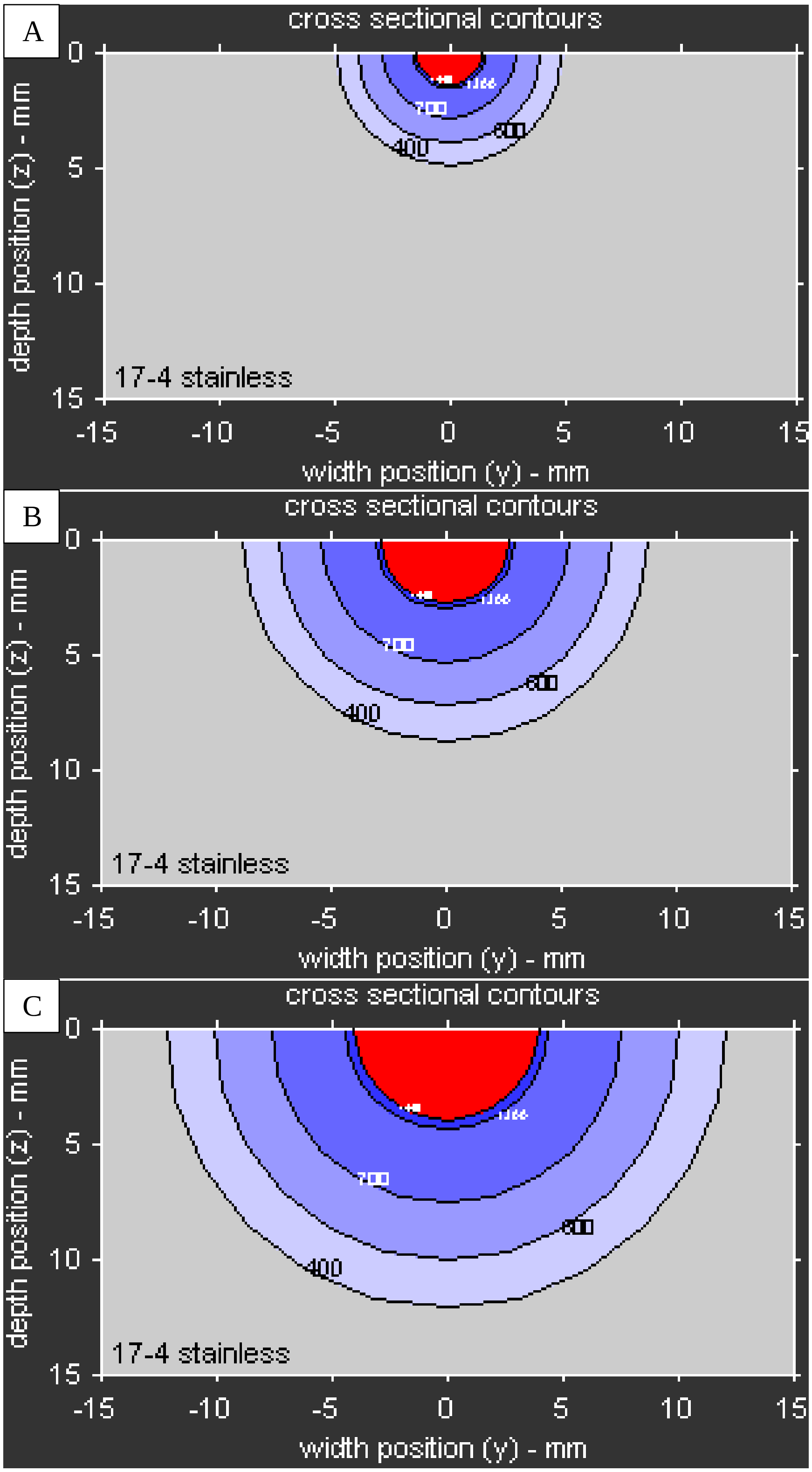

Figure 34: SmartWeld isotherms predicted for 17-4 with an (A) 1000 J/mm (B) 2000 J/mm and (C) 3000 J/mm heat input.

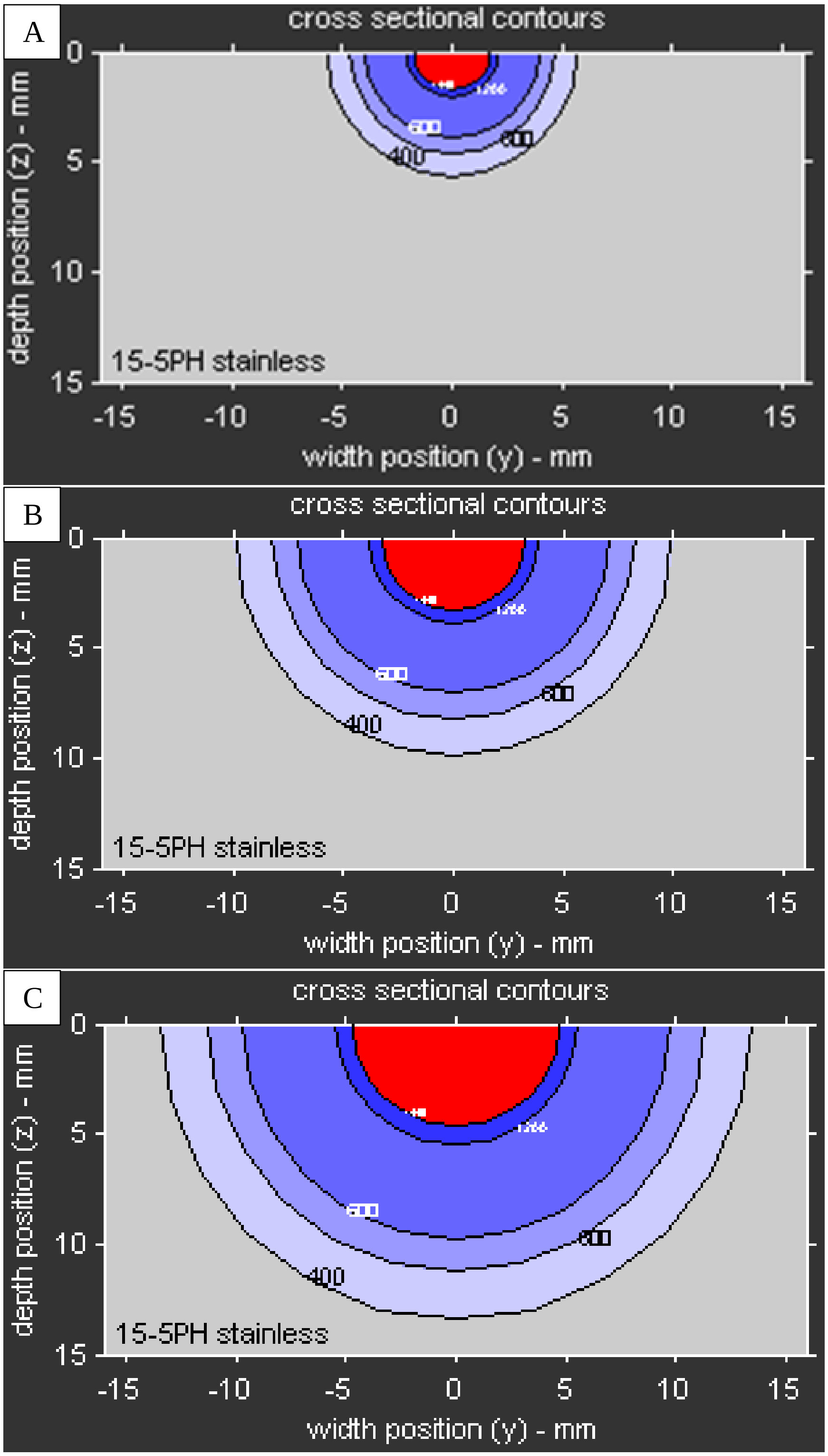

Figure 35: SmartWeld isotherms predicted for 13-8+Mo with an (A) 1000 J/mm (B) 2000 J/mm and (C) 3000 J/mm heat input.

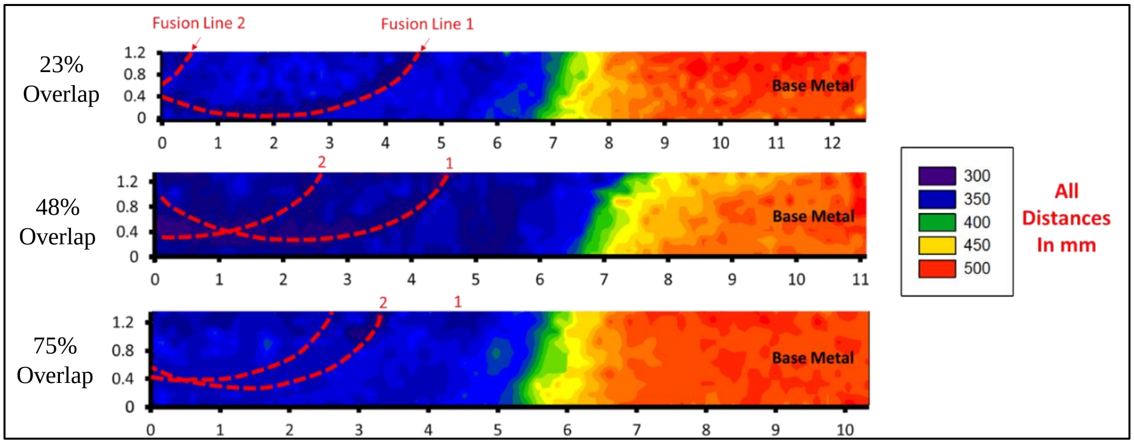

Figure 36: Hardness maps measured across a dual-pass 17-4 GTA weld made with a 1000 J/mm heat input with 25%, 50% and 75% target overlaps.

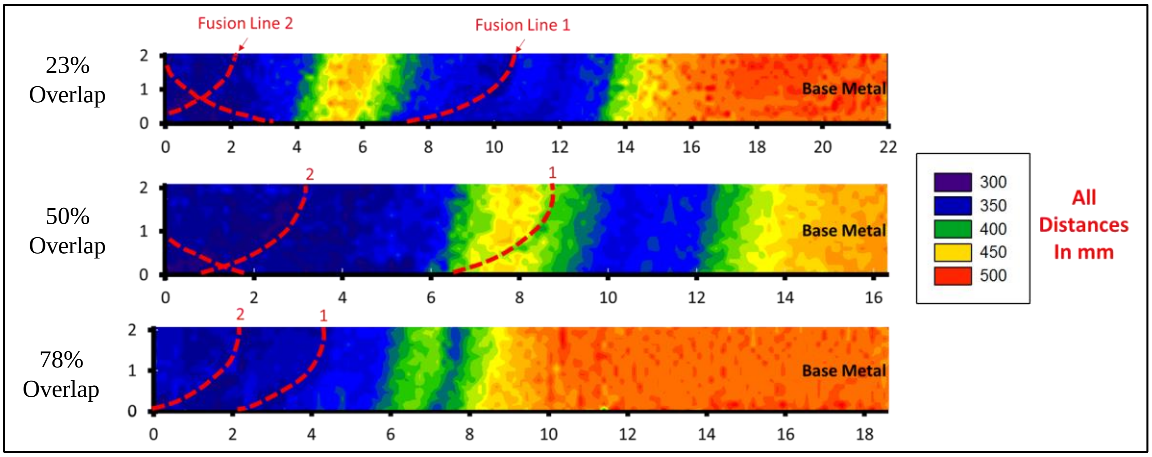

Figure 37: Hardness maps measured across a dual-pass 17-4 GTA weld made with a 2000 J/mm heat input with 25%, 50% and 75% target overlaps.

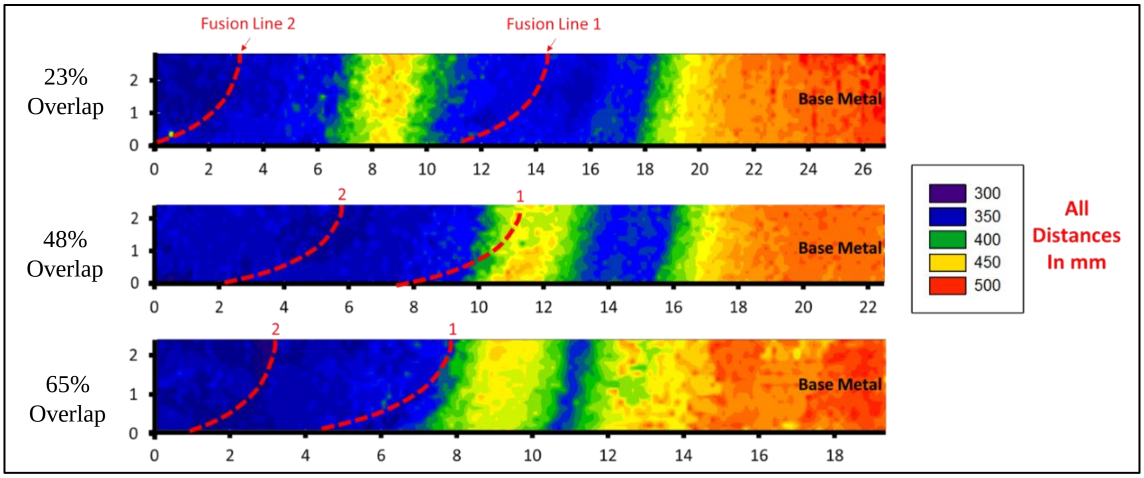

Figure 38: Hardness maps measured across a dual-pass 17-4 GTA weld made with a 3000 J/mm heat input with 25%, 50% and 75% target overlaps.

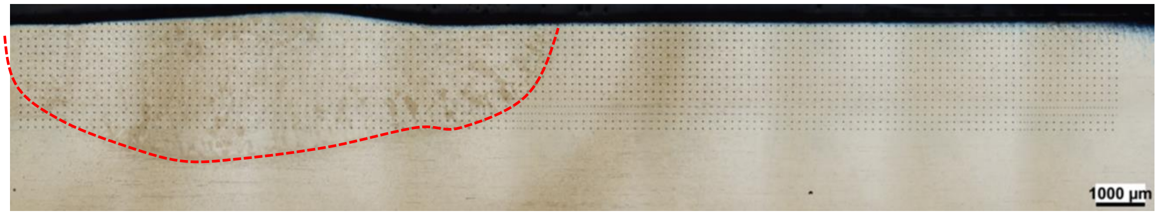

Figure 39: Light optical mircograph of the cross-section of the 17-4 2000 J/mm primary weld pass. Demonstrating the oblong nature of the weld pool.

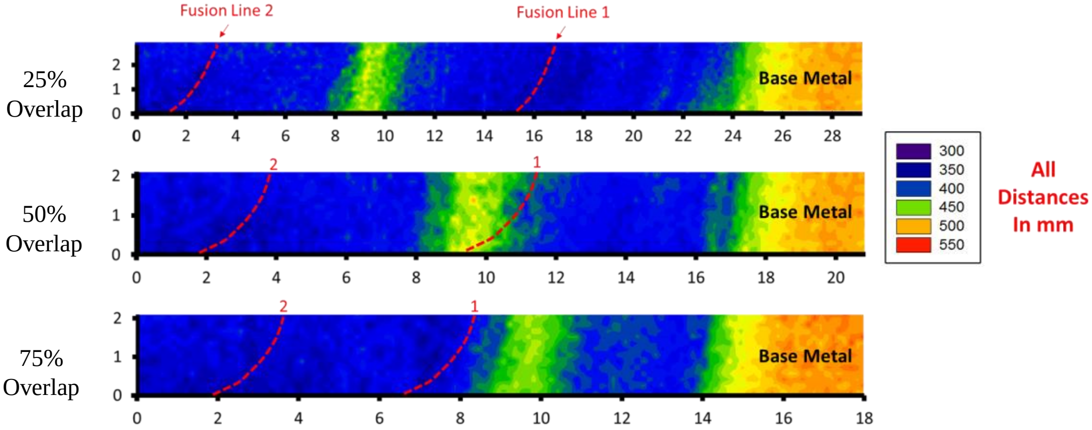

Figure 40: Hardness maps measured across a dual-pass 13-8+Mo GTA weld made with a 3000 J/mm heat input with 25%, 50% and 75% target overlaps.

References

1. Lippold, J. C. & Kotecki, D. J. Welding Metallurgy and Weldability of Stainless Steels. *Weld. Metall. Weldability Stainl. Steels John C Lippold Damian J Kotecki Pp 376 ISBN 0-471-47379-0 Wiley-VCH March 2005* **1,** (2005).
2. Bhadeshia, H. & Honeycombe, R. *Steels: Microstructure and Properties: Microstructure and Properties*. (Butterworth-Heinemann, 2011).
3. M88 | BAE Systems | International. Available at: http://www.baesystems.com/en/product/m88a2-hercules-recovery-vehicle. (Accessed: 15th August 2016)
4. *CES EduPak 2016*. (Granta Design Limited).
5. Ferjutz, K. & Davis, J. R. *ASM Handbook: Volume 6: Welding, Brazing, and Soldering*. (ASM International, 1993).
6. Bhaduri, A. K. & Venkadesan, S. Microstructure of the heat-affected zone in 17-4 PH stainless steel. *Steel Res.* **60,** 509–513 (1989).
7. Hochanadel, P. W., Edwards, G. R., Robino, C. V. & Cieslak, M. J. Heat treatment of investment cast PH 13-8 Mo stainless steel: Part I. Mechanical properties and microstructure. *Metall. Mater. Trans. A* **25,** 789–798 (1994).
8. Wanjara, P. & Jahazi, M. Characterization of electron beam welded 17-4 ph stainless steel. *Can. Metall. Q.* **47,** 413–436 (2008).
9. Petty, E. R. *Martensite: Fundamentals and Technology, Edited by E.R. Petty*. (1970).
10. CHRISTIAN, J. W. CHAPTER 21 - Characteristics of Martensitic Transformations. in *The Theory of Transformations in Metals and Alloys* 961–991 (Pergamon, 2002).

11. Murthy, A. S. *et al.* Copper precipitation in cobalt-alloyed precipitation-hardened stainless steel. *Scr. Mater.* **66,** 943–946 (2012).
12. Ping, D. H., Ohnuma, M., Hirakawa, Y., Kadoya, Y. & Hono, K. Microstructural evolution in 13Cr–8Ni–2.5Mo–2Al martensitic precipitation-hardened stainless steel. *Mater. Sci. Eng. A* **394,** 285–295 (2005).
13. Schnitzer, R. *et al.* Reverted austenite in PH 13-8 Mo maraging steels. *Mater. Chem. Phys.* **122,** 138–145 (2010).
14. Hull, D. & Bacon, D. J. *Introduction to Dislocations*. (Butterworth-Heinemann, 2001).
15. Robino, C. V., Cieslak, M. J., Hochanadel, P. W. & Edwards, G. R. Heat treatment of investment cast PH 13-8 Mo stainless steel: Part II. Isothermal aging kinetics. *Metall. Mater. Trans. A* **25,** 697–704
16. Mirzadeh, H. & Najafizadeh, A. Aging kinetics of 17-4 PH stainless steel. *Mater. Chem. Phys.* **116,** 119–124 (2009).
17. Avrami, M. Kinetics of Phase Change. I General Theory. *J. Chem. Phys.* **7,** 1103–1112 (1939).
18. Avrami, M. Kinetics of Phase Change. II Transformation-Time Relations for Random Distribution of Nuclei. *J. Chem. Phys.* **8,** 212–224 (1940).
19. Avrami, M. Granulation, Phase Change, and Microstructure Kinetics of Phase Change. III. *J. Chem. Phys.* **9,** 177–184 (1941).
20. Hamlin, R. J. & DuPont, J. N. Microstructural Evolution and Mechanical Properties of Simulated Heat-Affected Zones in Cast Precipitation-Hardened Stainless Steels 17-4 and 13-8+Mo. *Metall. Mater. Trans. A* **48,** 246–264 (2017).

21. Povoden-Karadeniz, E. & Kozeschnik, E. Simulation of precipitation kinetics and precipitation strengthening of B2-precipitates in martensitic PH 13-8 Mo steel. *ISIJ Int.* **52,** 610–615 (2012).
22. Holzer, I. & Kozeschnik, E. Simulation of Copper Precipitation in Fe-Cu Alloys. *Mater. Sci. Forum* **638–642,** 2579–2584 (2010).
23. Yu, X. *et al.* Strength Recovery in a High-Strength Steel During Multiple Weld Thermal Simulations. *Metall. Mater. Trans. A* **42,** 3669–3679 (2011).
24. Brooks, J. A. & Garrison Jr., W. M. Weld microstructure development and properties of precipitation-strengthened martensitic stainless steels. *Weld. J. Miami Fla* **78,** 280–s–291–s (1999).
25. Gladman, T. Precipitation hardening in metals. *Mater. Sci. Technol.* **15,** 30–36 (1999).
26. Guo, Z. & Sha, W. Quantification of Precipitation Hardening and Evolution of Precipitates. *Mater. Trans.* **43,** 1273–1282 (2002).
27. Viswanathan, U. K., Banerjee, S. & Krishnan, R. Effects of aging on the microstructure of 17-4 PH stainless steel. *Mater. Sci. Eng. Struct. Mater. Prop. Microstruct. Process.* **A104,** 181–189 (1988).
28. Bhaduri, A. K., Sujith, S., Srinivasan, G., Gill, T. P. S. & Mannan, S. L. Optimized postweld heat treatment procedures for 17-4 PH stainless steels. *Weld. J. Miami Fla* **74,** 153–159 (1995).
29. Fuerschbach, P. W. & Eisler, G. R. Determination of material properties for welding models by means of arc weld experiments. in *Sixth Int. Conf. Trends in Welding Research* 1–5

30. Fuerschbach, P. W., Eisler, G. R. & Steele, R. J. *Weld procedure development with OSLW-optimization software for laser welding*. (Sandia National Labs., Albuquerque, NM (United States), 1998).

31. Reed, R. C. & Bhadeshia, H. K. D. H. A simple model for multipass steel welds. *Acta Metall. Mater.* **42,** 3663–3678 (1994).

32. Andersson, J.-O., Helander, T., Höglund, L., Shi, P. & Sundman, B. Thermo-Calc & DICTRA, computational tools for materials science. *Calphad* **26,** 273–312 (2002).

33. Sindo, K. Welding metallurgy. *John Wiley Sons N. Y.* 199–206 (2003).

34. Bono, J. T., DuPont, J. N., Jain, D., Baik, S.-I. & Seidman, D. N. Investigation of Strength Recovery in Welds of NUCu-140 Steel Through Multipass Welding and Isothermal Post-Weld Heat Treatments. *Metall. Mater. Trans. A* **46,** 5158–5170 (2015).

35. Porter, D. A. & Easterling, K. E. *Phase Transformations in Metals and Alloys, Third Edition (Revised Reprint)*. (CRC Press, 1992).

36. CHRISTIAN, J. W. CHAPTER 16 - Precipitation from Supersaturated Solid Solution. in *The Theory of Transformations in Metals and Alloys* 718–796 (Pergamon, 2002).

37. *Smithells Metals Reference Book, Seventh Edition*. (Butterworth-Heinemann, 1998).

38. Cieslak, M. J., Hills, C. R., Hlava, P. F. & David, S. A. An investigation of the high-temperature and solidification microstructures of PH 13-8 Mo stainless steel. *Metall. Trans. A* **21,** 2465–2475 (1990).

39. Bower, T. F., Brody, H. D. & Flemings, M. C. Measurements of Solute Redistribution in Dendritic Solidification. *Trans. Metall. Soc. AIME* **236,** 624–633 (1966).
40. Clyne, T. W. & Kurz, W. Solute redistribution during solidification with rapid solid state diffusion. *Metall. Trans. A* **12,** 965–971 (1981).
41. DuPont, J. N., Marder, A. R., Notis, M. R. & Robino, C. V. Solidification of Nb-bearing superalloys: Part II. Pseudoternary solidification surfaces. *Metall. Mater. Trans. A* **29,** 2797–2806 (1998).
42. Adams, K. D. & DuPont, J. N. Influence of Ti and C on the Solidification Microstructure of Fe-10Al-5Cr Alloys. *Metall. Mater. Trans. A* **41,** 194–201 (2010).
43. Oikawa, H. Review on Lattice Diffusion of Substitutional Impurities in Iron. *Technol. Rep. Tohoku Univ.* **47,** 215–224 (1982).
44. CHRISTIAN, J. W. CHAPTER 12 - Formal Theory of Transformation Kinetics. in *The Theory of Transformations in Metals and Alloys* 529–552 (Pergamon, 2002).
45. Christian, J. W. Chapter 12 - Formal Theory of Transformation Kinetics. in *The Theory of Transformations in Metals and Alloys* (ed. Christian, J. W.) 529–552 (Pergamon, 2002).
46. Floreen, S. The physical metallurgy of maraging steels. *Metall. Rev.* **13,** 115–128 (1968).
47. Squires, D. R. & Wilson, E. A. Kinetics of aging in an Fe-12Ni-6Mn maraging alloy. *Metall. Trans. A* **15,** 1947–1948 (1984).
48. Viswanathan, U. K., Nayar, P. K. K. & Krishnan, R. Kinetics of precipitation in 17–4 PH stainless steel. *Mater. Sci. Technol.* **5,** 346–349 (1989).

49. Floreen, S. & Decker, R. F. Heat treatment of 18% Ni maraging steels. *Trans ASM* **55,** 518 (1962).
50. Vasudevan, V. K., Kim, S. J. & Wayman, C. M. Precipitation reactions and strengthening behavior in 18 Wt Pct nickel maraging steels. *Metall. Trans. A* **21,** 2655–2668 (1990).
51. Rivolta, B. & Gerosa, R. On the non-isothermal precipitation of copper-rich phase in 17-4 PH stainless steel using dilatometric techniques. *J. Therm. Anal. Calorim.* **102,** 857–862 (2010).
52. Kapoor, R. & Batra, I. S. On the to transformation in maraging (grade 350), PH 13-8 Mo and 17-4 PH steels. *Mater. Sci. Eng. A* **371,** 324–334 (2004).
53. CHRISTIAN, J. W. CHAPTER 9 - Diffusion in the Solid State. in *The Theory of Transformations in Metals and Alloys* 378–421 (Pergamon, 2002).
54. Wu, J.-H. & Lin, C.-K. Influence of high temperature exposure on the mechanical behavior and microstructure of 17-4 PH stainless steel. *J. Mater. Sci.* **38,** 965–971 (2003).
55. Sinha, P. P., Sivakumar, D., Babu, N. S., Tharian, K. T. & Natarajan, A. Austenite reversion in 18 Ni Co-free maraging steel. *Steel Res.* **66,** 490–494 (1995).
56. Nakagawa, H., Miyazaki, T. & Yokota, H. Effects of aging temperature on the microstructure and mechanical properties of 1.8Cu-7.3Ni-15.9Cr-1.2Mo-low C, N martensitic precipitation hardening stainless steel. *J. Mater. Sci.* **35,** 2245–2253 (2000).
57. Miner, R. E., Jackson, J. K. & Gibbons, D. F. INTERNAL FRICTION IN 18 PER CENT NI MARAGING STEELS. *AIME MET SOC TRANS* **236,** 1565–1570 (1966).

58. Speich, G. R., Dabkowski, D. S. & Porter, L. F. Strength and toughness of Fe-10ni alloys containing C, Cr, Mo, and Co. *Metall. Trans.* **4,** 303–315 (1973).
59. Rosenthal, D. & Rosenthal, D. Mathematical theory of heat distribution during welding and cutting. (1941).
60. Schnitzer, R., Zinner, S. & Leitner, H. Modeling of the yield strength of a stainless maraging steel. *Scr. Mater.* **62,** 286–289 (2010).

Vita

Robert Hamlin was born and raised in Jonesville, Vermont. He attended Richmond Elementary School, Camels Hump Middle School, and Mount Mansfield Union High School. In August 2008 Robert enrolled in Lehigh University in Bethlehem, Pennsylvania where he majored in Materials Science and Engineering and competed for the Lehigh wrestling team. He graduated with honors in 2013 with a Bachelor of Science degree in Materials Science and Engineering and received the Lehigh University scholar athlete award. He then joined the Engineering Metallurgy Group and chose to continue his education in the graduate degree program in Lehigh's Department of Materials Science under the advisement of Dr. John DuPont. He graduated with his Master of Science degree in May 2015 and earned his PhD in September 2017.